Nanoscale X-ray Computed Tomography Based Modeling of Lithium-ion Battery Electrodes

by

Ali Ghorbani Kashkooli

A thesis

presented to the University of Waterloo

in fulfillment of the

thesis requirement for the degree of

Doctor of Philosophy

in

Chemical Engineering

Waterloo, Ontario, Canada, 2018

© Ali Ghorbani Kashkooli 2018

Examining Committee Membership

The following served on the Examining Committee for this thesis. The decision of the Examining Committee is by majority vote.

External Examiner	Dr. Jon G. Pharoah Professor
Co-Supervisor	Dr. Zhongwei Chen Professor
Co-Supervisor	Dr. Siamak Farhad Assistant Professor
Internal Member	Dr. Eric Croiset Professor
Internal Member	Dr. Michael Pope Assistant Professor
Internal-external Member	Dr. Xianguo Li Professor

Author’s Declaration

This thesis consists of material all of which I authored or co-authored: see Statement of Contribution included in the thesis. This is a true copy of the thesis, including any required final revisions, as accepted by my examiners.

I understand that my thesis may be made electronically available to the public.

Statement of Contributions

The body of this thesis is based on a combination of published work. Various sections are adapted from the following list of publications:

Chapter 3

A.G. Kashkooli, S. Farhad, D.U. Lee, K. Feng, S. Litster, S. K. Babu, L. Zhu, Z. Chen, "Multiscale modeling of lithium-ion battery electrodes based on nano-scale X-ray computed tomography", Journal of Power sources, 2016, 307, 496-509.

Dr. Farhad and I developed the modeling framework. I carried out the simulation. Mr. Babu and Dr. Litster performed the X-ray computed tomography imaging. Mr. Feng and I performed experimental testing of batteries. I prepared all the results and wrote the final manuscript. Dr. Lee, Dr. Zhu, Dr. Farhad, and Dr. Chen reviewed the manuscript.

Chapter 4

A.G. Kashkooli, A. Amirfazli, S. Farhad, D.U. Lee, S. Felicelli, H.W. Park, K. Feng, V.D. Andrade, Z. Chen, "Representative volume element model of lithium-ion battery electrodes based on X-ray nano-tomography", Journal of Applied Electrochemistry, 2017, 47-281.

I developed the modeling framework, Mr. Amirfazli assisted with the computer simulation, and Dr. Farhad was the advisor for model development and results generation. Dr. De Andrade performed the synchrotron X-ray computed tomography at Argonne national laboratory. Mr. Feng and I performed experimental testing of

batteries. I prepared all the results and wrote the final manuscript. Dr. Lee, Dr. Zhu, Dr. Farhad, Dr. Felicelli, and Dr. Chen reviewed the manuscript.

Chapter 5

A.G. Kashkooli, G. Lui, S. Farhad, D. U. Lee, K. Feng, A. Yu, Z. Chen, "Nano-particle size effect on the performance of $Li_4Ti_5O_{12}$ spinel". Electrochimica Acta, 2016, 196, 33–40.

I developed the modeling framework along with the computer simulation, and Dr. Farhad was the advisor for model development and results generation. Mr. Lui performed the material synthesis and characterization and fabricate the battery's electrode. Mr. Feng fabricated the half coin-cells and performed experimental testing of batteries. I prepared the simulation results and wrote the final manuscript. Dr. Lee, Dr. Farhad, and Dr. Chen reviewed the manuscript.

A. G. Kashkooli, E. Foreman, S. Farhad, D. U. Lee, K. Feng, G. Lui, V. D. Andrade, Z. Chen, "Morphological and electrochemical characterization of a nanostructure $Li_4Ti_5O_{12}$ electrodes using multiple imaging mode synchrotron X-ray computed tomography", Journal of the Electrochemical Society, 2017, 164 (13), A1-A11.

I developed the modeling framework and image processing along with the computer simulation, and Dr. Farhad was the advisor for model development and results generation. Dr. De Andrade performed the synchrotron X-ray computed tomography at Argonne national laboratory while Mr. Foreman assisted with the sample preparation. Mr. Lui performed the material synthesis and characterization and fabricate the battery's electrode. Mr. Feng and I fabricated the coin-cells and

performed experimental testing of batteries. I prepare all the results and wrote the final manuscript. Dr. Lee, Dr. Farhad, and Dr. Chen reviewed the manuscript.

Chapter 6

A. G. Kashkooli, E. Foreman, S. Farhad, D. U. Lee, W. Ahn, K. Feng, V. D. Andrade, Z. Chen, “Synchrotron X-ray nano computed tomography based simulation of stress evolution in $LiMn_2O_4$ electrodes”, Electrochimcia Acta, 2017, 247, 1103–1116.

I developed the modeling framework and image processing along with the computer simulation, and Dr. Farhad was the advisor for model development and results generation. Dr. De Andrade performed the synchrotron X-ray computed tomography at Argonne national laboratory while Mr. Foreman and Mr. Feng, assisted with the electrode’s sample preparation. I prepared all the results and wrote the final manuscript. Dr. Ahn, Dr. Lee, Dr. Farhad, and Dr. Chen reviewed the manuscript.

Abstract

Because of their high energy/power density, long cycle life, and extremely low rate of self-discharge, lithium-ion batteries (LIBs) have dominated portable electronics, smart grid, and electric vehicles (EVs). Although they are the most developed and widely applied energy storage technology, there is still a strong desire to further enhance their energy/power density, cycle life, and safety. While all of these battery requirements are macroscopic and stated at cell/pack scale, they have to be addressed at particle or network of particles scale (mesoscale). At mesoscale, active material particles having different shape and morphologies are bound together with a carbon-doped polymer binder layer. This percolated network of particles serves as the electron conductive path from the reaction sites to the current collector. Even though significant research has been conducted to understand the physical and electrochemical behavior of material at the nanoscale, there have not been comprehensive studies to understand what is happening at the mesoscale.

Mathematical models have emerged as a promising way to shed light on complex physical and electrochemical phenomena happening at this scale. The idea of using mathematical model to study multiphysics behavior of LIBs is not new. Traditional models involved homogeneous spherical particles or computer generated electrode structures as the model geometry to simulate electrode/cell performance. While these models are successful to predict the cell performance, heterogeneous electrode's structure at mesoscale questions the accuracy of their findings related to battery internal behavior and property distribution.

The new advances in the field of 3D imaging including X-ray computed tomography (XCT) and Focused-ion beam/Scanning electron microscopy (FIB-SEM), have enabled the

3D visualization of the electrode's active particles and structures. In particular, XCT has offered nondestructive imaging and matter penetration capability in short period of time. Although it was commercialized in 70's, with the recent development of high resolution (down to 20 nm) laboratory and synchrotron radiation tomography has been revolutionized. 3D reconstructed electrodes based on XCT data can provide quantitative structural information such as particle and pore size distribution, porosity, solid/electrolyte interfacial surface area, and transport properties. In addition, XCT reconstructed geometry can be easily adopted as the model geometry for simulation purposes. For this, similar to traditional models, a modeling framework based on conservation of mass/charge and electrochemistry needs to be developed. The model links the electrode performance to the real electrode's structure geometry and allows for the detailed investigation of multiphysics phenomena. When combined with mechanical stress, such models can also be used for electrode's failure and degradation studies. The work presented in this dissertation aims to adopt 3D reconstructed structures from nano-XCT as the geometry to study multiphysics behaviour of the LIBs electrodes. In addition, 3D reconstructed structure provides more realistic electrode's morphological and transport properties. Such properties can benefit the homogeneous models by providing highly accurate input parameters.

In the first study, a multiscale platform has been developed to model LIB electrodes based on the reconstructed morphology. This multiscale framework consists of a microscale level where the electrode microstructure architecture is modeled and a macroscale level where discharge/charge is simulated. The coupling between two scales is performed in real time unlike using common surrogate based models for microscale. For microscale geometry 3D microstructure is reconstructed based on the nano-XCT data replacing typical computer

generated microstructure. It is shown that this model can predict the experimental performance of $LiFePO_4$ (LFP) cathodes at different discharge rates more accurately than the traditional/homogenous models. The approach employed in this study provides valuable insight into the spatial distribution of lithium within the microstructure of LIB electrodes.

In the second study, a new model that keeps all major advantages of the single-particle model of LIB and includes three-dimensional structure of the electrode was developed. Unlike the single spherical particle, this model considers a small volume element of an electrode, called the Representative Volume Element (RVE), which represent the real electrode structure. The advantages of using RVE as the model geometry was demonstrated for a typical LIB electrode consisting of nano-particle LFP active material. The model was employed to predict the voltage curve in a half-cell during galvanostatic operations and validated against experimental data. The simulation results showed that the distribution of lithium inside the electrode microstructure is very different from the results obtained based on the single-particle model.

In the third study, synchrotron X-ray computed tomography has been utilized using two different imaging modes, absorption and Zernike phase contrast, to reconstruct the real 3D morphology of nanostructured $Li_4Ti_5O_{12}$ (LTO) electrodes. The morphology of the high atomic number active material has been obtained using the absorption contrast mode, whereas the percolated solid network composed of active material and carbon-doped polymer binder domain (CBD) has been obtained using the Zernike phase contrast mode. The 3D absorption contrast image revealed that some LTO nano-particles tend to agglomerate and form secondary micro-sized particles with varying degrees of sphericity. The tortuosity of the pore and solid phases were found to have directional dependence, different from Bruggeman's

tortuosity commonly used in homogeneous models. The electrode's heterogeneous structure behaviour was also investigated by developing a numerical model to simulate a galvanostatic discharge process using the Zernike phase contrast mode.

In the last study, synchrotron X-ray nano-computed tomography has been employed to reconstruct real 3D active particle morphology of a $LiMn_2O_4$ (LMO) electrode. For the first time, CBD has been included in the electrode structure as a 108 nm thick uniform layer using image processing technique. With this unique model, stress generated inside four LMO particles with a uniform layer of CBD has been simulated, demonstrating its strong dependence on local morphology (surface concavity and convexity), and the mechanical properties of CBD such as Young's modulus. Specifically, high levels of stress have been found in vicinity of particle's center or near surface concave regions, however much lower than the material failure limits even after discharging rate as high as 5C. On the other hand, the stress inside CBD has reached its mechanical limits when discharged at 5C, suggesting that it can potentially lead to failure by plastic deformation. The findings in this study highlight the importance of modeling LIB active particles with CBD and its appropriate compositional design and development to prevent the loss of electrical connectivity of the active particles from the percolated solid network and power losses due to CBD failure.

There are still plenty of opportunities to further develop the methods and models applied in this thesis work to better understand the multiscale multiphysics phenomena happening in the electrode of LIBs. For example, in the multiscale model, microscale solid phase charge transfer and electrolyte mass/charge transfer can be included. In this way, heterogeneous distribution of current density in microscale would be achieved. Also, in both multiscale and RVE models, the exact location of CBD can be incorporated in the electrode structure to

specify lithium diffusional path inside the group of particles in the solid matrix. Finally, in the fourth study, the vehicle battery driving cycle can be applied instead of galvanostatic operating condition, to mimic the stress generated inside the electrodes in real practical condition.

Acknowledgements

First of all, I would like to thank my supervisors: Professor Zhongwei Chen and Professor Siamak Farhad, and all my colleagues I've worked with at the University of Waterloo. The opportunities which I was given to share ideas and technical knowledge were critical for making the progress and outcomes.

I'd like to thank my Ph.D. examining committee, Professor Xianguo Li, Professor Eric Croiset, Professor Michael Pope from university of Waterloo, and Professor Jon Pharoah as my external examiner from Queen's university for their time and contributions.

I'd like to acknowledge the support from the funding sources Natural Science and Engineering Research Council of Canada (NSERC) and University of Waterloo.

I'd also like acknowledge Advanced Photon Source (APS) in Argonne National Laboratory (ANL) for using Transmission X-ray Microscope (TXM) facility under "Fundamental study on structural defects of Li-ion battery electrodes & separators after capacity and power fading; Proposal: # 42190; 2015".

I'd also like to acknowledge the support from University of Akron for providing simulation Workstation, COMSOL Multiphysics®, and Simpleware 7 (Synopsys, Mountain View, USA) software.

Finally, I'd like to acknowledge the help and support I received from my family and friends. Without their love and care I would have not been able to make it this far.

Dedication

To my mother, Fariba, and my father, Kiyoumars, whose wholehearted love, wisdom, and support constantly encouraged me throughout life.

Table of Contents

List of Figures

List of Tables

List of Symbols

a	volume specific interfacial area (m^{-1})
c	lithium-ion concentration (mol m^{-3})
$\tilde{c}$	concentration change of lithium from the original condition (mol m^{-3})
D	diffusion coefficient (m^2 s^{-1})
E	Young's (elastic) modulus (Pa)
E_p	photon energy (J)
f	mean molar activity coefficient
F	Faraday's constant, 96487 (C mol^{-1})
i	current density (A m^{-2})
I	total applied current density to the cell (A m^{-2})
j_n	pore-solid flux of lithium-ion (mol m^{-3} s^{-1})
k_0	reaction rate constant $(\text{mol m}^{-2}\text{s}^{-1}(\text{mol m}^{-3})^{-1.5})$
ll	direction cosine between the external normal vector and x-coordinate
mm	direction cosine between the external normal vector and y-coordinate
nn	direction cosine between the external normal vector and z-coordinate
L	thickness (m)
n	unit vector normal to the boundary interface
OCP	interfacial open circuit potential (V)
r	spatial coordinate along the spherical particle radius
R	universal gas constant (J mol^{-1} K^{-1})
R_p	particle radius (m)

t	time (s)
T	temperature (K)
t_+	transference number of lithium-ion with respect to the solvent
u_i	displacement vector
U	open circuit potential of LFP (V)
x	spatial coordinate along the thickness of the cell
Z	atomic number

Greek letters

α	apparent transfer coefficient (kinetic parameter)
β	stress modeling parameter $\frac{\Omega(3\lambda+2\mu)}{3}$
γ	thermodynamic factor for variable solid state diffusivity model
δ_{ij}	Dirac delta function
ε	porosity
ε_{ij}	strain component
η	surface overpotential (V)
κ	electrolyte conductivity (S m^{-1})
λ	stress modeling parameter $\frac{2\nu\mu}{1-2\nu}$
μ	stress modeling parameter $\frac{E}{2(1+\nu)}$
ν	Poisson's ratio
ρ	density (kg m^{-3})
σ	conductivity of solid matrix (S m^{-1})

σ_{ij}	stress (Pa)
ϕ	electric potential (V)
τ	electrode tortuosity
Ω	partial molar volume ($m^3\ mol^{-1}$)

Subscripts

1	solid phase
2	electrolyte phase
a	anodic
app	applied current density
c	cathodic
e	electrolyte
eff	effective
ini	initial
h	hydrostatic stress
loc	local
LFP	lithium iron phosphate
max	maximum
s	solid/electrolyte interface
sep	separator
SOC	state of charge
pos	positive electrode

Superscripts

$+$	length plus epsilon
$-$	Length minus epsilon

List of Acronyms

APS	Advanced Photon Source
ANL	Argonne National Laboratory
BET	Brunauer Emmett and Teller
CBD	carbon-doped binder domain
CCCV	constant-current–constant-voltage
DEC	diethyl carbonate
EC	ethylene carbonate
EV	electric vehicle
FBP	filtered back projection
FEM	finite element method
FIB-SEM	focused-ion beam/scanning electron microscopy
LFP	lithium iron phosphate
LIB	lithium-ion battery
LCO	lithium cobalt oxide
LMO	lithium manganese oxide
LTO	lithium titanate oxide
MCMB	mesocarbon microbead

NCA	lithium nickel cobalt aluminum oxide
NMC	lithium nickel manganese cobalt oxide
NMP	1-methyl-2 pyrolidinone
OCV	open circuit voltage
P2D	pseudo two dimensional
PDE	partial differential equation
PVDF	polyvinylidene fluoride
RVE	Representative Volume Element
SEI	solid-electrolyte interphase
SEM	scanning Electron Microscopy
SOC	state of charge
TXM	transmission x-ray microscope
TGA	Thermogravimetric Analysis
XCT	X-ray computed tomography
XRD	X-ray diffraction

1. Introduction

1.1 Overview and Objectives

Since the introduction to the market in 1991, lithium-ion batteries (LIBs) have revolutionized portable electronics. They have offered an efficient energy storage system with high energy/power density and long cycle life suitable for cell phone and power tool applications. With the rising of environmental issues due to fossil fuel consumption, sustainable energy conversion and storage technologies has become important part in the development of modern societies. Extensive investigations have been conducted to integrate renewable energy sources such as solar, wind, and geothermal to the electrical grid. However, these sources of energy are intermittent in nature and require to be stored at the production time for the later supply, opening a new market for LIBs. In addition to portable electronics and grid energy storage, significant efforts have been directed toward electrifying the transportation sector to reduce air pollution from internal combustion engines. Battery's energy density is the key parameter that determines the driving range. Today's LIBs have superior gravimetric and volumetric energy densities typically 260 Wh/kg and 780 Wh/L closing to the ~300 miles per full of charge target required for large scale electrification of vehicles [1]. As the range of LIB's application continues to broaden, the battery's technology also needs to advance. Even though, the technology is currently mature enough to meet some market requirements for a variety of applications, there is still a crucial need to enhance performance including energy, power, cycle life, and safety [2,3].

Although these performance requirements are macroscopic and usually stated at cell or pack scale, they are to be addressed over multiple length scales with different material and electrode design strategies as shown in **Fig. 1-1** [4]. The design of active materials happens at atomic scale up to nano-scale where the material voltage, capacity, lattice stability, kinetic barrier, and transport property are designed. The electrode architecture design occurs from tenth of nanometer up to micro-scale, where the electrode lithium-ion transport path, surface area, deformation & fatigue, structural stability, and interface physics are designed. The design of electrodes pairing and cell level transport design usually happen from micro-scale up to one meter scale. In a LIB cell, electrochemical reaction occurs on nano scale and depends on the chemical and electronic properties of the material [5]. Charge and mass transport takes place from the material level to the electrode and eventually to the cell level. It also depends on the materials and electrode's structural properties. All these processes are strongly and nonlinearly coupled over different length scales. As a result, a mechanism at the nano/micro scale can dominantly effect the overall LIB behaviour. While significant research has been conducted to understand the chemical and physical behavior of materials at the nanoscale, there is a lack of understanding in the scientific community about what is exactly happening at the network of the particles scale or mesoscale. This could be related to the difficulty of experimentally observing the phenomena happening at this scale, especially in situ or in-operando [6].

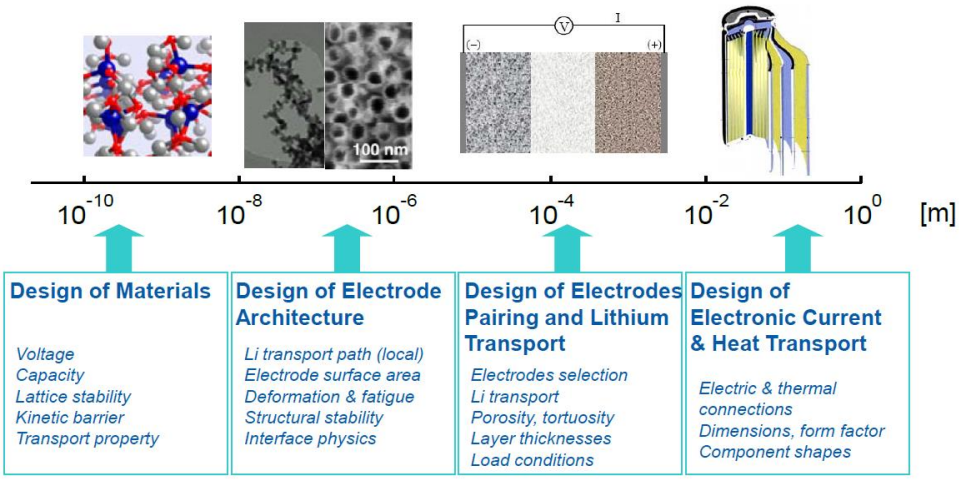

Figure 1-1. A diagram showing different length scale of LIB and its design requirements. Reproduced with permission from [4]

Motivated by the need to better understand the battery mesoscale behaviour, the field of 3D imaging for energy materials study has been advancing rapidly. Two common methods of visualizing electrode's structure are X-ray computed tomography (XCT) and Focused-ion beam/Scanning electron microscopy (FIB-SEM). Unlike FIB-SEM, XCT enables nondestructive 3D imaging in a rather short time with material penetration capability suitable for in situ and in-operando imaging [7]. Therefore, it has risen as the primary advanced imaging techniques for studying LIB internal structures. As will be discussed with more details in 2.3, XCT measures the interaction of X-rays with the electrode sample to reconstruct the internal local morphology of the materials. It provides visual and quantitative insights into the electrode's structure such as porosity, volume specific surface area, particle and pore size distributions, and transport properties.

In addition to quantitative morphological information, 3D reconstructed electrode's structures can be used as the computational geometry for multiphysics simulations. In this

way, a modeling framework that describes the multiphysics phenomena occurring during battery operation needs to be developed. The model links the electrochemistry, mass and charge transport, mechanical stress, and thermal response of the electrode to the real 3D electrode geometry. Such modeling studies are a promising approach to elucidate the complex multiphysics phenomena occurring during battery operation.

Moreover, they can be used in degradation and failure studies, helping to design strategies to improve LIB's cycle life. Computer simulations provide the heterogeneous distribution of physical and electrochemical properties within the electrode structure, contributing to performance loss. Similar to most materials, LIB electrode's failure depends on local imperfections and heterogeneities which is responsible for performance loss during battery cycling [8]. Therefore, to mitigate performance loss due to structural heterogeneities, more homogeneous electrode structures are favorable. The simulation could provide a guideline for gradual structural modification of particle morphology to achieve more homogeneous electrode [9]. This approach could furtherly improve the electrode's capacity fade and lead to the enhanced cycle life for next generation LIBs.

The objective of this PhD research has been the development of multiphysics mathematical models to simulate multiphysics behaviour of LIBs electrode based on 3D reconstructed structure. The models shed light on the interaction among chemistry, mass and charge transport, mechanics, and microstructural geometry during battery operation. As the geometry, all models take into consideration the electrode's 3D structure reconstructed from nano-scale XCT. The four principle stages of this PhD study have been: 1) development of a multiscale platform to model a commercial nano-structured $LiFePO_4$ (LFP) cathode for LIBs.

This multiscale framework consists of a microscale level where the electrode 3D microstructure behaviour is modeled and a macroscale level where discharge performance is simulated. 2) development of Representative Volume Element (RVE) model for a commercial nano-structured LFP cathode which is more computationally efficient compared to multiscale model. 3) morphological and electrochemical characterization of an in-house prepared nanostructure $Li_4Ti_5O_{12}$ (LTO) anode using two modes of XCT imaging: absorption contrast and Zernike phase contrast. 4) development of a diffusion induced stress model to investigate mechanical response of a commercial $LiMn_2O_4$ (LMO) cathode. The model includes 3D reconstructed active particles and carbon-doped binder domain (CBD) as the geometry. While first two models link the electrode's performance to the structural geometry of a nanostructured LFP cathode, the third stage involves morphological analyses of a nanostructure LTO anode. In addition, in the third stage, the RVE model developed in second stage was further improved by incorporating charge transport within the solid phase in the governing equations. Finally, the fourth stage lies within the simulations studies that employ electrode's reconstructed structure to relate structural degradation to the battery performance loss. This model considers a uniform CBD at the outer surface of reconstructed LMO active particles by employing image processing techniques and investigates the evolution of intercalation induced stress within the electrode structure.

1.2 Thesis Layout

This thesis includes 7 chapters wherein chapter 1 depicts the motivation and objectives of the overall studies along with the thesis layout. Chapter 2 reviews the background information

used in the next chapters. It starts with a brief introduction about LIBs working principle and different active material chemistries used in electrodes. Chapter 2 continues with the discussion of traditional modeling approaches to simulate the battery performance including curve fitting models, circuit based models, and homogeneous models such as single-particle and pseudo-2D models. Chapter 2 concludes with the explanation of XCT technology working principles and its advantageous over other imaging techniques. Chapters 3 to 6 consists of papers all of which I co-authored as principal lead author (Please refer to the statement of contributions included in the thesis).

Chapter 3 presents multiscale modeling of LIBs' electrodes based on nano-scale XCT data published by Kashkooli *et al.* [10] and is reproduced with permission from the Journal of Power Sources. In this chapter, a multiscale platform is introduced to model LIB electrodes electrochemical behavior based on the 3D reconstructed structure. This multiscale framework consists of a microscale level where the electrode microstructure architecture is modeled and a macroscale level where galvanostatic discharge/charge performance is simulated. For microscale geometry 3D microstructure is reconstructed based on nano-scale X-ray computed tomography data replacing typical computer generated microstructure. It is shown that this model can predict the experimental performance of a commercial LFP cathode at different discharge rates more accurately than the conventional homogenous models.

Chapter 4 introduces the RVE model of LIB electrodes based on XCT reconstructed geometry published by Kashkooli [11] and reproduced with permission from Journal of Applied Electrochemistry. In this chapter, a new model that keeps all major advantages of the single-particle model of LIB and includes 3D structure of the electrode is developed. Unlike

the single spherical particle, this model considers a small volume element of an electrode, called the RVE, which represents the electrode structure. The advantages of using RVE as the model geometry is demonstrated for a typical LIB electrode consisting of nano-particle LFP active material. The simulation results show that the distribution of lithium inside the electrode microstructure is very different from the results obtained based on single-particle model.

Chapter 5 studies morphological and electrochemical characterization of a nanostructured LTO anode using multiple imaging mode synchrotron X-ray computed tomography and is based on two works by Kashkooli *et al.* [12] and [13] which are reproduced with permission from Electrochimica Acta and The Journal of the Electrochemical Society, respectively. In this study, synchrotron X-ray computed tomography has been employed using two different imaging modes of absorption and Zernike phase contrast to reconstruct the real 3D morphology of a nano-structured LTO electrode for lithium-ion batteries. The inclusion of carbon-doped binder domain (CBD) in Zernike phase contrast mode provides an integrated percolated network of active material and CBD together, making it well-suited for continuum modeling.

Chapter 6 discusses synchrotron X-ray nano computed tomography based simulation of stress evolution in LMO electrodes published by Kashkooli *et al.* [14] which is reproduced with permission from Electrochimica Acta. In this study, synchrotron X-ray nano-computed tomography at the Advanced Photon Source in Argonne National Laboratory has been employed to reconstruct real 3D active particle morphology of LMO commonly used in LIBs. For the first time, CBD has been included in the electrode structure as a 108 nm thick uniform layer at the outer surface of active particles, using image processing techniques. With this

unique model, stress generated inside four LMO particles with a uniform layer of CBD has been simulated, demonstrating its strong dependence on local morphology (surface concavity and convexity), and the mechanical properties of CBD such as Young's modulus.

Chapter 7 summarizes the conclusions and provides recommendations for future work.

2. Background

2.1 Lithium-ion Battery Technology

A lithium-ion battery (LIB) consists of a positive and a negative porous electrode detached by a separator. The terms “positive electrode” for “cathode” and “negative electrode” for “anode” are used interchangeably throughout this dissertation. The porous electrode supports the electrochemical reaction happening in the battery for energy storage and the separator allows ions movement while preventing electron passage, see **Fig. 2-1**. The electrode in a LIB stores energy through three different mechanisms: (1) alloying e.g. silicon and tin [15],[16] ; (2) conversion e.g. Iron oxide and coppers oxide [17]; (3) intercalation e.g. graphite and lithium cobalt oxide. While alloying provides several times higher capacity compared to other mechanisms, it results in a huge material volume change [18] which limits the battery cycle life. Conversion requires nano-structured material to provide reversible reactions and is typically used with the alloying chemistries [17]. Intercalation is the most widespread mechanism for storing energy in both the anode and the cathode and broadly applied in commercial LIBs. The intercalation process entails a host material accommodating the lithium-ions inside its crystal structure. During charge, lithium de-intercalates from the positive electrode, is transported in the electrolyte, and intercalates into the negative electrode. During discharge, the process is reversed, with the lithium-ion intercalating inside positive electrode. The battery energy storage capability depends on the cell voltage and capacity. While the battery voltage is determined by the different combinations of anode and cathode materials, the battery capacity is determined by the capacity of cathode. This is because the

capacity of anode material is typically higher than the cathode, thereby, the cathode chemistry limits the overall battery capacity [17].

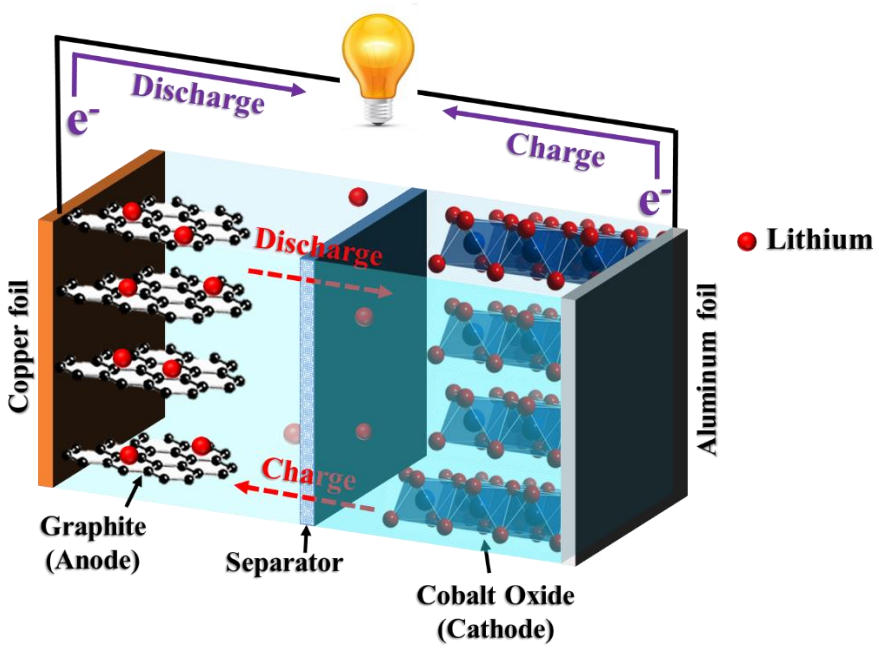

Figure 2-1. LIB's schematic with graphite as the anode and cobalt oxide as the cathode.

In the case of anode material, graphite is commonly used in commercial LIB because of low cost and good cycling stability. It offers the specific capacity of 350 mAh/g and experiences low volume change, below 10 percent, upon cycling [19]. Lithium Titanate Oxide ($Li_4Ti_5O_{12}$) or LTO is another promising alternative for the anode, offering high rate capability with almost zero volume change upon cycling which makes it suitable for vehicle application [20]. Other alternatives including, alloying silicon or Si/C composites are being extensively researched due to their significantly higher specific capacity. The higher capacity anode material leads to thinner anode usage which enhances the overall battery energy density. The

silicon theoretical capacity is 4200 mAh/g which is more than 10 times higher than graphite. Nevertheless, large volume changes upon cycling, has limited its large scale applications [21].

In case of the cathode, options are far wider and different materials provides various combinations of performance, durability, cost, and safety. Usually a lithium metal oxide is utilized as the cathode material. The most common ones are Lithium cobalt oxide ($LiCoO_2$) or LCO, Lithium manganese oxide ($LiMn_2O_4$) or LMO, Lithium nickel manganese cobalt oxide ($LiNiMnCo_2$) or NMC, Lithium nickel cobalt aluminum oxide ($LiNiCoAlO_2$) or NCA, Lithium iron phosphate ($LiFePO_4$) or LFP. LCO offers very high energy, limited power, and good cycle life [17]. It is a great choice for small portable electronics such as cell phones and laptops. However, it shows moderate charged state thermal stability which makes it unsuitable for EVs [1]. In addition, cobalt cost has increased by 70 percent recently which might challenge future applications of LCO. LMO has high power, very good thermal stability, and low cost; Nonetheless, its low capacity, limited cycle/calendar life limits its application to the power tools and electric motive power [22]. NMC provides very good combination of energy, power, cycle life, and thermal stability at charged state. Nickel has high specific energy, but low stability; Manganese has low cost and high stability, but low specific energy; and Cobalt has high activity, but is toxic; Combining these metals leads to lower cost and toxicity of NMC compared to LCO [23]. This makes NMC a promising candidate for both portable electronics and EV applications. Similar to NMC, NCA provides high energy and power with good thermal stability and cycle life. Due to presence of Aluminum, NCA offers higher energy and stability compared to NMC, which makes it an excellent choice for automotive and premium electronic applications[24]. The last cathode material discussed is LFP which in contrast to

the other cathode materials is not a metal oxide. LFP is a low cost material offering high power, very good thermal stability, and excellent safety and cycle life [25]. However, the low operating voltage of 3.3 V *vs.* Lithium, reduces LFP electrode's specific energy compared to the metal oxides counterparts. The main challenge of using LFP has been the low electronic conductivity which can be enhanced by nano-structuring and carbon coating of the active material [25]. LFP is mainly used in power tools and grid energy storage applications [26].

2.2 Lithium-ion battery models

In order to better understand LIB's physical and electrochemical behaviour different types of models have been developed. These models vary from simple empirical/circuit based models [27–29] to the homogeneous [30–34] and molecular dynamics models [35]. They also differ broadly in terms of complexity, computational cost, and reliability. Ideally, a model should predict the internal behavior of battery components at minimum computational cost. However, the inherent difficulty of LIB modeling is that it is a multiscale [36] multiphysics system. Multiple physical and electrochemical phenomena occur during LIB operation. These coupled physical and electrochemical phenomena are best described by complex non-linear partial differential equations that need to be solved numerically via Finite Element, Finite difference, Finite volume, and Boundary Element Methods. On the other hand, these multiphysics phenomena are happening over different length scales ranging from 1-nanometer to 1-meter scale, previously shown in **Fig. 1-1**. For example, in a LFP cathode, LFP nano-particles represent the smallest scale observed, secondary particles which are formed by those primary particles agglomeration of primary particles, represent the second size scale. The third size

scale is the positive electrode that consists of carbon conductive additive, polymeric binder and the secondary particles [37]. Simulation of a multiphysics system model that includes all those scales requires huge amount of memory.

Another challenge in modeling of LIBs is that it is impossible to obtain all the model parameters from the experimental data. There are limited number of available experimental data for transport properties relative to each chemistry in literature. In addition, those reported properties also vary greatly in value. This is because the materials have been synthesized using variety of methods and their properties have been measured using various experimental techniques. For example, in the literature, the diffusion coefficient of Lithium-ion inside LFP chemistry ranges from 10^{-17} to 10^{-22} m^2/s [38–40]. In order to determine unknown parameters, e.g. lithium-ion diffusion coefficient, the simulated performance voltage is compared against experimental data at a low C rate [32] (1C is the discharge current that discharge the entire battery in 1 hour). To determine the unknown parameter, it is varied to provide the best experiment/simulation fit. Then, the accuracy of the estimated parameter is confirmed against the available reported value in literature, if possible. In the following subsections, common LIB modeling approaches are briefly reviewed.

2.2.1 Curve fitting and Circuit based models

Curve fitting model provides an empirical correlation by fitting polynomial, exponential, power law, and logarithmic functions to the performance data, previously obtained by experiment. The model is used later to predict the future battery performance at various operating conditions [41]. Although the model can be used to predict cell performance, it

usually loses the accuracy outside the operating conditions in which it has been determined. The curve fitting approach lacks any physical meaning and fails to relate sophisticated multiscale multiphysics phenomena occurring during battery operation to the cell performance. The circuit based model describes the LIB using a circuit model that typically involves a combination of resistors, capacitors, voltage sources in parallel or series. The model various components value are determined in a way to provide the best fit against the battery impedance spectroscopy data [27],[42]. Current research in this area entails continuous updating of the model parameters during battery operation time using current and voltage data, see [27–29].

2.2.2 Single-particle model

Single-particle model describes the battery electrode by a single active particle and simulate the discharge/charge performance without considering the structure of the porous. Lithium-ion mass transfer is only modeled within the anode and cathode active particles and is limitated due to concentration variation and potential effects in the electrolyte being neglected [43–45]. Lithium diffusion is based on Fick's mass transport and electrochemical reaction is based on Butler-Volmer kinetics.

Table 2-1, summarize the governing equations used in single-particle model in which c_1 is lithium-ion concentration inside the active material particles, R_p is particle radius, $D_1$is lithium-ion diffusion coefficient in active material, j_n is pore-solid flux of lithium-ion, i_0 is exchange current density, k_0 is reaction rate constant, F is Faraday's constant, R is universal gas constant, T is Temperature, C_{1s} and C_{2s} are lithium-ion concentration in particle and

electrolyte at the solid/electrolyte interface, respectively; C_{max} is the maximum concentration of lithium inside the solid matrix, $\phi_1$is solid phase potential, and *U* is open circuit potential.

The single-particle model is a simplified model that allows the battery performance prediction at low to moderate C-rates operating conditions. The single-particle model provides computational efficiency over pseudo-two-dimensional (P2D), which makes it a suitable candidate for battery pack and large scale simulations. However, their results deviate from experiment for high C rates or for batteries having thick electrodes [43]. Particle groups model [46–49] can also be categorized in this sub-section. These models include lithium diffusion inside multiple, e.g. four [46], groups of active particles which are connected to the percolated network of the solid matrix. The governing equations are similar to **Table 2-1** in which each particle group has separate mass transfer equation and contributes to the total current density based on its individual particle size [47].

Table 2-1 Governing equations of single-particle model

Governing Equation	Boundary Condition
$\frac{\partial c_1}{\partial t} = \frac{1}{r^2}\frac{\partial}{\partial r}\left(r^2 D_1 \frac{\partial c_1}{\partial r}\right)$	$\left.\frac{\partial c_1}{\partial r}\right\|_{r=0} = 0$ $\left.\frac{\partial c_1}{\partial r}\right\|_{r=R_p} = -j_n D_1$
$j_n = \frac{I}{F} = \frac{i_0}{F}\left(exp\left(\frac{\alpha_a F}{RT}(\phi_1 - U)\right) - exp\left(-\frac{\alpha_c F}{RT}(\phi_1 - U)\right)\right)$	
$i_0 = F k_0 (c_{2s})^{\alpha} (C_{max} - C_{1s})^{\alpha} {C_{1s}}^{\alpha}$	

2.2.3 Pseudo-two-dimensional model

The P2D model is based on Newman's porous electrode theory [50] and employs concentrated solution theory to describe the internal behavior of a LIB cell comprising positive and negative porous electrodes with a porous separator in between. P2D is a detailed multiphysics model that includes several physical and electrochemical internal variables comprising the electrochemical potentials and lithium-ion concentration within electrode's pore and solid phases [30–34]. P2D has allowed researchers to study the effect of different operating conditions on battery performance without relying on costly experiments. The model has been widely utilized to optimize the electrode and separator structural design such as thickness, porosity, and electrode's active particle size [51], [52].

The P2D model is based on governing equation of mass and charge transport. It depicts the electrochemical behavior of a 1D battery in isothermal condition. The model includes a total of 10 governing partial differential equations (PDEs) in *x, r,* and *t,* across three regions of positive and negative electrodes, and separator, and are given in **Table 2-2** along with their corresponding boundary conditions. Here x represents the cell thickness direction and r is the particle radius coordinate. The boundary conditions at the electrode separator interfaces are given to satisfy continuity and conservation of flux, while the electrode-current collector interfaces are insulating conditions for all variables except the solid phase potential. The solid phase potential boundary conditions are dictated by the charging/discharge protocol considered. The governing equations for positive and negative electrodes are generally identical and differ only in the parameter values and correlations. The separator is void of active material, so all terms relating to the solid phase are absent. The first equation is obtained

from concentrated solution theory and mass balances of lithium-ion within the electrolyte phase. The second equation is the conservation of charge within electrolyte phase while the third equation is conservation of charge within the solid phase. The fourth equation is Fick's 2nd law of diffusion inside the solid particles (solid phase), which is analogous to governing equations of the single-particle model discussed in Section 2.2.2. Thus the P2D model can be seen as an extension of the single-particle model which accounts for variation across the electrodes and effects of the electrolyte.

In **Table 2-2**, ε is electrode porosity, c_2 is lithium-ion concentration in electrolyte, D_{eff} is effective diffusion coefficient, a is the volume specific surface area which is interfacial surface area per unit volume of electrode , and t_+^0 is the transference number of the lithium-ion in the solution, i_2 is current density in electrolyte, k_{eff} is effective conductivity of electrolyte, and f_2 is mean molar activity coefficient of electrolyte, *I* is total current density, σ_{eff} is effective conductivity of solid matrix.

Table

2-2 Pseudo two dimensional model

Governing Equations	Boundary Conditions
Electrode	
$\varepsilon \frac{\partial c_2}{\partial t} = \frac{\partial}{\partial x}\left(D_{eff} \frac{\partial c_2}{\partial x}\right) + a j_n (1 - t_+^0)$	$\left.\frac{\partial c_1}{\partial x}\right\|_{x=0} = 0$ $-D_{eff,e} \left.\frac{\partial c}{\partial x}\right\|_{x=l_e^-} =$ $-D_{eff,s} \left.\frac{\partial c}{\partial x}\right\|_{x=l_e^+}$
$\frac{\partial \phi_2}{\partial x} = -\frac{i_2}{k_{eff}} + \frac{RT}{F}(1 - t_+)\left(1 + \frac{\partial ln f_2}{\partial ln c_2}\right)\frac{\partial ln c_2}{\partial x}$	$\left.\frac{\partial \phi_2}{\partial x}\right\|_{x=0} = 0$ $-\kappa_{eff,p} \left.\frac{\partial c}{\partial x}\right\|_{x=l_e^-} = -\kappa_{eff,s} \left.\frac{\partial c}{\partial x}\right\|_{x=l_e^+}$
$I - i_2 = -\sigma_{eff} \frac{\partial \phi_1}{\partial x}$	$\left.\frac{\partial \phi_1}{\partial x}\right\|_{x=0} = -\frac{I}{\sigma_{eff}}$ $\left.\frac{\partial \phi_1}{\partial x}\right\|_{x=l_e^-} = 0$
$\frac{\partial c_1}{\partial t} = \frac{1}{r^2}\frac{\partial}{\partial r}\left(r^2 D_1 \frac{\partial c_1}{\partial r}\right)$	$\left.\frac{\partial c_1}{\partial x}\right\|_{r=0} = 0$ $\left.\frac{\partial c_1}{\partial x}\right\|_{r=R_p} = -j_n D_1$

$$j_n = \frac{I}{F} = \frac{i_0}{F}\left(exp\left(\frac{\alpha_a F}{RT}(\phi_1 - \phi_2 - U)\right) - exp\left(-\frac{\alpha_c F}{RT}(\phi_1 - \phi_2 - U)\right)\right)$$

$$i_0 = Fk_0(c_{2s})^{\alpha}(C_{max} - C_{1s})^{\alpha}{C_{1s}}^{\alpha}$$

Separator	
$\varepsilon\frac{\partial c_2}{\partial t} = \frac{\partial}{\partial x}\left(D_{eff}\frac{\partial c_2}{\partial x}\right)$	$c\|_{x=l_e^-} = c\|_{x=l_e^+}$ $c\|_{x=l_e+l_s^-} = c\|_{x=l_e+l_s^+}$

Although single-particle and P2D models are developed based on multiphysics phenomena happening inside the battery, they typically use simple spherical particle or computer generated particles as the modeling geometry. Therefore, complex morphology of real electrode's active particles and structure casts doubt on some of the physical and electrochemical findings of these models. Combining the multiphysics phenomena with the electrodes 3D reconstructed structure, using FIB-SEM or XCT, can provide reliable insight on the LIBs physical and electrochemical behaviour. In the present thesis, nano-XCT technology has been employed to obtain 3D visualization of the electrode. The following sub-section briefly describe XCT working principles and reviews its application to LIB.

2.3 X-ray Computed Tomography

2.3.1 Working principles

For most people X-ray computed tomography (XCT), also known as CT-scan (computed tomography-scan), is dedicated for medical application to visualize internal parts of human

body. Nowadays, the application of XCT has being extended to other science fields including natural science, material science, and geology [8], [53,54]. Although the technique was commercialized in 70's, in the past 10 years with the development of nano scale laboratory and synchrotron radiation tomography, has been revolutionized. XCT offers unique characterization features including high resolution, high sensitivity, fast imaging, and matter penetration leading to its broad application in the nano-material research. Using XCT, there is no need for tedious sample preparation methods such as polishing and imaging of very brittle samples could be easily handled. It is a non-destructive technique, suitable for in-situ and in-operando studies [55–57]. New XCTs provide 3D images with a spatial resolution up to 20 nm (20 nm^3 voxels) [58] which makes them an invaluable imaging tool in the same respect as electron microscopes such as scanning electron microscopy (SEM) and transmission electron microscopy (TEM). Nevertheless, there is still a spatial resolution gap between electron microscopes and XCT which needs to be narrowed [59].

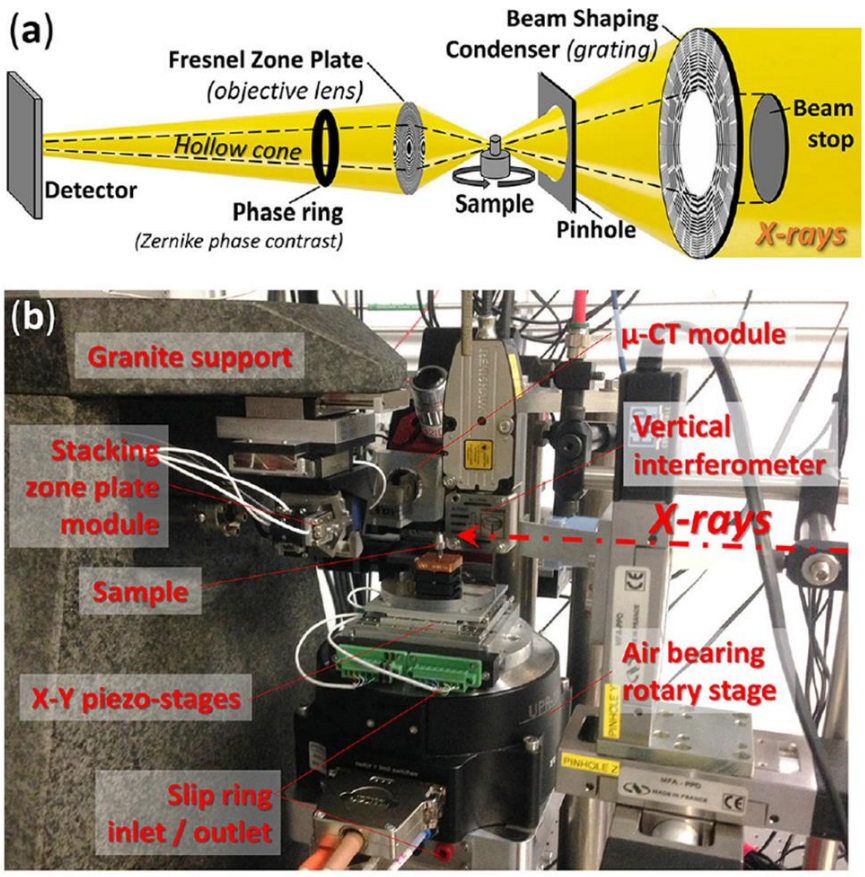

Figure 2-2. (a) schematic of operation principle of transmission x-ray microscope (TXM) used for nano-XCT (b) photograph of TXM at sector 32-ID of the Advanced Photon Source of the Argonne National Laboratory, reproduced with permission from SPIE publishing [59]**.**

Two XCT instruments have been employed for this dissertation: 1) laboratory nano-XCT at Carnegie melon university called UltraXRM-L200 (also known as Ulta-800, Carl Zeiss X-ray Microscopy-formerly Xradia, Inc., Pleasanton, CA, USA) and 2) transmission x-ray microscope (TXM) at the advanced photon source (sector 32-ID) of the Argonne National Laboratory. In order to achieve nano-scale resolution, laboratory and synchrotron XCT instruments employ lens-based systems. Laboratory nano-XCT devices employ an X-ray tube

with high voltage to collide electrons on to a metal target anode, e.g. copper. They typically generate X-rays with relatively low energy of ~8 keV [60]. Synchrotron X-rays are electromagnetic waves generated by high energy electrons in particle accelerators which can easily reach to GeV energy level. Their advantages over laboratory X-rays include higher penetration depth and high degree of monochromacity. Therefore, in addition to imaging, synchrotron X-rays are also employed in crystallography, diffraction, scattering, and various spectroscopy characterizations. **Fig 2-2** shows schematic and real photograph of Transmission X-ray Microscope (TXM) in Advanced Photon Source of the Argonne National Laboratory. The operation principle of TXMs are similar to optical visible light microscopes. First, the tunable X-ray passes through a mono-capillary condenser lens to effectively focus on the sample. After passing through the sample a Fresnel Zone Plate is used to focus and magnify the images on to the detector. The sample is placed on a rotary stage that enables the imaging over 180° and makes nano-XCT imaging possible. Reconstruction algorithms are later used to generate 3D images.

Two XCT imaging modes are currently used in material research: absorption contrast and Zernike phase contrast. In absorption contrast, the contrast is generated via transmitting an X-ray beam through the sample and capturing the resulting attenuated beam on a detector. The amount of X-ray absorption is dependent on the sample atomic number, *Z*, density of the material, ρ, and the X-ray photon energy, E_p. The X-ray attenuation is proportional to $Z^3\rho/{E_p}^3$ [61]. In addition to absorption contrast, low contrast, soft materials such as carbon and organic materials with low Z, can be imaged using Zernike phase contrast ring. For this a

gold ring is used to detect the phase shift of the x-ray passing through the sample, see **Fig. 2-2a**. Once a large enough number of tomograms are taken to acquire the desired nano-scale resolutions (between 720 to 1500 tomograms over 180 degrees recorded [59]), the 3D image is reconstructed employing filtered back projection (FBP) , see **Fig. 2-3**.

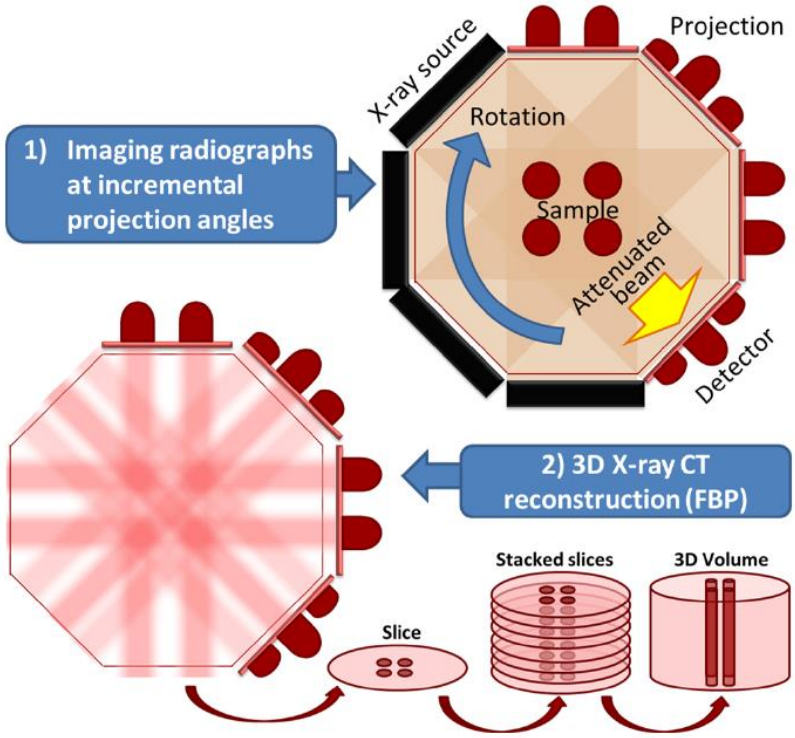

Figure 2-3. Generating volumetric imaging using nano-XCT, reproduced from [62]**, open access reference.**

An XCT 2D image is typically called a tomogram or slice as it corresponds to a slice from a loaf of bread (Tomos is the greek word meaning cut or section). Similar to a slice of bread having thickness, an XCT slice also has a specified thickness of the object being imaged. Therefore, as *pixels* (picture elements) form a typical digital image, *voxels* (volume elements)

form a 3D volumetric image. The schematic in **Fig. 2-3** represents the process of making a sample's 3D volumetric image using laboratory XCT. The 3D image is reconstructed computationally based on several 2D tomograms using reconstruction algorithms. 2D radiographs are generated by passing the X-ray through the sample at many projections around it while the sample is rotating. The following sub-section highlights the important studies related to the XCT application in the LIB research.

2.3.2 LIB application

In case of XCT application to LIB , for the first time in 2010 Shearing group [53] reconstructed a 3D structure of a commercial graphite electrode using a laboratory scale XCT with spatial resolution of 480 nm. The authors divided the electrode's volume into sub-volumes of various sizes to determine each sub-volume porosity, tortuosity, and volume specific surface area as a function of size. Based on their results, they could suggest a representative volume element (RVE) for the analyzed electrode sample. Later, they applied the same methodology to assess microstructural heterogeneity within a nano-structured LFP electrode using synchrotron XCT with resolution of 20 nm [63]. In this way, they employed a novel approach to quantify tortuosity based on heat-mass transfer analogy and found that tortuosity depends substantially on the direction measured, which negates a single scalar tortuosity assumption commonly used in homogeneous models. A similar study was conducted on a mesocarbon microbead (MCMB) electrode by Tariq *et al.* [64] to calculate the volume specific surface area, volume connectivity, and tortuosity using synchrotron nano-XCT with the spatial resolution of 16 nm. They found the tortuosity to be in the range of 2 to 7 for the solid and pore phase domain

respectively, confirming the presence of significant structural heterogeneity within the electrode microstructure. Furthermore, they showed that small particles are dispersed between large particles leading to increased electrode tortuosity. The highly tortuous electrode leads to the heterogeneous distribution of lithium-ion within the electrode's solid domain. This could accelerate local material failure during battery cycling. Ebner *et al.* [65] employed synchrotron XCT with resolution of 370 nm to a NMC electrode to characterize the influence of using different calendering pressure on the electrode's performance. They showed that higher pressure leads to less electrode porosity. However, the resulting high rate discharge capacity showed no dependency to the applied pressure, confirming that the capacity is limited by electronic rather than ionic conductivity.

In addition to morphological analysis, XCT has offered the capability of linking 3D electrode structure to the electrochemical performance. In this way, a computer model uses the XCT reconstructed structure as the geometry and governing equation of mass and charge transport to simulate the electrochemical performance. The simulation provides the detail study of electrochemistry, mass and charge transport, mechanical stress, and thermal behavior within the electrode's structure. For example, Yan *et al.* [66] simulated the discharge behavior of a LCO electrode based on nano-XCT reconstructed geometry. Their results show that the distribution of electrolyte concentration, current density, over potential, and intercalation reaction rate are very different from the results obtained from P2D model. Moreover, they showed that microstructure heterogeneity is responsible for the cell performance loss specially at high discharge rates. Using micro-XCT, Chung *et al.* [67] showed that electrode's particle size polydispersity inside a LMO electrode impact the local chemical and electrical behaviour.

Their results demonstrated that at low rates polydispersed particle distribution delivers up to two times higher energy density compared to computer-generated monodispersed particles; However, at high rates, monodispersed particle size distribution delivers higher energy and power density. This can be attributed to the higher volume specific surface area of monodispersed particle size.

As highlighted earlier in Chapter 1, XCT has enabled the investigation of electrode's mechanical response using 3D reconstructed structure. Lim *et al.* [68] were the first who employed reconstructed particle structures as model geometry for calculating diffusion-induced stress inside LCO and graphite particles. They calculated stress within both reconstructed and simple spherical particles and showed the stress level is several times higher in reconstructed particles compared to spherical particle with the same volume. Their results revealed that diffusion-induced stress is highly depended on the geometrical characteristics of the particles, highlighting the importance of including real particle geometry in the electrode's mechanical behavior studies. Their results motivated the study conducted in Chapter 6, to further improve the model's geometry by inclusion of CBD at the outer surface of the reconstructed particles. This enables the investigation of stress level within the electrode's reconstructed active particle and surrounding CBD at the same time.

3. Multiscale modeling of lithium-ion battery electrodes based on nano-scale X-ray computed tomography

This chapter is reprinted in adopted form with permission from Journal of Power Sources:

A.G. Kashkooli, S. Farhad, D.U. Lee, K. Feng, S. Litster, S. K. Babu, L. Zhu, Z. Chen, Multiscale modeling of lithium-ion battery electrodes based on nano-scale X-ray computed tomography, Journal of Power sources, 2016, 307, 496-509.

3.1 Introduction

As mentioned earlier in Chapter 1, lithium-ion batteries (LIBs) have attracted a tremendous attention because of their high energy/power density and long cycle life. Recently, automotive industries have put considerable effort to accelerate electrification of vehicles using LIBs [69,70]. For this purpose, among different candidates for cathode material, $LiFePO_4$ (LFP) is believed to be promising choice due to its low price, superb safety, and enhanced rate capability [71–73]. In addition to material selection, the electrode architecture also plays a crucial role in improving the performance of LIBs [64,74]. The microstructure of LIB electrode remarkably influences the performance by providing certain interfacial surface area, lithium-ion diffusion path, and active material connectivity [65,73], which particularly critical in automotive applications where the demands of energy and power densities are high [69].

The development of next generation high performance LIBs requires close relation between modeling and experiment. Mathematical models have been used to address physical and electrochemical processes occurring inside the battery and further employed to optimize

electrode design. However, traditional models still rely on a simplified picture of homogenous electrode which do not provide sufficient information about the electrode's real microstructure. Newman and co-workers have developed one of the most successful LIB models based on the porous electrode and concentrated solution theory [30,52]. Newman's pseudo-2D (P2D) model, previously introduced in 2.2.3., assumes that the porous electrode is made of equally sized, isotropic, homogenous spherical particles [30]. This homogenous description of electrode structure results in smooth, uniform intercalation/de-intercalation of lithium inside the host materials and has proven to be successful in characterizing discharge/charge behaviors particularly at low to moderate rates [75,76]. Although P2D model assumptions are not preserved in real LIB porous electrodes, it is widely applied in a variety of LIB research due to its simplicity [77–79]. This includes the rate capability and design investigation [43,52] as well as thermal behavior [80–82] studies. However, it fails to predict the phenomena related to inhomogenious structure of the electrode microstructure such as performance drop at high rates [83,84]. In addition, the well-known method of estimating the specific surface area based on spherical particles and the electrode tortuosity using Bruggeman relation has been controversial [8,85]. Therefore, in order to have more genuine insight in LIBs research, there is a crucial need for an advanced model capable of simulating LIBs behavior based on the electrode 3D reconstructed microstructure.

Recent advances in the X-ray computed tomography (XCT) have made nano-scale 3D microstructures capturing a reality. Nano-XCT offers the capability to non-destructively resolve the 3D structure of porous electrodes as it provides a high spatial resolution 2D stack to computationally reconstruct a 3D image of the electrode microstructure. The obtained 3D

geometry could be an alternative to commonly used computer-generated geometries [83,86] in LIB 3D models. As briefly discussed in 2.3.2, LIBs research involving XCT can be categorized into two general groups: the morphological studies and multiphysics modeling. The first group is dedicated to characterizing the 3D microstructure, particle distribution, pore scale morphological and transport properties analysis [8,68,87]. The second group, on the other hand, utilizes reconstructed 3D microstructure to simulate multiphysics phenomena occurring inside the cell such as discharge/charge performance [66], thermal behavior [88] and stress analysis [68]. Yan *et al.* [66] simulated the discharge behavior of $LiCoO_2$ (LCO) based on nano-XCT data. Their results show that the distributions of electrolyte concentration, current density, over potential and intercalation reaction rate are significantly different from the results obtained from the P2D model. Furthermore, the microstructure inhomogeneity is found to be responsible for the performance loss particularly at high discharge rates. Lim *et al.* [68] modeled diffusion-induced stress inside LCO particles which were reconstructed using XCT. Their results demonstrated that the highest von Mises and Tresca stresses in a reconstructed particle are several times greater than those obtained from the simple spherical or ellipsoid particle with the same volume. Yan *et al.* [88] simulated the heat generation during galvanostatic discharge in LCO microstructure. Their results show that the simulation based on reconstructed microstructure predicts more heat generation than the P2D model at high discharge rates. The simulation based on the reconstructed microstructure commonly results in the wider distribution of physical and electrochemical properties. The authors attributed the higher predicted heat generation to this wider electrochemical properties distribution. Chung *et al.* [89] studied the electrochemical and chemo-mechanical response of $LiMn_2O_4$ (LMO)

cathodes based on the XCT method. Their simulations show that particle size polydispersity of microstructures impacts the local chemical and electrical behavior of a porous electrode.

In this chapter, we aim to develop a model based on the 3D reconstructed microstructure of the electrode. Among different candidates, LFP was chosen as the focused technology due to the aforementioned reasons. Applying the above mentioned method on the electrode with nano-particles, e.g. LFP, to study multiphysics phenomena, poses the inherent multiscale difficulty involved in the LIB research [36]. Typically, models involve electrode's microstructure, study LIBs behavior in two different length scales simultaneously; the first scale is in the range of the particle size which is couple of micrometers in case of LCO and LMO and tenth of nanometers for LFP. In this work, this scale is called "microscale" wherein electrode's reconstructed structure is included. The second scale is in the range of the electrode thickness, typically 100 micrometers, where discharge/charge is characterized and here is called "macroscale". For a micro-particle electrode, the model length scale is from 10^{-6} to 10^{-2} m considering both microscale and macroscale. However, the scale is from 10^{-8} to 10^{-2} m for a nano-size particle. Thus, the length scale range is two orders of magnitudes higher in case of an electrode with nano-particles compared to the electrodes made of micro-particles. When running the 3D simulation, this requires around 10^{6} times more mesh elements that would burden a huge extra computational cost on the model simulation. To avoid this, the concept of multiscale modeling has been employed to investigate LFP electrode behavior [36,90–92]. First, the electrode microstructure was reconstructed based on the nano-XCT data and the intercalation flux were obtained based on the simulation results on microscale. Then, the intercalation flux was exported to the macroscale to update the state variables such as electric

potentials and specious concentrations in macroscale. Finally, the intercalation flux is updated based on the recent updated variables and sent back to microscale domain [93]. The link between microscale and macroscale is accomplished through coupling of equations at two sub-scales simultaneously [93], meaning that all the governing equations are solved concurrently in two scales and state variables are transferred between them in real time. To couple sub-scale models, another approach reported in the literature is serial coupling [94]. In the serial coupling, a surrogate-based model is determined from the pre-processed simulation data carried out on the microscale. The surrogate model is obtained based on the numerical experiment performed on microscale. For this, a quasi-steady state simulation of the governing equation is performed based on an experiment design for the initial values of state variables. Then, to couple the two scales, database and look up table [95,96] approach is used to couple microscale with macroscale. Although using serial method diminishes computational time, it includes error due to uncertainty in fitting the empirical model to microstructural data. In addition, the assumption of quasi steady state in microscale is highly questionable in a mainly time dependent model.

In this chapter, an advanced imaged-based multiscale computational framework capable of modeling LIBs is established. The modeling simulation results are presented for an LFP cathode scanned by a nano-XCT device and processed/reconstructed by a commercial software Simpleware 7 (Synopsys, Mountain View, USA). To achieve accurate results, a concurrent multiscale model is implemented in COMSOL Multiphysics® 5.0 software.

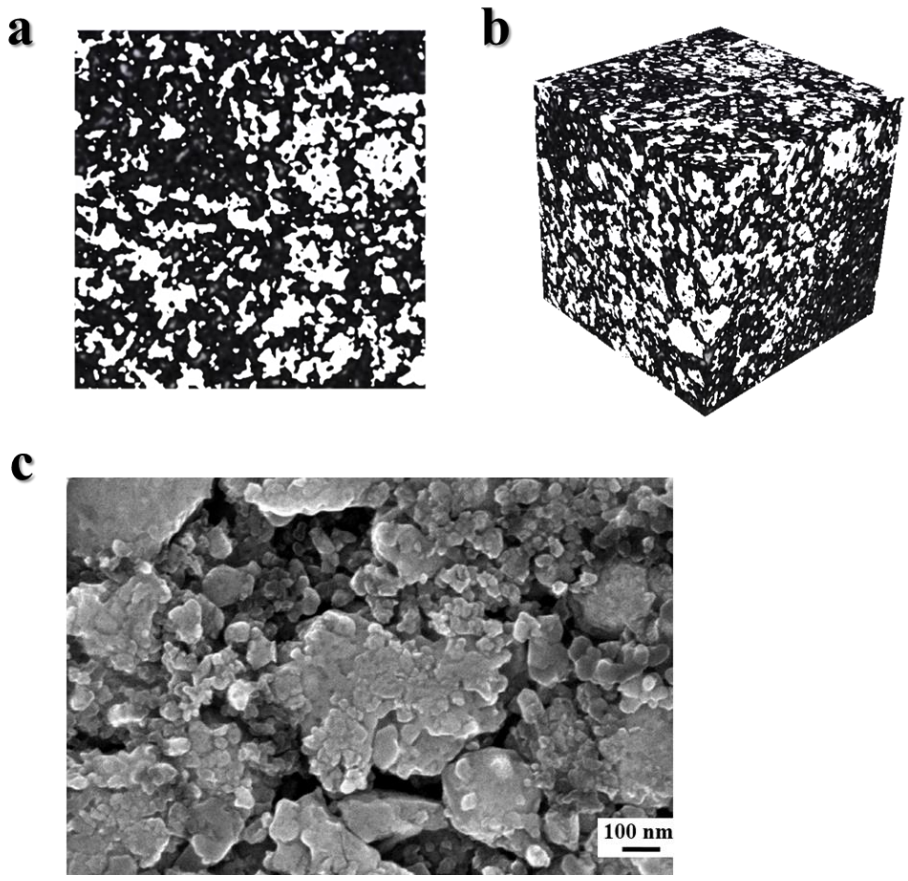

Figure 3-1. Different morphological images of a commercial LFP (a) Nano-XCT tomogram, 5 µm each side (b) Reconstructed structure, 5 µm each side (c) SEM image, scale bar is 100 nm.

3.2 Electrode structure reconstruction

The LFP sample used in this study is from a commercial LFP/graphite cell which was disassembled in an argon filled glove box (H_2O < 0.5 ppm, O_2 < 0.5 ppm). Since the Aluminum current collector affects the XCT scan, it was detached from the electrode by soaking in 6 molar KOH solution [66]. The sample was imaged using nano-XCT (UltraXRM-L200, Xradia Inc., Pleasanton, CA) at Carnegie Mellon university [97]. A high resolution scan of the region of interest with 50 nanometers spatial resolution and 16 µm field of view was

performed. A total of 990 tomograms were obtained by rotating the sample over 180° with 16 nm distance between slices. Then, the obtained 2D stack was segmented using binary thresholding technique to convert greyscale stack to binary stack. Eventually, 3D morphology of the LFP nano particles was reconstructed based on the 2D stack by ScanIP 7 (software in Simpleware package).

Fig. 3-1a shows a 2D raw morphology of the electrode microstructure based on a 2D tomogram obtained from 2D stack after segmentation. **Fig. 3-1b** shows the reconstructed 3D microstructure of the electrode consists of cluster of particles and **Fig. 3-1c** represents the SEM image of electrode nano-particles. In **Fig. 3-1a** and **3-1b**, the black region consists of cluster of active material particles whereas white region includes pore, additives comprising polymer binder (PVDF) and conductive carbon material. Since X-ray is highly sensitive to the atomic number, low atomic number additive phases could not be captured with one run of imaging. To distinguish different phases, two modes of imaging are needed: absorption contrast which capture active material and Zernike phase contrast that detects active material along with solid phase additives. Details of the method of distinguishing various electrode regions can be found in Ref. [98]. In this work, additives are not considered separately from the active material because it is hard to clearly distinguish them from active material. Moreover, treating them as separate regions requires an excessive computational load. It is shown that if the weight percentage of active material is high, the carbon material and polymer binder are distributed randomly in the electrode [99]. The weight percentage of active material in the current electrode is 90 percent obtained by Thermogravimetric Analysis (TGA) [100]. Hence, we assumed that the low percentage carbon material is randomly distributed among

the active material to provide electronic connectivity. For this, a growing region image processing algorithm with the width of one pixel was applied on the active material region to provide fusion of neighbouring active material together. Before this, unwanted noise was removed using recursive Gaussian filter with cubic Gaussian sigma value of 1. Gaussian sigma is a parameter that determines how many neighboring pixels should contribute to the smoothing operation of corresponding pixel. The obtained 3D reconstructed microstructure pore volume became 40% after filtering and image processing improvement which came in agreement with the 35% porosity of the real electrode obtained by Brunauer Emmett Teller (BET) measurement. The difference could be attributed to the unconnected pores which cannot be detected by BET.

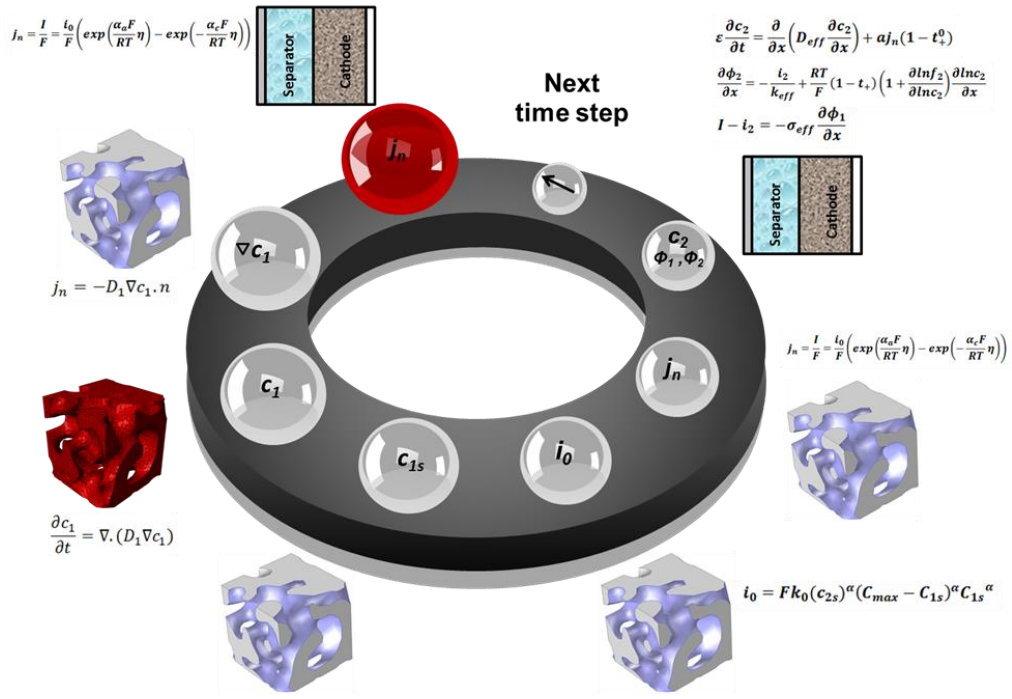

Figure 3-2. Multiscale modeling framework.

3.3 Experiment

For validation of the model, several coin cell (half-cells) were fabricated from the LFP cathode of the disassembled commercial LIB. Since LFP had been coated on both side of an aluminum sheet, the LFP coated on one side was removed using a cotton-based wipe soaked in 1-methyl-2 pyrolidinone (NMP) and scotch tape. To make the coin half-cells circular cathodes with area of 1.13 cm^2 were punched and coin cells (LIR2032-type) were assembled with a lithium metal foil as the counter electrode and an ion permeable separator (Celgard 2500). The electrolyte is 1M lithium hexafluorophosphate ($LiPF_6$) in 1:1 ethylene carbonate (EC): diethyl carbonate (DEC) and sealed before removal from the glove box. The cells then were tested on a battery cycler (Neware CT-3008-5 V10 mA). All cells were first cycled five times for the formation stage with a constant-current–constant-voltage CCCV protocol [46] on charge (CC at C/5 between 2.5 and 4.2 V and CV until I < C/25) and a 30 minutes period of rest, followed by CC discharge between 4.2 and 2.5V versus Li electrode. Then, in order to estimate the equilibrium potential, a fully charged electrode was discharged at CC at C/25 and the result is presented in **Table 3-3**. The rate-capability tests were accomplished on the coin half-cell setup by galvanostatic charge/discharge at C-rates ranging from C/25 to 4C between 2.5 and 4.2 V versus Li electrode. For all rates, CCCV protocol was used for charge (CV until I <C/25) to make sure the cathode came back to a fully charged state.

3.4 Modeling and Computer Simulation

Multiscale model development of the LIB half-cell based on the 3D reconstructed structure is presented in this section. This includes the geometries and governing equations on 3D

microscale and 1D macroscale domains along with the bridging between two scales. The microscale geometry is a Representative Volume Element (RVE) of the total reconstructed electrode. The macroscale is a 1D sandwich model of Li foil | separator | cathode to simulate half-cell charge/discharge performance. As discussed in 3.1, to couple the state variables such as electric potentials and specious concentrations between two scales, concurrent approach is used. Bridging is accomplished through transferring the calculated intercalation flux on the macroscale as the boundary condition for microscale. Then, the governing equations in microscale are solved to update the lithium concentration inside the microstructures and to calculate the new intercalation flux. Next, the intercalation flux is sent back to the macroscale, which is later used in the governing equations on the macroscale domain to update the state variables. The updated state variables in the macroscale are then used to update the intercalation flux which in the next time step is applied as an interfacial boundary condition in the microscale domain. This circular coupling, which is illustrated in **Fig. 3-2**, continues during the cell operation time. The coupling details will be further discussed in 3.4.4.

3.4.1 Microstructure selection

As discussed in the introduction, the reason that multiscale approach was chosen is due to the presence of LFP nano-particles which creates complicated microstructure, see **Fig. 3-1**. In order to choose appropriate microstructure we apply the concept of RVE which represents a portion of the electrode as a cluster of particles [101]. Majdabadi *et al.* [33] showed that the largest particle radius in the commercial LFP battery, which is similar to the one we disassembled, is around 169 nm. The particles with the size of 169 nm, allocate around 10%

(volume) of the active electrode material. Accordingly, we calculated the smallest volume of the electrode that has at least one particle with the largest size. We achieved a cubic RVE with sides of 728 nm which is the largest characteristic size of the microstructure.

Another approach to find the smallest RVE size is to calculate the electrode properties for a small cubic subdivision of the electrode sample. The subdivision size then will be increased until electrode properties e.g. porosity ε and specific interfacial surface area per unit volume of electrode a, remain within an acceptable range. **Table 3-1** shows porosity and specific surface area per unit volume for various cubic subdivisions using ScanIP. As mentioned previously, the domain porosity is around 0.4. For the sizes above 707 nm, when the subdivision size increases, the porosity of the subdivisions remains within the 3% of the domain porosity. On the other hand, the average specific surface area of the electrode is around 3.6 (1/ μm) where it remains within the 9% of the domain specific surface area for the subdivisions above 707 nm. Using the results of both approaches, a RVE with 750 nm each side from reconstructed microstructure was chosen for the current simulation.

Table 3-1. Porosity and specific surface area per unit volume for cubic subdivisions of the electrode sample with different size using ScanIP 7 (Simpleware, HO, Exeter, England)

Cube side (nm)	Porosity, ε	Specific surface area, a (1/ μm)
2122	0.41	3.62
1415	0.36	3.59
1132	0.42	3.73

849	0.42	3.71
707	0.39	3.51
566	0.35	4.27
424	0.6	4.92
283	0.58	4.87

3.4.2 Governing equations in macroscale

In this sub-section, the governing equations of mass and charge transfer are developed for each component of the 1D cell structure in macroscale, including the LFP porous cathode, a porous and ion permeable membrane separator, Li foil counter electrode, and the electrolyte that fills the cathode and separator pores. During discharge electrons flow in the external circuit from lithium foil to the cathode current collector and lithium-ions travel through the separator to the cathode. The following electrochemical reaction happens during the discharge and charge process:

Positive Electrode:

$$xLi^+ + xe^- + Li_yFePO_4 \rightleftharpoons Li_{x+y}FePO_4 \tag{3-11}$$

Negative Electrode:

$$Li \rightleftharpoons Li_{(1-x)} + xLi^+ + xe^- \tag{3-2}$$

The mathematical model employed to simulate macroscopic 1D half-cell LIB is based on the porous electrode theory [50,102,103]. For the transport of lithium-ions inside the electrolyte concentrated solution theory is used which can be written as:

$$\varepsilon \frac{\partial c_2}{\partial t} = \frac{\partial}{\partial x}\left(D_{eff} \frac{\partial c_2}{\partial x}\right) + a j_n (1 - t_+^0) \tag{3-3}$$

Where c_2 is the concentration of lithium inside electrolyte, D_{eff} is effective diffusivity, j_n is the pore-solid flux of lithium ions, and t_+^0 is the transference number of the lithium ion in the solution which is assumed to be constant in this work. The subscripts *i* = 1, 2 are the solid and electrolyte phases, respectively. The governing equations in the macroscale are similar to the ones in the P2D model. However, the model properties are calculated using the real specific surface area, a , and the effective diffusivity, D_{eff} as described in ref. [63].

The effective diffusivity is defined as [63]:

$$D_{eff} = D \frac{\varepsilon}{\tau} \tag{3-4}$$

Where D is the intrinsic diffusivity and τ is the electrode tortuosity which accounts for the obstruction to diffusion by porous network. Generally, in traditional LIB modeling tortuosity is calculated using Bruggeman correlation [30,31,52]. However, Bruggeman derived the correlation for a specific structure containing spherical particles which is not the case for diverse morphology of LIB active materials [63]. In order to calculate the tortuosity, using heat and mass transfer analogy, the steady state conductive heat transfer was simulated on both pore network and active material microstructure. The temperature distribution was obtained within the pore network by applying temperature gradient in x, y, z directions separately. To calculate the tortuosity, results obtained from the pore network must be compared to the one obtained through a uniform, non-porous sample with the same dimensions as discussed in ref. [63] by cooper *et al*. **Table 3-2** represents directional tortuosity

and its average value based on the stationary heat transfer simulation. Electric potential in the solution ϕ_2 is represented by Ohm's law as:

$$\frac{\partial \phi_2}{\partial x} = -\frac{i_2}{k_{eff}} + \frac{RT}{F}(1 - t_+)\left(1 + \frac{\partial lnf_2}{\partial lnc_2}\right)\frac{\partial lnc_2}{\partial x} \quad (3\text{-}5)$$

where i_2 is current density in the electrolyte, k_{eff} is effective conductivity, R is the universal gas constant, T is temperature, F is Faraday's constant, and f_2 is mean molar activity coefficient of electrolyte and is assumed to be constant. Since tortuosity is a geometric characteristics of the electrode, it is not related to the transport processes. Therefore, k_{eff} can also be calculated using **eq. (3-4)** by replacing diffusivity, D with conductivity, k using tortuosity values listed in **Table 3-2**.

Table 3-2. Directional tortuosity of both solid and electrolyte phase of the studied LFP cathode.

Region	Volume fraction	τ_x	τ_y	τ_z	τ_{avg}
Solid phase	0.6	1.6116	1.8154	1.7794	1.7311
Electrolyte phase	0.4	2.2544	2.4289	2.0844	2.2472

This is also valid for all upcoming effective parameters. The electric potential in the solid phase, ϕ_1, is described using Ohm's law in solid as follows:

$$I - i_2 = -\sigma_{eff}\frac{\partial \phi_1}{\partial x} \quad (3\text{-}6)$$

Where, I is superficial current density, σ_{eff} is effective conductivity of solid matrix.

The lithium ion intercalation reaction in the solid matrix is estimated from the Buter-Volmer equation as:

$$j_n = \frac{I}{F} = \frac{i_0}{F}\left(exp\left(\frac{\alpha_a F}{RT}\eta\right) - exp\left(-\frac{\alpha_c F}{RT}\eta\right)\right) \quad (3\text{-}7)$$

Where, η, is the surface overpotential defined as:

$$\eta = U - \phi_1 - \phi_2 \quad (3\text{-}8)$$

And i_0 is the exchange current density defined as [30]:

$$i_0 = Fk_0(c_{2s})^{\alpha}(C_{max} - C_{1s})^{\alpha}{C_{1s}}^{\alpha} \quad (3\text{-}9)$$

Where, k_0 is a reaction rate constant, C_{1s} and C_{2s} are the lithium ion concentration at the interface of the active material and electrolyte, respectively, C_{max} is the maximum concentration of lithium inside the solid matrix, and *U* is the open circuit potential which is a function of C_{1s}.

3.4.3 Governing equations in microscale and bridging

The conservation of mass inside the microscale is governed by Fick's mass transfer equation:

$$\frac{\partial c_1}{\partial t} = \nabla.(D_1 \nabla c_1) \quad (3\text{-}10)$$

Where, c_1 is the concentration of lithium-ion inside the microstructure, D_1 is the solid state diffusivity of LFP, and ∇ operator applies on the spatial coordinate in the 3D microscale domain. Boundary condition for the **eq. (3-10)** is expressed as:

$$j_n = -D_1 \nabla c_1.n \quad \text{at the interface of the solid matrix and electrolyte} \quad (3\text{-}11)$$

Where, n is the unit vector normal to the boundary interface and j_n is the pore-wall flux imported from macroscale. As shown in **Fig. 3-2**, bridging between two scales is a circular or two way coupling of state variables in real time (concurrent coupling). **Fig. 3-2** shows the multiscale framework along with the time dependent solution algorithm in counter clock wise direction. The marching in time starts by calculating pore-wall flux, j_n from macroscale initial values, shown by red bubble in **Fig. 3-2**. The calculated pore-wall flux, j_n then is used as the boundary condition **eq. (3-11)** for **eq.(3-10)** in microscale; by this lithium-ion concentration, c_1, is updated inside the whole microstructure using **eq. (3-11)** specially this includes updating electrode/electrolyte interface, C_{1s}. The updated C_{1s} would be used to update exchange current density, i_0 and next pore-solid lithium flux j_n. To update the flux, we assume that the electric potential and electrolyte concentration at the interface does not change between the two scales. The updated pore-solid lithium flux then is mapped from microscale to macroscale and next will be used to update other state variables through macroscale governing equations. This loop continues until the stop operation condition of the cell is satisfied.

The only remaining issue to complete the model development is determining solid state diffusivity of LFP, D_{LFP}, where special care needs to be taken. In modeling LIBs, all chemistries share a common modeling framework that involves transport of charge across both the electronic and ionic phases in an electrode, transport of mass in the ionic phase, reaction at the electrode/electrolyte interface, and transport of Li ions in the solid particles [32]. The unique features of each chemistry are then accounted for by changing the parameters

that describe these processes e.g. thermodynamic potential and diffusion coefficient appropriately. However, the LFP electrode differs from these systems in that it undergoes a phase change with the lithiated and unlithiated forms having distinct phases, as evidenced from X-ray diffraction patterns of the material at various stages of lithiation [104]. The phase change of LFP first was incorporated into P2D model using the shrinking core concept by Srinavasan *et al.* [32]. The core-shell model considers the existence of a core of one phase covered with a shell of the second phase and transport of lithium ions in the shell move the boundary between two phases. The validity of the Core-Shell model has been controversial [34,105,106] since it has shown to be incompatible with experimental observation [107]. To account for phase change, here we have used the variable solid-state diffusivity model [33,34,106] which model LFP phase change by a thermodynamic factor γ as:

$$D_1 = D_{LFP}\gamma \tag{3-12}$$

γ can be calculated based on the open circuit potential U, and state of charge of the electrode, y, using:

$$\gamma = -\frac{F}{RT}y(1-y)\frac{\partial U}{\partial y} \tag{3-13}$$

Table 3-3. List of model parameters.

Parameter	Description	Value
A	Area of the electrode	1.13 cm^2
l_{pos}	Positive electrode thickness	50 μm
l_{sep}	Separator thickness	52 μm
ε_{pos}	Porosity of positive electrode	0.4
ε_{sep}	Porosity of separator	1
D_{LFP}	Solid state binary diffusion coefficient of LFP	7×10^{-18} m^2 s^{-1}
σ	Electrical conductivity of positive electrode	0.03 S/m
k_0	Reaction rate constant in positive electrode	2.5×10^{-13} $mol\ m^{-2}s^{-1}(mol\ m^{-3})^{-1.5}$
α_a	Anodic transfer coefficient	0.5
α_c	Cathodic transfer coefficient	0.5
i_f	Exchange current density of lithium foil	19 A m^{-2}
c_{ini}	Initial salt concentration in the electrolyte	1000 mol m^{-3}
c_{max}	Maximum Lithium concentration in the LFP particles	22800 mol m^{-3}
D_{LiPF_6}	Salt diffusivity of electrolyte	3×10^{-10} m^2 s^{-1}
t_+^0	Lithium ion transference number	0.343
T	Cell Temperature	298 K

U	Open circuit potential of LFP	$\mathrm{U}_{\mathrm{c}/50}$ $= 3.382 + 0.00470\,\mathrm{y}$ $+ 1.627\exp(-81.163\,\mathrm{y}^{1.0138})$ $+ 7.6445$ $\times 10^{-8}\exp(25.36\,\mathrm{y}^{2.469})$ $- 8.4410$ $\times 10^{-8}\exp(25.262\,\mathrm{y}^{2.478})$

3.5 Results and Discussion

As discussed earlier, in the P2D model it is assumed that the porous electrode consists of isotropic, homogeneous, monodispersed spherical particles [66]. These assumptions are not valid for real battery electrodes where the electrode microstructure is inhomogeneous, non-isotropic with 3D pores and constructed from different size and shape particles. In this study, consideration of the 3D reconstructed real electrode microstructure creates the opportunity to remove the P2D assumptions to reach more accurate and more detailed results related to the electrode microstructure.

The galvanostatic discharge at various rates for an LFP half-cell with the model parameters listed in **Table 3-3** is obtained from the multiscale model and shown in **Fig. 3-3a**. It is noted that the multiscale model takes the real electrode structure into account. The design adjustable parameters including the solid phase diffusion coefficient, D_{LFP}, and solid matrix conductivity, σ, are determined based on the method described in ref. [32] and compared with

the obtained experimental data. In addition, to compare the multiscale model with Newman P2D model, the half-cell is also simulated based on the P2D model and results are shown in **Fig. 3-3b**. In P2D model, the average spherical particle size was chosen to be 37 nm based on the single particle distribution obtained by SEM (see **Fig. 3-1c**) [33]. The specific surface area of electrode/electrolyte in the P2D model is calculated for spherical particles with a radius of 37 nm and the effective transport properties including $D_{eff}, k_{eff}, \sigma_{eff}$, are calculated using Bruggeman relation with the coefficient of 1.5 [30].

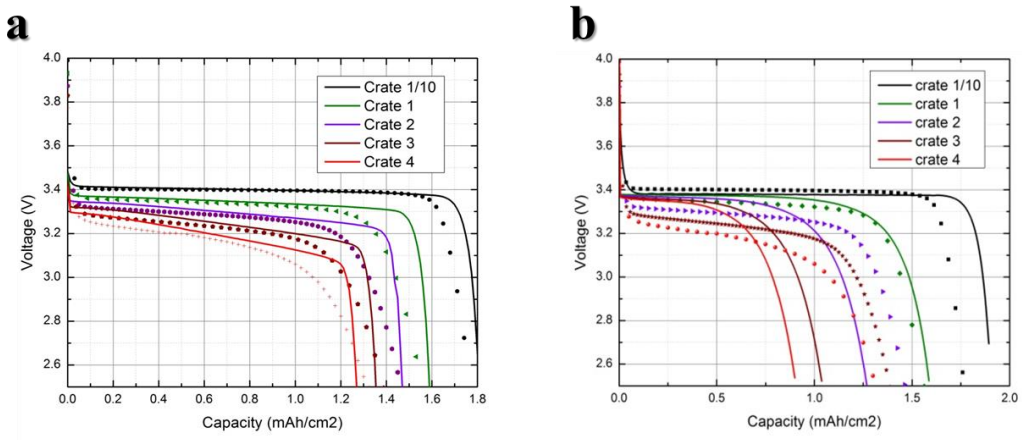

Figure 3-3. Comparison of the modeling (line) and experimental (dots) results for a LFP electrode half-cell at different discharge rates (a) multiscale model (b) Newman P2D model.

As shown in **Fig. 3-3b**, the P2D model over predicts the capacity at discharge rates lower than 1 and under predicts the capacity for higher discharge rates. Other researchers have also achieved the same results for the Newman P2D model [32–34]. In the modeling work using P2D model, the normal remedy to address this issue is using two [32] or four [33,34] different particle sizes to mimic the real electrode microstructure. On the other hand, the multiscale model could also predict the discharge curves at different rates without further

assumption using reconstructed electrode morphology. The reconstructed geometry provides higher surface area for the lithium to intercalate compared to the spherical particle geometry with average size in the P2D. Moreover, the multiscale model does not use the Bruggeman relation to calculate the effective transport properties.

Even though P2D model has proven successful to predict the performance, it fails to predict the degradation and failure. The main advantage using tomographic data in the current work is to visualize the heterogeneities inside the electrode microstructure contributing to electrode failure and degradation. The approach used in this study can provide valuable insight into the spatial distribution of electrochemical properties inside the electrode structure. For the LFP half-cell, during discharge at 1C, the lithium concentration, current density, open circuit potential (OCP), overpotentials, and intercalation reaction rate are determined from the multiscale modeling. The lithium concentration in the electrode microstructure along the electrode thickness direction at discharge rate of unity for various states of charges (SOCs) is shown in **Fig. 3-4**. Here, SOC is defined as the ratio of local lithium concentration to its maximum possible concentration.

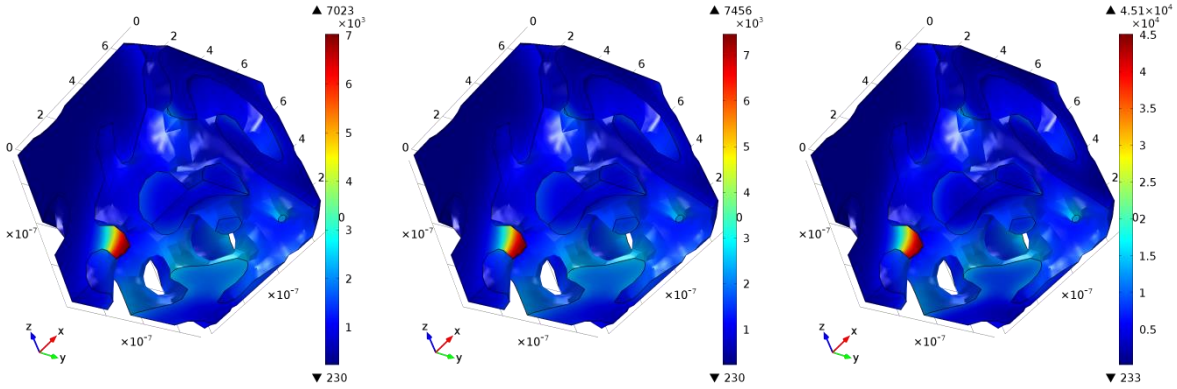

SOC=0.95

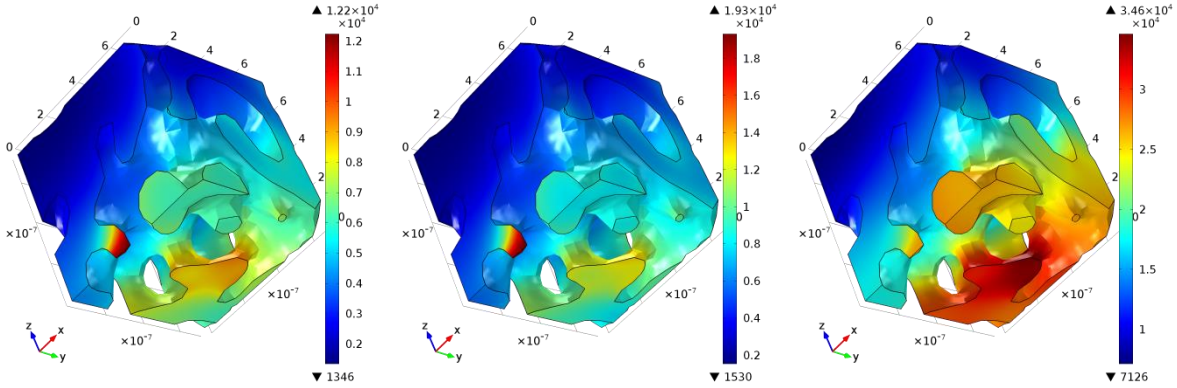

SOC=0.5

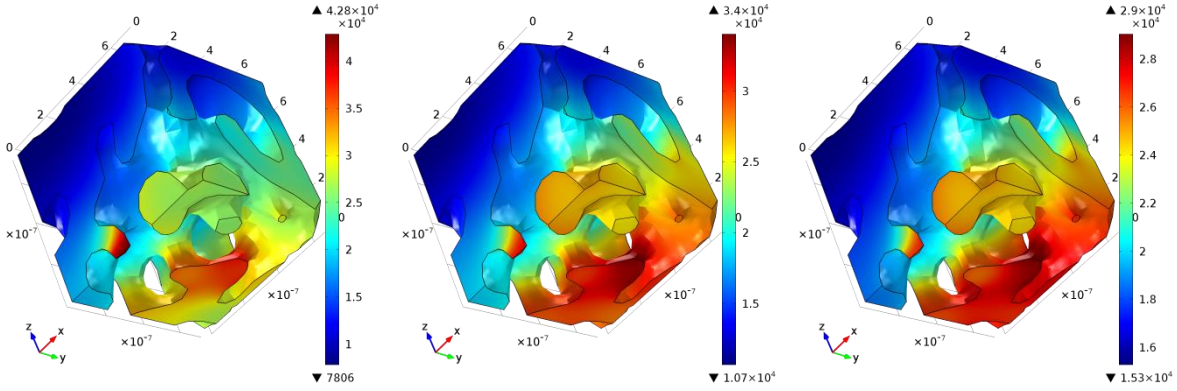

Separator ***End of Discharge*** ***Current Collector***

$x = l_{pos}/10$ $x = l_{pos}/2$ $x = l_{pos}$

Figure 3-4. Distribution of lithium concentration (mol m^{-3}) inside the electrode microstructure during discharge at C-rate=1 for different SOCs (3D electrode microstructure represents geometry in microscale and 1D x-coordinate describe geometry in macroscale along the electrode thickness direction).

The average lithium ion concentration increases from the separator toward the current collector. Moreover, lithium ion concentration in microstructure is much higher in the region with smaller cross section area perpendicular to lithium intercalation pathway. At SOC=0.5, the maximum lithium ion concentration is $4.51 \times 10^4\ mol.m^{-3}$ which is in the location of one of those sharp regions close to the current collector (cal. around 10 times compared to average lithium concentration in the RVE). Moreover, **Fig. 3-4** shows that sharp region at SOC=0.95, have higher concentration than the maximum concentration at the end of discharge (4.51×10^4 compared to 2.9×10^4) . The last feature that can be found from the concentration distribution is that the maximum concentration occurs in different locations across the electrode thickness at different times. The maximum concentration takes place in the cathode current collector location at SOC=0.95 and 0.5, whereas, it occurs in the location close to the separator at the end of discharge.

These unpredictable behavior confirms the inherent non-homogenous microstructure of LIB and could not be detected using homogenized methods. This behavior could be described better by comparing the lithium ion concentration histogram as shown in **Fig. 3-5**. The distribution range of lithium concentration becomes wider from separator to current collector for SOC=0.95 and 0.5. This would result in the more inhomogeneity in concentration for the

particles closer to current collector. However, at the end of discharge the condition is reversed and the inhomogeneity shifts toward the separator.

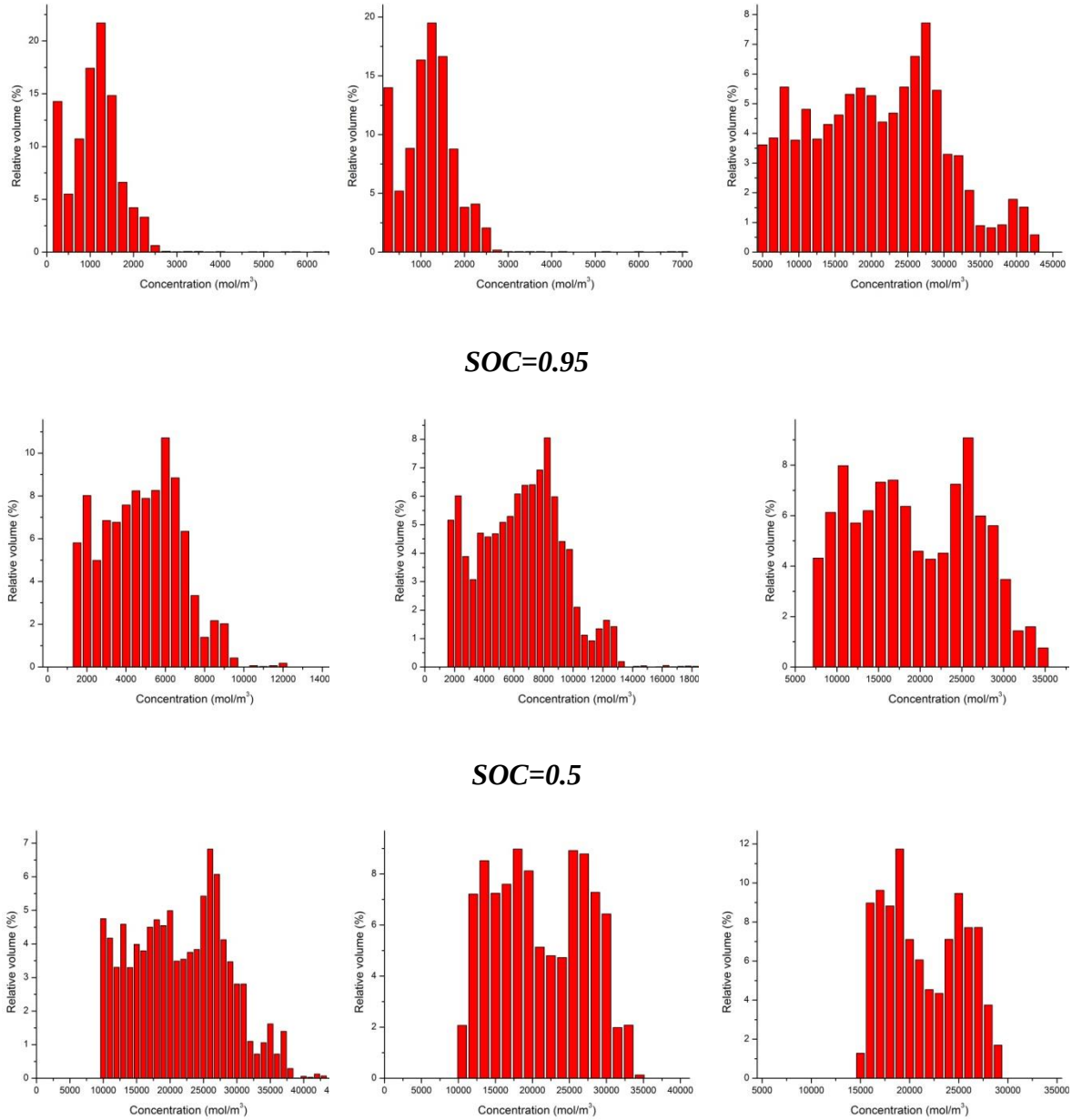

Figure 3-5. Histograms of the lithium ion concentration inside microstructure using multiscale model at C-rate=1.

To emphasize the model capability to capture inhomogeneity, lithium ion concentration result using P2D is also shown in **Fig. 3-6** for comparison. The wider range of lithium concentration using multiscale model is evident comparing two **Figs. 3-5** and **3-6**. In addition, lithium concentration distribution using P2D model shows a certain trend because the properties vary in direction of electrode thickness. Nevertheless, the property distribution based on the real microstructure properties show no clear trend due to inherent inhomogeneity of microstructures.

Fig. 3-7 illustrates the overpotential distribution on the electrode solid/electrolyte interface. The overpotential is calculated using **eq. 3-8**, and is a function of OCV, electric potential in the solid, ϕ_1, and electric potential in electrolyte, ϕ_2. OCV is obtained by microscale simulation results from the lithium concentration on the solid/electrolyte interface. The OCP is a function of the SOC on the electrode solid/electrolyte interface based on the experimental data obtained during the half-cell discharge at C/50 (shown in **Table 3-3**). Inhomogeneous distribution of the OCP is due to different lithium concentrations and material utilization during discharge. On the other hand, electric and electronic potentials are achieved through macroscale results. Therefore, the overpotential is a property that requires to be calculated using results from the multiscale: microscale and macroscale. On the solid/electrolyte interface at a certain point along the thickness direction, the overpotential variations is primary due to OCP changes. However, among different location along thickness direction is due to different contributions of OCP and electric potential in the solid and electrolyte.

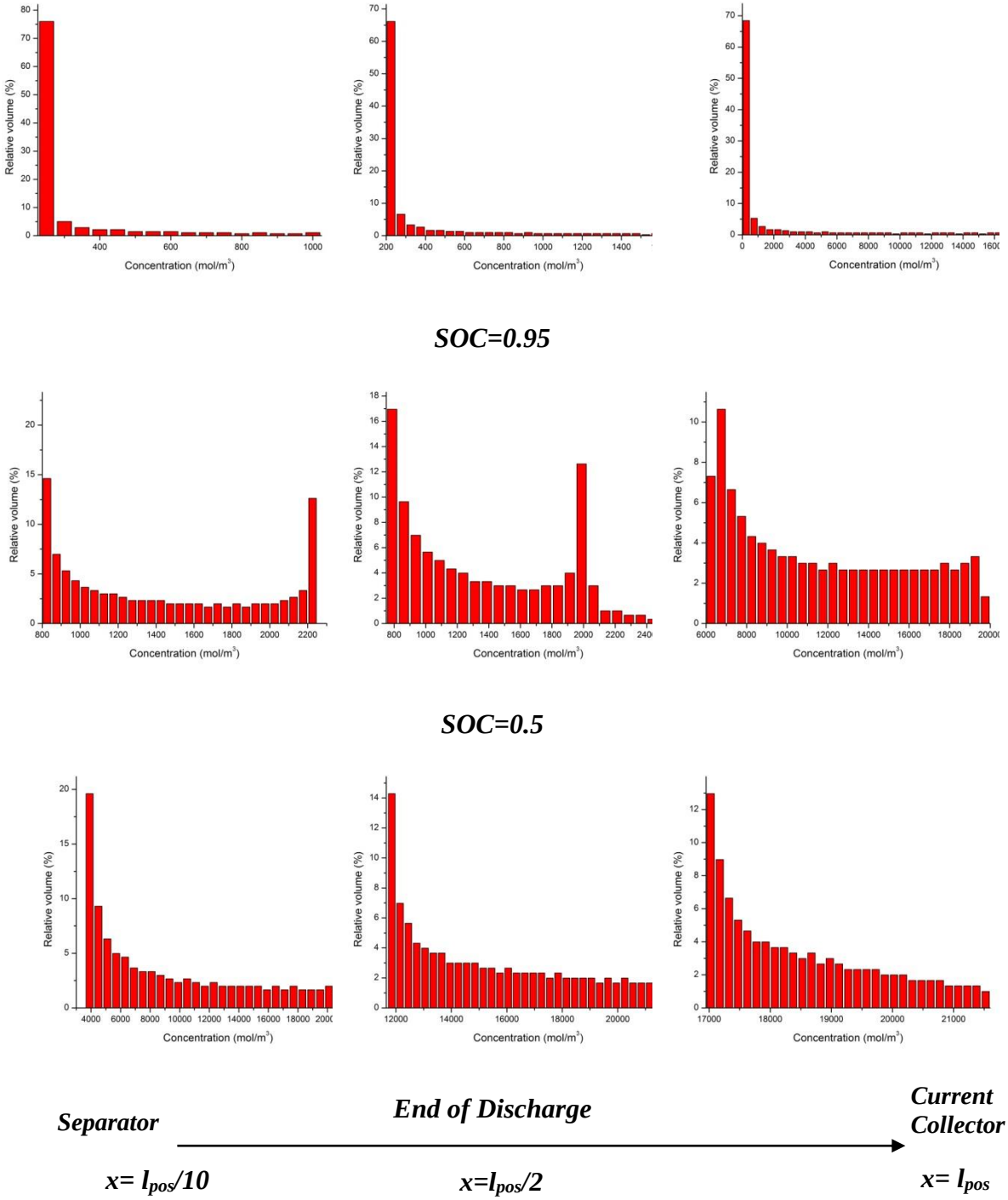

Figure 3-6. Histogram of the lithium ion concentration using P2D model inside spherical particles with radius of 37 nm at C-rate=1.

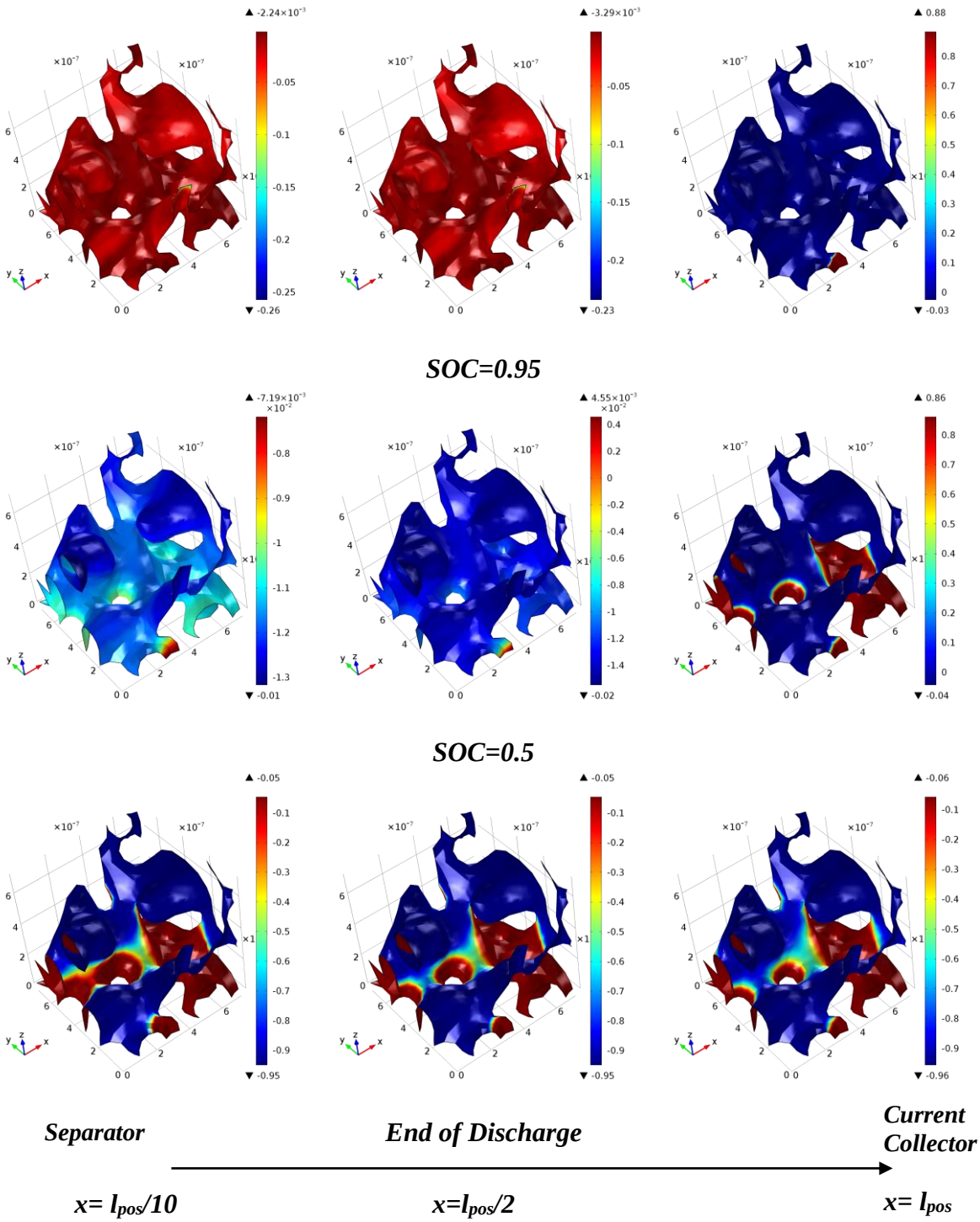

Figure 3-7. Distribution of the overpotential (unit:V) on the solid/electrolyte interface during discharge at C-rate=1 for different SOCs.

To compare the simulation results at different rates, discharge process at C-rate=4 is presented in **Fig. 3-8**. Lithium ion concentration in the electrode microstructure at the end of discharge for C-rate=4 is shown in the first row in **Fig. 3-8**. Simulation results show higher inhomogenity inside microstructure at C-rate=4 (1st row in **Fig. 3-8**) compared to the C-rate=1 (3rd row of **Fig. 3-4**). The inhomogenity could be better scrutinized by comparing the range of lithium concentration at different rates.

Table 3-4. Lithium concentration range in the microstructure along the electrode thickness direction at different rates (time: end of discharge, unit: mol/m^3).

C-rate	$l_{pos}/10$	$l_{pos}/2$	l_{pos}
1	3.50×10^4	2.33×10^4	1.37×10^4
4	1.05×10^5	7.40×10^4	3.91×10^4

Table 3-4 summarizes those ranges which clearly confirms the wider range of concentration at higher rate due to effect of inhomogeneities. In addition, OCP and overpotential interfacial properties at the solid/electrolyte interface along the electrode thickness direction are also shown in 2nd and 3rd row of **Fig. 3-8**, respectively. **Fig. 3-8** shows that the interfacial properties are also distributed in a wider range at C-rate=4 compared to C-rate=1.

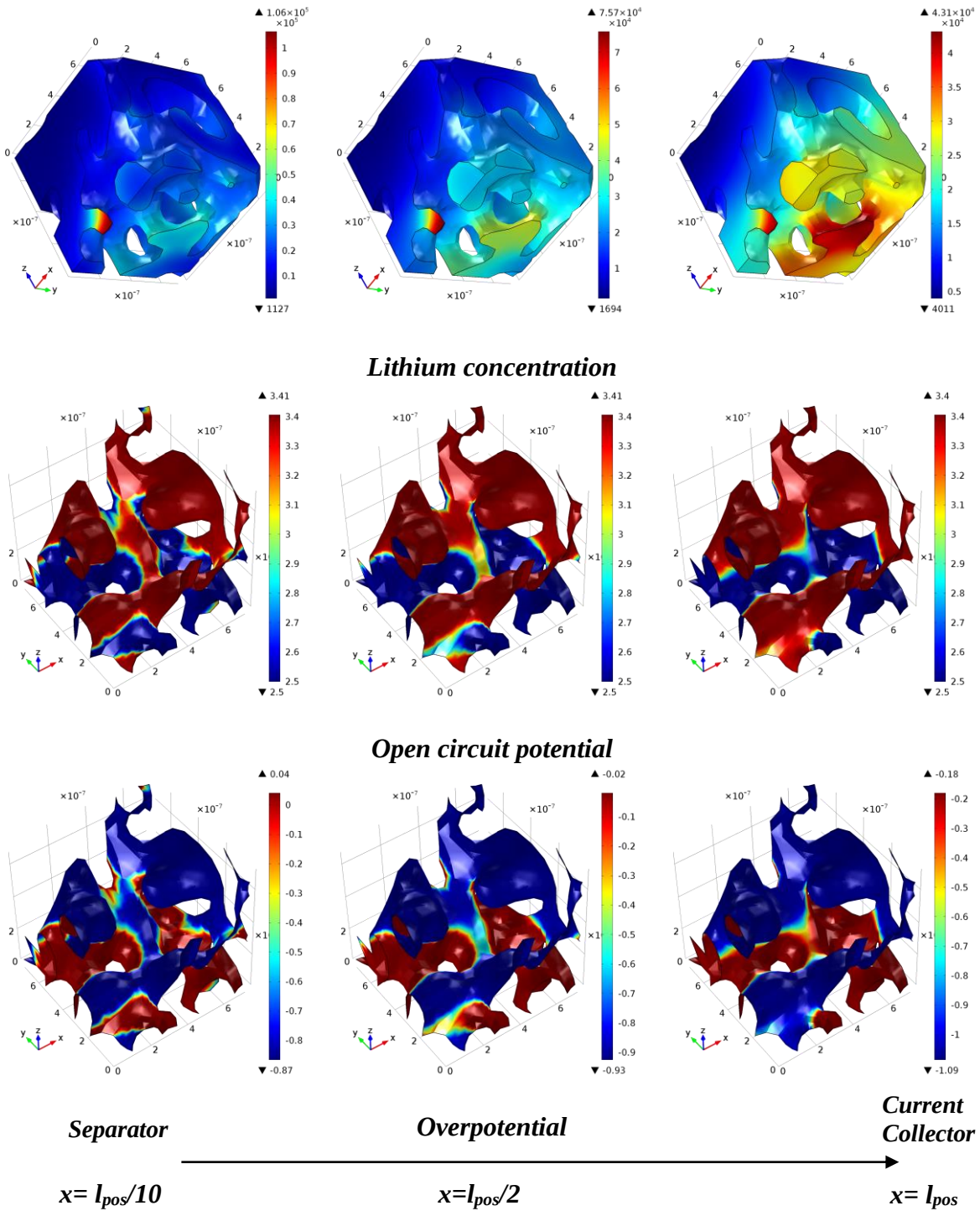

Figure 3-8. Distribution of lithium concentration (mol m^{-3}) and Interfacial properties along the electrode thickness direction at the end of discharge for C-rate=4.

3.6 Conclusions

In this chapter, we have successfully established an imaged-based multiscale model to study the real microstructure of electrodes of lithium ion batteries. The model is based on the real 3D microstructure data, while taking advantage of the traditional homogenous 1D model in macroscale to characterize discharge/charge performance. In macroscale, the model is modified through dropping Bruggeman relation and replacing it by real tortousity of the electrode porous structure. In addition, the interfacial surface area is determined based on the nano-XCT data removing the typical relation assuming spherical particles. The coupling between micro and macro scales are performed in real time unlike using common surrogate based models for microscale. The simulation results could predict the experimental discharge voltage of LFP cathodes at different rates. The simulation showed that the lithium ion concentration in the electrode active material structure is much higher in the region with smaller cross-section area perpendicular to the lithium intercalation pathway. Such low area regions would intercalate ca. 10 times higher than the area with an average concentration. The approach used in this study can provide valuable insight into the spatial distribution of lithium ions inside the microstructure of LIB electrodes. The inhomogenous microstructure of LFP causes a wide range of physical and electrochemical properties compared to the homogenous model.

4. Representative Volume Element Model of Lithium-ion Battery Electrodes Based on synchrotron X-ray Nano-tomography

This chapter is reprinted in adopted form with permission from Journal of applied electrochemistry:

Kashkooli, A. G.; Amirfazli, A.; Farhad, S.; Un Lee, D.; Felicelli, S.; Woong Park, H.; Feng, K.; De Andrade, V.; Chen, Z. Representative volume element model of lithium-ion battery electrodes based on X-ray nano-tomography Journal of Applied Electrochemistry, 2017, 47-281.

4.1 Introduction

As highlighted in previous chapter, various computer models have been developed in the past to predict the performance based on different electrode designs and operating conditions [102,103,108]. However, the results of these models demonstrated limited accuracy due to the over-simplification of electrode structures. Physics based LIB models based on their description of electrode structures, are categorized into four distinct groups: 1) models that describe electrodes as homogenous single-sized spherical particles [12,78,109]; 2) models that describe electrodes comprising of multi-sized spherical particles [33,34,110]; 3) models that deploy sophisticated mathematical methods to simulate electrode structures [89,111,112]; 4) models that reconstruct real electrode microstructures using two imaging methods of Focused ion beam-Scanning electron microscopy (FIB-SEM) and X-ray computed tomography (XCT). The computational costs of groups 3) and 4) are significantly higher due to their complexity

compared to those of 1) and 2). However, the advantage of them over those of 1) and 2) is much detailed information that can be obtained such as heterogeneous distributions of lithium-ions inside electrode microstructures during both lithiation (charge) and de-lithiation (discharge) processes, which is very useful when simulating the whole battery-cell or battery-pack.

The aforementioned complexities associated with 3D modelling of electrode microstructures can be reduced without sacrificing accuracy by considering smaller sizes of electrode volume called Representative Volume (RVE) [113–115]. The RVE provides a way to compute a smaller domain while maintaining the heterogeneous microstructures of the electrode, which is one of the determining factors that often dictate the overall cell performance. This essentially allows for improved computational efficiency by reasonably reducing computational costs associated with modeling complex 3D images to still accurately describe electrode behaviors. In fact, the RVE method is widely employed to model the mechanical characteristics of composite materials [116–118], but has only gained interest from the energy field recently. For example, RVE has been employed to investigate the microstructures and effective transport properties in solid oxide fuel cells [119–122]. Additionally, Shearing *et al.* [53] have utilized the RVE concept for studying graphite electrodes by reconstructing the real 3D morphology using XCT. The authors have analyzed the electrode porosity and solid matrix volume specific surface for sub-volume of the sample to achieve minimum RVE size.

In the chapter 3, we developed a multi-scale model consisting of both micro and macro scale models to investigate the discharge behavior of $LiFePO_4$ (LFP) electrodes [10]. For the

microscale, we reconstructed the 3D electrode morphology using nano-XCT, while for macroscale, the galvanostatic discharge behavior was simulated by employing the homogenization theory and Newman psedudo-2D model [30,31]. The multi-scale model, which included the real 3D morphology of the electrode, was an improvement over the Newman pseudo-2D model, whereas the present RVE model is an advancement over the single-particle model [123,124], which allows the formation of a computationally efficient framework for including reconstructed three-dimensional morphology of the electrode. The RVE model is developed with the notion of replacing the single-particle geometry with a RVE obtained from XCT imaging. In addition, the RVE model can be considered as a simplification of our previously reported multi-scale model where for RVE model, the local lithium-ion concentrations inside the electrolyte is neglected and a solution resistance term is used instead to account for the electrolyte resistance. Moreover, the electric potential variations inside the solid matrix is also be neglected, which makes the model applicable for thin electrodes subjected to low to medium current rates. This model accounts for the diffusion of lithium-ions inside and between the active materials. The 3D morphology of the electrode is reconstructed using a Simpleware 7.0 and COMSOL Multiphysics® 5.0 is employed to simulate the LIB performance.

4.2 Nano-XCT imaging

LFP electrode samples have been recovered from a LFP/graphite pouch cell for nano-XCT imaging. The cell was opened in a sealed glove box filled with argon where the oxygen and water level were kept below 0.5 ppm. The electrode aluminum foil was delaminated by

soaking the sample in a 6.0 M KOH solution since aluminum interferes with X-ray imaging. The acquisition of a tomogram was conducted using Transmission X-ray Microscope (TXM), the new nano-tomography instrument of sector 32-ID-C at Advanced Photon Source, Argonne National Laboratory [59]. The radiographs were acquired in the absorption mode using an 8 keV monochromatic beam. The tomographic images were obtained by rotating the sample 180° using a step scan increment of 0.5° and the exposure time of 1 second at each increment. The X-ray objective lens used to magnify radiographs was a 60 nm outermost zone width Fresnel zone plate, providing a spatial resolution of 60 nm. The 3D reconstruction was performed with Tomopy, an open source platform for the synchrotron tomographic data analysis [125,126]. The reconstructed volume represents voxel of 58 nm^3 after binning. Subsequently, ScanIP 7.0 was used to perform segmentation of each individual reconstructed slice to extract the final 3D morphology of the solid matrix.

Fig. 4-1 shows the morphology of the LFP electrode consisting of nano-particles revealed by SEM (**Fig. 4-1a**), and the reconstructed 3D microstructure obtained using nano-XCT imaging (**Fig. 4-1b**). Because of the low X-ray absorption of the polyvinylidene fluoride (PVDF) binder and conductive carbon, they are indistinguishable from the pore phase by single run of imaging. As such, the polymer binder and carbon additives are not distinguished from the active material in the present study. Alternatively, one can assume that relatively much lower percentages of binding and carbon additives are randomly distributed among the active material [10,66,99] and form an integrated solid matrix. To simulate this, a close image processing algorithm in ScanIP was employed on the active material region to guarantee the connectivity of neighbor particles. This also provides the possibility of lithium-ion diffusion

between two neighboring particles, unlike in Newman type models where the lithium-ions are imprisoned inside the particles. Although not all of active particles may be in perfect contact, we have assumed that very particle is in perfect contact which eliminates any diffusion intra-resistance. On the other hand, the average particle size of LFP is 37 nm which is below the resolution of the XCT (60 nm). Therefore, it is impossible to capture individual particles, and rather images cluster of LFP particles, which justifies our assumption of fusion of neighboring particles. This means that the 3D solid matrix shown in **Fig. 4-1b** consists of LFP, PVDF, and conductive carbon. More detailed description of segmentation and reconstruction of the 3D microstructure can be found in our previous publication [10].

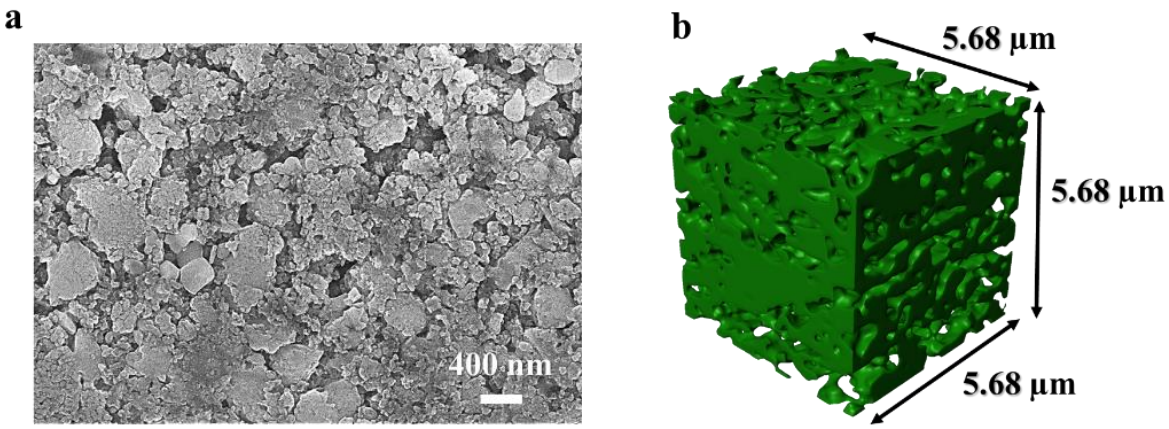

Figure 4-1. (a) Typical morphology of the LFP electrode revealed by SEM, and (b) the reconstructed 3D electrode microstructure obtained by nano-XCT imaging

4.3 Modeling and Computer Simulation

4.3.1 RVE selection

Assuming that the LIB electrodes are a periodic material, the RVE of a LIB electrode is a subdivision volume over which a measured property can be considered as a representative value for the whole electrode. In our model, the electrode properties of interest for the determination of an appropriate RVE size are the electrode porosity and volume specific surface area which is the ratio of solid/electrolyte surface area to electrode volume. **Table 4-1** shows sample volume specific surface area and porosity of a cubic RVE subdivision of different sizes. The domain porosity is around 0.4. For a RVE size of 850 nm and larger, the porosity of the subdivisions lies within 2 % of the whole sample porosity. Moreover, the electrode volume specific surface area is 3.3 (1/μm), thereby remaining within 7% of the domain volume specific surface area for volumes sizes of 850 nm and larger. Therefore, the smallest appropriate RVE of the electrode is selected as 850 nm size. This calculation is based on the selection of subdivision volumes from one corner of electrode sample. To reduce the error associated with the selection of specific sample region in the electrode position, in the present study we have selected a volume with side length of 3000 nm (see **Fig. 4-2**) as electrode RVE and model geometry although we could have chosen the smallest RVE size (i.e. 850 nm).

Table 4-1. The electrode porosity and the solid matrix volume specific surface area represented in a RVE with different sizes

Cube size (nm)	Porosity, ε	Volume specific surface area, a $(\mu m)^{-1}$
283	0.54	4.85
425	0.35	5.35
849	0.38	3.71
1132	0.42	3.79
1698	0.39	3.75
2264	0.42	3.63
2830	0.42	3.46
3396	0.43	3.27
3962	0.47	3.28
4528	0.43	3.27
5094	0.41	3.34
5660	0.41	3.32

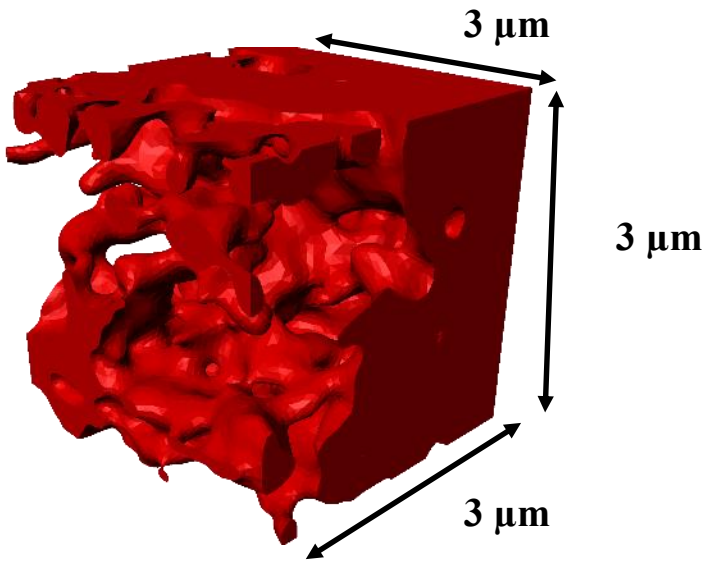

Figure 4-2. The 3D morphology of the electrode microstructure of the RVE model selected from the reconstructed solid matrix by nano-XCT

4.3.2 Governing equations

The governing equation used in this study are the conservation of mass and intercalation kinetics. As mentioned previously, the variations of lithium-ion concentration and electric potential inside the electrolyte are neglected and electrolyte polarization is included by a lumped constant electrolyte resistance parameter. In addition, the electric potential gradient in the solid phase of the electrodes is neglected. In the RVE model, the diffusion inside the solid matrix is modeled by Fick's mass transport law as [10,66]:

$$\frac{\partial c_1}{\partial t} = \nabla.(D_1 \nabla c_1) \tag{4-1}$$

Where, c_1 is the concentration of lithium-ion in the RVE, D_1 is the lithium diffusivity in the solid matrix, and ∇ operates on the spatial coordinates. To distinguish different regions in the

porous electrode, subscripts 1 and 2 are utilized to represent the solid matrix and electrolyte, respectively. The boundary condition for **eq. (4-1)** at the solid/electrolyte interface is [10,66]:

$$j_n = -D_1 \nabla c_{1,s}.n \tag{4-2}$$

Where, j_n is the normal component of lithium-ion mass transfer flux at the solid/electrolyte interface caused by the electrochemical reaction, *s* refers to the solid/electrolyte boundary, and *n* is the boundary interface normal unit vector, pointing toward the electrolyte. A symmetric boundary condition is applied on all other surfaces. j_n at the solid/electrolyte boundary is depended on applied current density as:

$$j_n = \frac{i_{loc}}{F} = \frac{i_{app}}{F(1-\varepsilon)aL} \tag{4-3}$$

where, i_{loc} is local current density at the interface, i_{app} is the applied current density on the cell level, F is Faraday's constant, ε is the electrode porosity, *a* is the specific surface area of the interface per volume of the solid phase, and *L* is the electrode thickness. The local state of charge (SOC) for the solid matrix can be estimated by:

$$SOC = 1 - \frac{c_1}{c_{max}} \tag{4-4}$$

Where, c_{max} is the maximum concentration of lithium inside the active material. Rate of intercalation reaction is obtained using Butler-Volmer electrochemical kinetics relation [127]:

$$j_n = \frac{i_{loc}}{F} = \frac{i_0}{F}\left(exp\left(\frac{\alpha F}{RT}(\phi_1 - U)\right) - exp\left(-\frac{(1-\alpha)F}{RT}(\phi_1 - U)\right)\right) \tag{4-5}$$

where, α is charge transfer coefficient, R is the universal gas constant, T is temperature, ϕ_1 is the electric potential in solid matrix, and U is the open circuit potential and i_0 is the exchange current density, which is defined as [127]:

$$i_0 = Fk_0(c_2)^{\alpha}\left(c_{max} - c_{1,s}\right)^{\alpha}(c_{1,s})^{\alpha} \tag{4-6}$$

Where, k_0 is rate constant of the reaction, c_2 is concentration of lithium-ion in electrolyte which we considered it as a constant in this study. To enhance model numerical efficiency, the Butler-Volmer relation can be expressed using inverse hyperbolic function which results in following relation for calculating ϕ_1:

$$\phi_1 = U + \frac{RT}{\alpha F} asinh\left(\frac{i_{loc}}{2i_0}\right) \tag{4-7}$$

By neglecting the solid phase potential gradient, the electrode potential, V, is obtained by averaging the ϕ_1 on the solid/electrolyte interface as:

$$V = \frac{\int_s \phi_1 \, ds}{\int_s \, ds} \tag{4-8}$$

At the lithium counter electrode, $V = 0$. Therefore, the half-cell voltage can be determined by:

$$E = V - i_{app}R_2 \tag{4-9}$$

Where, R_2 is the electrolyte resistance parameter that express the potential drop inside the electrolyte between positive and negative electrodes. Here R_2 is an adjustable parameter that is set by comparing simulation results with experimental data [123,128]. At each time step four variables, c_1, i_0, ϕ_1, E, are updating through equations 1, 6, 7, 9 and U through the last row in **Table 4-2**. **Fig. 4-2** illustrates the modeling solution algorithm.

The final issue to complete modeling development is to specify LFP solid state diffusivity, (D_{LFP}) where its phase change needs to be considered. In modeling LIBs electrodes, all the intercalation based chemistry share a common modeling platform to simulate electrode performance; The unique features of each chemistry is included by varying physical and electrochemical properties. However, LFP deviates from this usual approach since it experiences phase change with the formation of two separate lithiated and unlithiated phases, as proved by X-ray diffraction [104]. Srinavasan *et al.* first incorporated the phase change of LFP using the shrinking core concept [32]. The core-shell model assumes that in a spherical particle, two lithiated and unlithiated phases co-exist where one phase is enclosed with the other phase in a structure similar to a core-shell; As lithium-ions transfer inside the shell, the boundary between two phases moves in the radial direction. The accuracy of core-Shell model has been questioned [34,105,106] and also been shown to be incompatible with experimental observations [107]. In the present study, to include LFP phase change, we employed the variable solid-state diffusivity model [33,34,105] wherein phase change is modeled by using a thermodynamic factor γ as:

$$D_1 = D_{LFP}\gamma \tag{4-10}$$

γ is calculated based on the open circuit potential U, and SOC using:

$$\gamma = \frac{F}{RT} SOC(1 - SOC) \frac{\partial U}{\partial SOC} \tag{4-11}$$

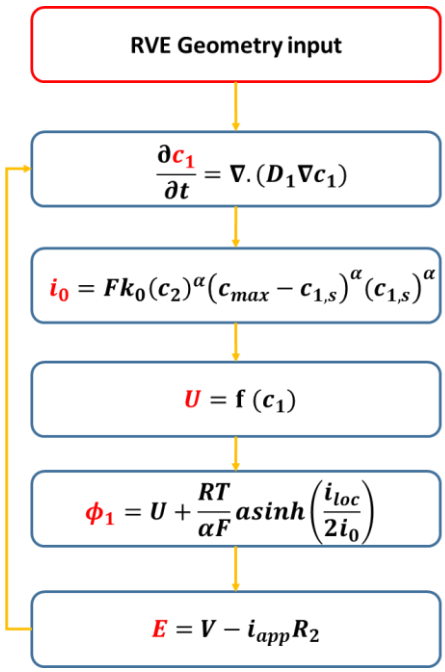

Figure 4-3. RVE model algorithm wherein the updating state variable is shown in red.

4.4 Experimental

In order to validate the model, coin cells were made using the LFP electrode from the same commercial pouch cell. Commercial cathodes have slurry coating on two sides of current collector, so the coating on a side was delaminated by a cotton wipe immersed in 1-methyl-2 pyrolidinone (NMP). The electrode was then punched in a circular area of 1.13 cm^2 and assembled into a coin half-cell (LIR2032-type) inside the glove box. The electrode coin half-cells were made using lithium metal as the counter electrode and (Celgard 2500) as a separator. A solution of 1.0 M lithium hexafluorophosphate ($LiPF_6$) salt in the 1:1 (v/v) ethylene carbonate (EC): diethyl carbonate (DEC) was utilized as electrolyte. Coin cells were tested on the (Neware CT-3008-5V10 mA) battery cycler. All coin cells are first cycled five times to gradually form the solid-electrolyte interphase (SEI) layer on the surface of the electrode. The

formation stage is performed using a constant-current–constant-voltage CCCV method at C/5. The cells are first charged on CC from 2.5 to 4.2 V and then are charged again on CV of 4.2 until the current falls below C/25 to guarantee that the electrode returns to a completely charged condition. The charging follows 30 minutes rest interval, and then cells are discharged on CC from 4.2 to 2.5 V. We obtained the open circuit potential of the half-cell by discharging a totally charged half-cell at very low current (C/50). Low current keeps cell polarizations small and provides a good approximation for the open circuit potential. The rate-capability results were obtained by galvanostatically charging/discharging the coin cells at different C-rates.

4.5 Results and Discussion

We have simulated the galvanostatic discharge process of the half-cell based on the reconstructed structure of the LFP electrode and have developed modeling platform. The material properties, operation conditions, and model parameters are shown in **Table 4-2**. The diffusion coefficient, D_{LFP} is considered as a model adjustable parameter and determined by fitting the model to experimental discharge curve corresponding to a low-rate condition [32,34]. The discharge curve at C-rate=0.1 was used as the base case to fit the model to experiment data. The value of 1.2×10^{-14} m^2/s provided the best-fit and was used for the C-rates>0.1 to predict the galvanostatic discharge. The obtained D_{LFP} is almost five orders of magnitude greater than what is commonly utilized in spherical-particle models [33,34]. This value agrees very well with recent experimental data reported in the literature, confirming extremely fast lithium-ion diffusion within LFP particles with D_{LFP} in the range of 10^{-13} to

10^{-15} m^2/s [129,130]. Based on a single-particle model, the electrode is assumed to consist of single-sized nano-scale spherical particles. However, the real electrode structure includes a range of particle sizes ranging from tens of nano-meters to micro meters. As a result, to simulate the performance, the single-particle model requires an invalid (very small) diffusion coefficient to adjust the unrealistic assumption of structure morphology. On the other hand, RVE model includes the reconstructed heterogeneous structure of the electrode obtained from XCT. The structure consists of bi-continuous network of particles cluster with various sizes and morphologies. Therefore, the diffusion coefficient obtained for RVE model is in agreement with the recent experimental measurement. For example, Munakata *et al.* [129] used a single micro-size LFP secondary particle to investigate the lithium-ion diffusion coefficient. The secondary particle was composed of primary nano-size particles. The particle was connected to a micro Pt electrode in an electrolyte solution using a micromanipulator under optical microscope visualization. Then a galvanostatic charge/discharge process was conducted to characterize electrochemical performance. The lithium-ion diffusion coefficient in the particle was found to be 2.7×10^{-13} m^2/s which is in a good agreement with 1.2×10^{-14} m^2/s in this study.

Table 4-2. List of model parameters [10]**.**

Parameter	Description	Value
A	Area of the electrode	1.13 cm^2
L	Positive electrode thickness	50 μm
ε	Porosity of positive electrode	0.4
D_{LFP}	Solid matrix diffusion coefficient	1.2×10^{-14} m^2 s^{-1}
k_0	Reaction rate constant in positive electrode	2.5×10^{-13} $mol\ m^{-2}s^{-1}(mol\ m^{-3})^{-1.5}$
α	Charge transfer coefficient	0.5
c_{ini}	Salt concentration in the electrolyte	1000 mol m^{-3}
c_{max}	Maximum Lithium concentration in the LFP particles	22800 mol m^{-3}
T	Cell Temperature	298 K
R_2	Electrolyte resistance parameter	2.7×10^{-3} $\Omega\ m^2$
U	Open circuit potential of LFP	$U = 3.382 + 0.00470\ (1 - soc) + 1.627\exp(-81.163\ (1 - soc)^{1.0138}) + 7.6445 \times 10^{-8}\exp(25.36\ (1 - soc)^{2.469}) - 8.4410 \times 10^{-8}\exp(25.262\ (1 - soc)^{2.478})$

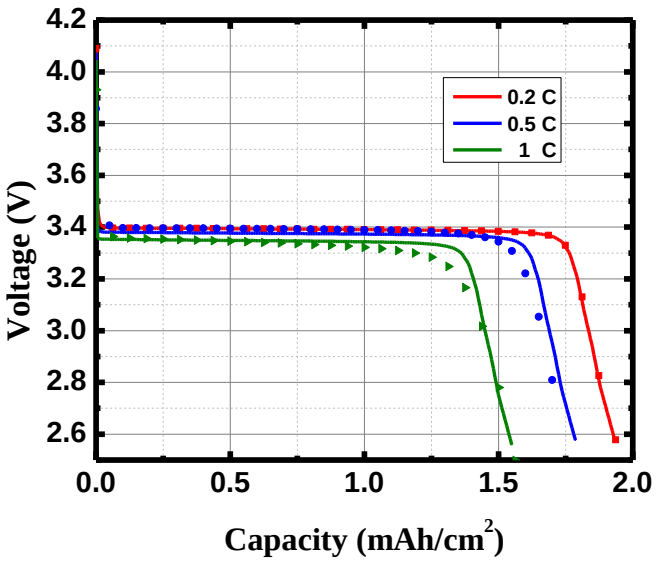

Figure 4-4. Comparison of the RVE modeling (line) and experimental (dots) results for the coin half-cell based on the LFP electrode tested at varying discharge rates.

Fig. 4-4 shows the galvanostatic discharge curves obtained at different rates based on the simulation using the RVE model. The experimental data was obtained from the coin cell performance data. The model describes the discharge behavior of LFP electrode accurately up to C-rate of 1.0. It should be noted that the main advantage of using nano-XCT to reconstruct the morphology of the electrode in the present work is the capability to capture a heterogeneous lithium-ions distribution inside the electrode solid matrix. Newman type models [31,34,78,127] which are based on isotropic, homogeneous spherical particles have proven to be successful and computationally efficient for modelling battery performance. However, the assumptions that the model makes are not reasonable for electrodes comprised of heterogeneous, non-isotropic particles with different particle shapes and sizes. On the other hand, nano-XCT based RVE modeling presented in this study uses a framework which

simulates the real electrode morphology to accurately account for the heterogeneities inside the electrode microstructure.

Fig. 4-5 shows the concentration of lithium-ion inside the electrode solid matrix obtained at different state of charges (SOCs) during galvanostatic discharge at C-rate of 1.0. As mentioned above, a symmetric boundary condition is applied on all 6 sides of the RVE and the lithium-ions can diffuse inside the RVE at the solid matrix and electrolyte interface. In addition, lithium is free to diffuse between the neighboring particles unlike the Newman type models wherein they are trapped in one-dimensional spherical particles. During galvanostatic discharge, the lithium-ion concentration gradually increases until it reaches the maximum local concentration of 22,800 mol/m^3 which corresponds to the cut-off voltage of 2.5 V. The concentration ($mol.m^{-3}$) distributions are better illustrated with cross-sectional contour plots along the direction of the electrode's thickness as demonstrated in **Fig. 4-6** (The distance between each cross section is 1 μm). **Fig. 4-6** shows that at any given SOC, the concentration of lithium-ion is relatively elevated in two regions: one with smaller cross-sectional area normal to the diffusion path of lithium, and the other with higher surface area exposed to the electrolyte. The observed non-uniform distributions of lithium-ion concentration are different from those of the spherical particle models, which commonly show a gradual increase of the concentration from the particle center to the particle surface.

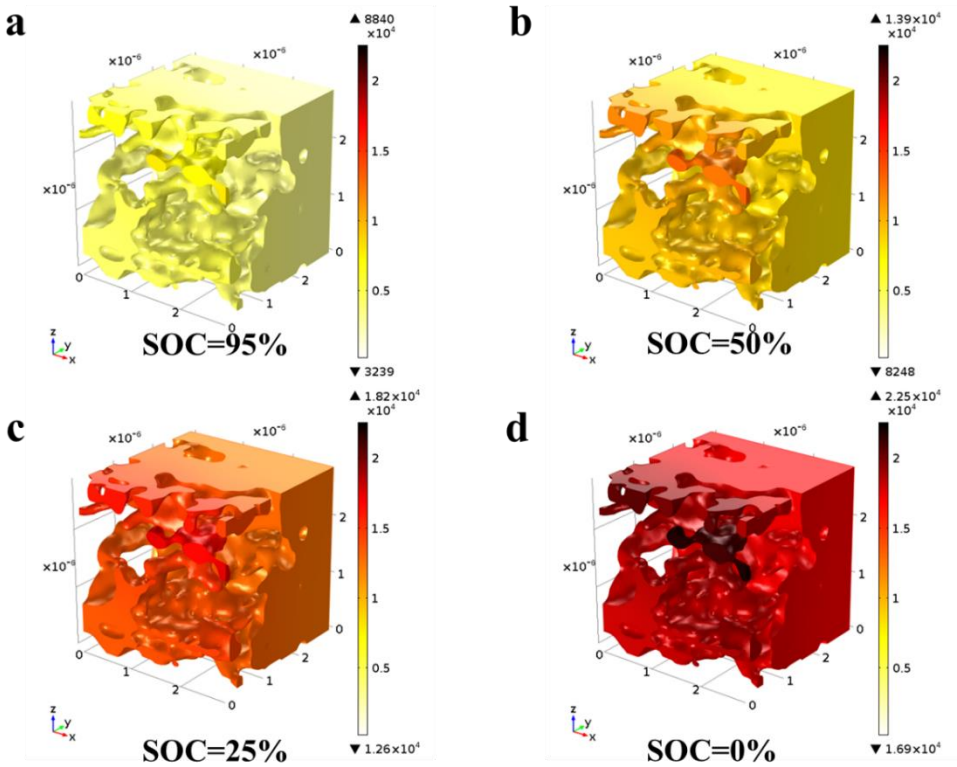

Figure 4-5. The lithium-ion concentration (mol m^{-3}) inside the electrode microstructure obtained at different SOCs during galvanostatic discharge at C-rate of 1.0.

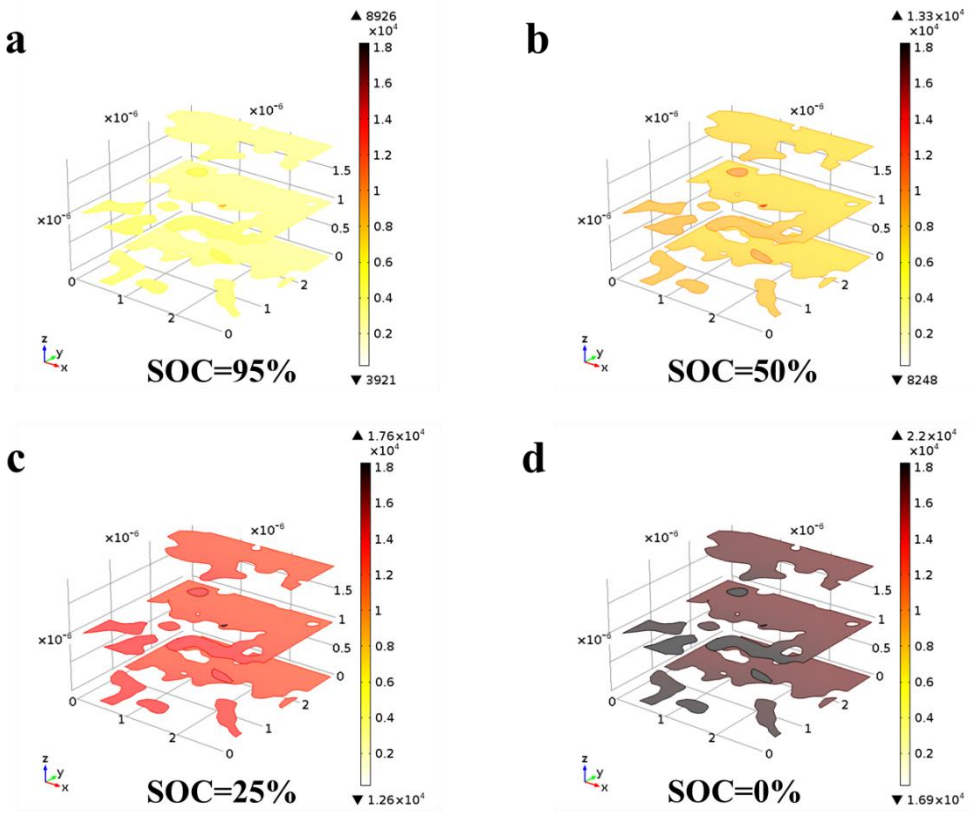

Figure 4-6. The lithium-ion concentration (mol m^{-3}) inside the electrode microstructure obtained at three different 2D projecting radiographs along the direction of the electrode's thickness during galvanostatic discharge at C-rate of 1.0.

The capability of the model to show the heterogeneous microstructure of the electrode can be demonstrated by comparing the lithium-ion concentration histograms obtained using both the RVE and single-particle models [123,128]. **Fig. 4-7** shows the histograms of the lithium-ion concentration obtained at different SOCs during discharge at C-rate of 1.0 using the RVE model. The concentration is distributed in the range from 3,000 to 6,000 mol/m^3 at SOC=95%, 6,000 to 14,000 at SOC=50%, 12,000 to 18,000 at SOC=25%, and 17,000 to 22,500 at the end of discharge. The histograms obtained using the single-particle model,

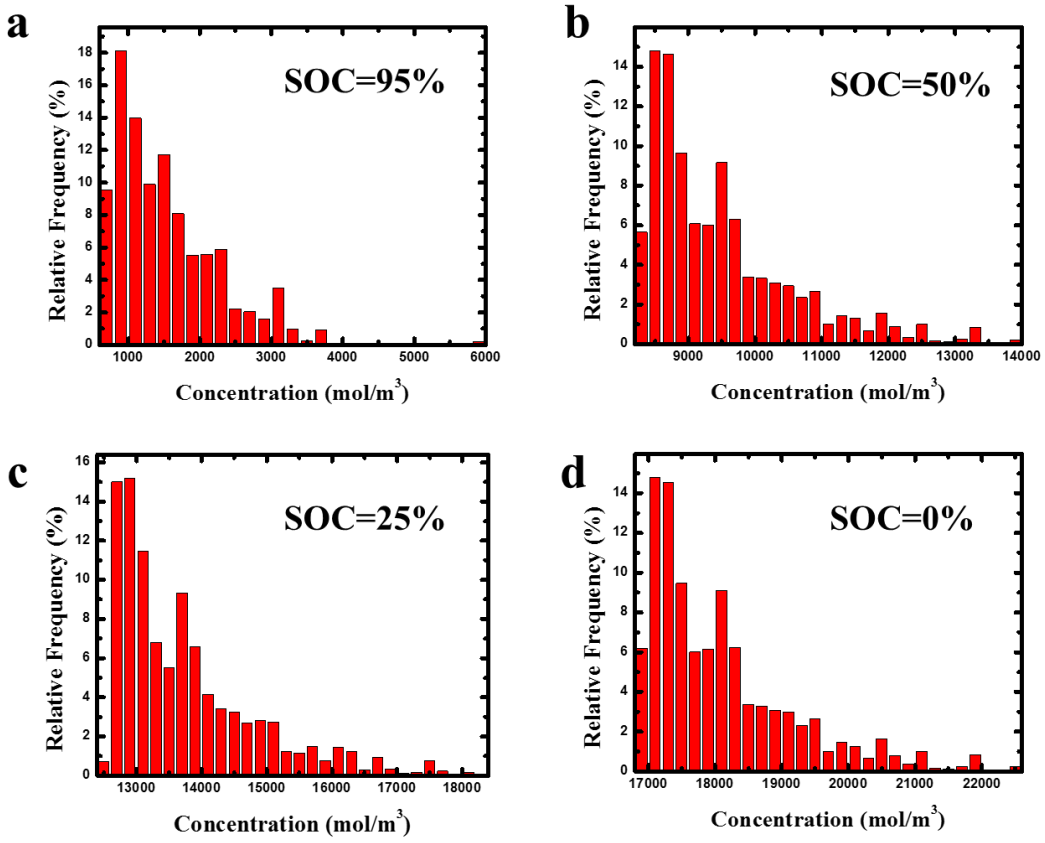

Figure 4-7. Histograms of the lithium-ion concentrations obtained at different SOCs inside the electrode's microstructure using the RVE model during galvanostatic discharge at C-rate of 1.0.

shown in **Fig. 4-8**, is based on the average particle size of 37 nm [33] with all other parameters used the same as the RVE model except D_{LFP} which is found to be 1.3×10^{-19} m^2/s through single-particle model/experiment comparison. The lithium-ion concentration obtained using the single-particle model is shown to be distributed in the range from 3,680 to 3,715 mol/m^3 at SOC=95%, 13,689 to 13,697 at SOC=50%, 18,146 to 18,153 at SOC=25%, and 22,472 to 22,479 at the end of discharge. The wider ranges of lithium concentration observed at different SOCs obtained using the RVE model compared to the single-particle model clearly show that

the RVE model is capable of simulating the inherent heterogeneity inside the electrode's microstructure more accurately. The inhomogeneous distribution of lithium inside the electrode structure has been reported in recent in-situ TXM measurement [131].

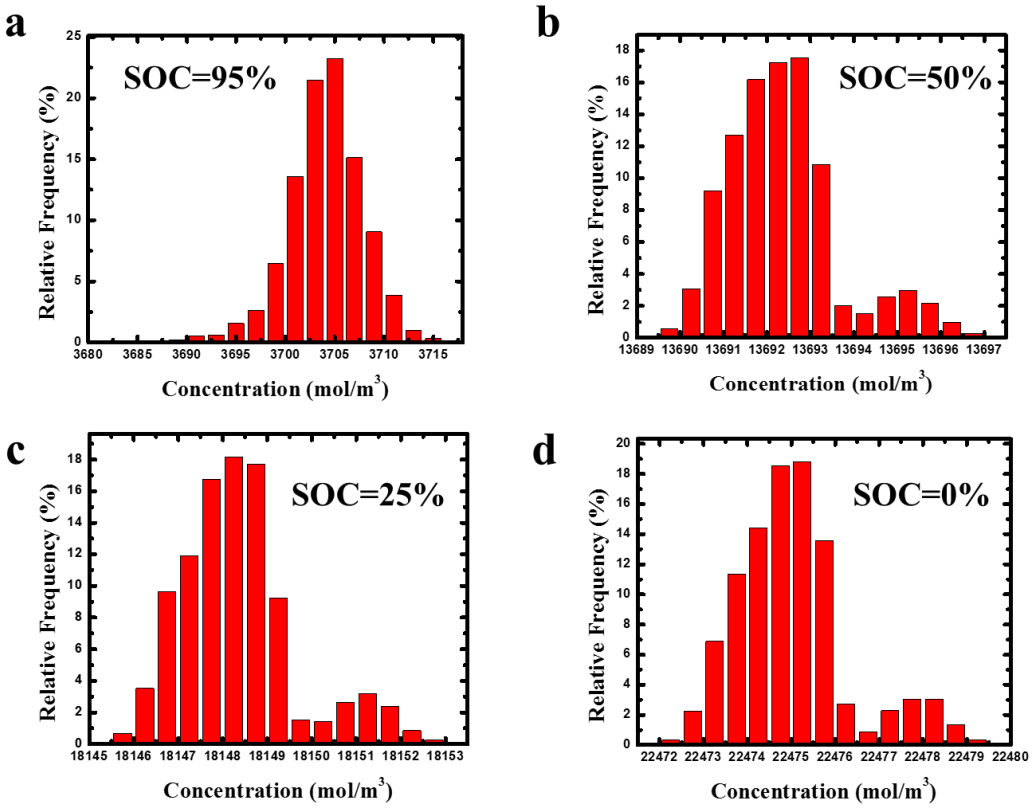

Figure 4-8. Histograms of the lithium-ion concentrations obtained at different SOCs inside the electrode's microstructure using the single-particle model during galvanostatic discharge at C-rate of 1.0.

4.6 Conclusions

In this chapter, a computationally efficient three dimensional RVE model has been successfully developed and validated to accurately predict LIB electrode performance at

different operating conditions. Unlike other LIB models, the real morphology of electrode has been reconstructed by nano-XCT imaging technique, effectively capturing inhomogeneities in the electrode microstructure. The model takes advantage of computational efficiency of the single-particle model, while simultaneously utilizing 3D electrode microstructure as the real geometry. The demonstration of the model and its advantages are discussed for a common LIB electrode consisting of nano-particle LFP active material. Unlike commonly used lithium-ion diffusion coefficient that are in the order of 10^{-19} in spherical particle models, this value is found to be 1.2×10^{-14} m^2/s based on the current model, which is consistent with recently reported experimental data ranging from 10^{-13} to 10^{-15} m^2/s. The simulation results are in good agreement with the discharge profile of LFP cathode at various discharge rates, which have been validated with experimental data. The simulation shows that at any given SOC, the lithium-ion concentration is elevated in the regions with smaller cross-sectional area perpendicular to the diffusion path in the active material and in the region with higher surface area exposed to the electrolyte. Moreover, the distribution of the lithium-ions in RVE is demonstrated to be wider than that of the single-spherical-particle model due to the inherent heterogeneous microstructure. This RVE model opens up many possibilities for future studies of scaled-up battery-cells, battery-packs simulations, as well as thermal and stress studies where the spatial distribution of temperature and intercalation induced stress in the microstructures can be evaluated during battery operation.

5. Morphological and electrochemical characterization of a nanostructure $Li_4Ti_5O_{12}$ electrode using multiple imaging mode synchrotron X-ray computed tomography

This chapter is reprinted in adopted form (from two papers) with permission from Electrochimica Acta and Journal of the Electrochemical Society:

A.G. Kashkooli, G. Lui, S. Farhad, D. U. Lee, K. Feng, A. Yu, Z. Chen, Nano-particle size effect on the performance of $Li_4Ti_5O_{12}$ spinel, Electrochimica Acta 2016, 196, 33–40.

A. G. Kashkooli, E. Foreman, S. Farhad, D. U. Lee, K. Feng, G. Lui, V. D. Andrade, Z. Chen, Morphological and electrochemical characterization of a nanostructure $Li_4Ti_5O_{12}$ electrode using multiple imaging mode synchrotron X-ray computed tomography, Journal of the Electrochemical Society, 2017, 164 (13), A1-A11.

5.1 Introduction

As shown in chapters 3 and 4, application of tomographic techniques, specifically X-ray tomography (XCT) [89,132,133] have provided the microstructure details required for LIBs research. A realistic 3D reconstruction of the LIB porous electrode needs to distinguish three domains: active material, carbon-doped polymer binder domain (CBD), and pore domain. X-ray attenuation is a function of atomic number and density of material. Using nano-XCT, LIB electrodes can also be scanned using two different imaging modes: 1) absorption contrast, where contrast is generated by X-ray absorptivity of the sample; 2) Zernike phase contrast, where the contrast is occurred by phase shift of the X-ray passing through the sample [134].

Therefore, absorption contrast can capture only highly-attenuated cathode active material while leaving the remainder of volume as combination of pore domain and CBD. Lack of CBD in absorption contrast images causes discontinuity within electrode solid domain [135], which significantly decrease the accuracy of solid domain transport properties estimation such as tortuosity [98,136]. On the other hand, using Zernike phase contrast, active materials are imaged along with the CBD [98]. Zernike phase contrast is typically employed to image low-attenuation, low atomic number materials commonly used in the LIB such as graphite and polymer binder [134,137]. As X-ray penetrates the sample both amplitude reduction (active material imaging) and phase change (CBD imaging) of beam occurs resulting in attenuation and refraction of the X-ray. Thereby, the Zernike phase contrast guarantees a connected electrode solid domain comprising percolated network of active materials surrounded by CBD which is suitable for the simulation investigations.

As mentioned previously, traditional models describe LIB electrodes as macro-homogeneous, isotropic porous medium using scalar properties such as particle size, porosity, diffusivity, and conductivity [12,30,78]. Electrode tortuosity is usually used to include decrease of the effective transport properties due to geometric complexity inherent to porous media. The most common approach to calculate tortuosity is Bruggeman relation [138]:

$$\tau = \varepsilon^{1-\alpha} \tag{5-1}$$

Where describe tortuosity τ as a function of porosity ε and the Bruggeman exponent. The value of $\alpha = 1.5$ has been widely used in macro-homogeneous models to calculate effective diffusivity and conductivity. The value was originally obtained from the transport study of a

porous medium consists of equally sized sphere pores [139]. The validity of Bruggeman relation with $\alpha = 1.5$ is controversial; Regarding nano-particle LIB electrode, Thorat *et al.* used AC impedance and current interrupt experimental methods to investigate tortuosity-porosity of $LiFePO_4$ (LFP) electrode [140]. They showed that Bruggeman exponent accurately predict the tortuosity of solid domain, while predict the pore domain tortuosity smaller by factor of 2. Conversely, using heat-mass transport analogy simulation, Ender *et al.* showed that LFP electrode pore domain tortuosity agrees quite well with Bruggeman relation [141], whereas the solid domain tortuosity is found to be two times the one predicted by Bruggeman. Cooper *et al.* measured the pore domain tortuosity by heat transport simulation and showed that Bruggeman underestimates the tortuosity of LFP electrode [63]. They showed that tortuosity is highly dependent on the direction considered and should be considered as a vector rather than a scalar. We also reconstructed the 3D morphology of the LFP solid domain using nano-XCT and presented directional tortuosity of the electrode structure [10]. Moreover, the estimated tortuosities were employed to simulate the electrochemical performance of the electrode at higher length scale in a multiscale modeling framework. Recently, the Shearing group provided a great review on the origin and limitations of the Bruggeman relation and compared several studies on the tortuosity-porosity correlation [142]. They concluded that the Bruggeman equation provide better results when applied to media with sphere or cylinder particles, while special considerations are needed for more complex geometries.

Performance can be sufficiently predicted based on effective transport properties using the tortuosity concept, as in macro-homogeneous models. However, the inclusion of the real electrode 3D structure is required to predict electrode degradation since failure depends on

local inhomogeneities [8]. XCT has enabled the analysis of electrode's local structural effects on physical and electrochemical property distributions. For instance, transport and electrochemical properties within the electrode structure are estimated during battery charge/discharge. Generally, the distribution of these properties are heterogeneous because the electrode structures are heterogeneous [11,66,143], however, the link between XCT data and performance effectively allows quantification of these heterogeneities inside the electrodes.

Herein, we present, to the authors' knowledge, the first 3D microstructural study of $Li_4Ti_5O_{12}$ (LTO) electrode based on multiple imaging mode synchrotron nano-XCT data. LTO is regarded as one of the promising candidate for the anode of the LIB [144,145]. To overcome its inherent low conductivity and sluggish lithium diffusivity, nano-structuring has been proven to be a viable approach [12]. However, it causes a marked challenge for microstructural imaging due to a high resolution requirement (below 100 nm) [10,63]. For this, synchrotron transmission X-ray microscopy (TXM) with a spatial resolution of 58 nm^3 at the Advanced Photon Source (APS) of the Argonne National Laboratory (ANL) is employed. The data is obtained in both absorption contrast and Zernike phase contrast. While the absorption contrast is used to study morphological characteristics of primary and secondary active material particles, Zernike phase contrast is combined with absorption contrast to resolve the CBD within the electrode structure. Cooper *et al.* imaged a nano-particle LFP cathode with nano-XCT and explored the microstructural heterogeneity within the 3D reconstructed pore domain based on the tortuosity calculations [63]. Similarly, we have employed absorption and Zernike phase contrast reconstructed structures as the foundation to

determine the electrode tortuosity for pore and solid domains, respectively. The geometrical and transport based tortuosity are estimated which sheds light into the complex anisotropic nature of heterogeneous electrodes. In addition to tortuosity, the effects of local microstructural heterogeneity on the physical and electrochemical processes occurring during cell operation have been investigated. For this, galvanostatic discharge performance of the LTO half-cell electrode is simulated based on our recently published work, representative volume element (RVE) model, developed for LIB [11]. Nano-XCT simulation studies typically use absorption contrast 3D reconstructed as the model geometry [10,66]. As mentioned, CBD cannot be distinguished from pore domain in absorption contrast which may lead to isolated active material particles. Image processing techniques are usually employed to merge the active materials together and form an integrated solid domain required for continuum simulations [10,63,66]. However, Zernike phase contrast geometry employed in the current model, provides a united percolated network of active materials and CBD which eliminates the 3D reconstruction error. Our previous RVE model [11] is improved further by incorporating the charge transport within the microstructures to the governing equations. The model includes conservation of mass and charge within solid domain plus the electrochemical kinetics and is validated with the experimental data obtained from half/coin-cell performance. The model does not consider the local variation of lithium-ion concentration inside the electrolyte, instead, an electrolyte resistance term is employed to account for the electrolyte resistance.

This chapter is organized as follows: first, LTO synthesis and characterization methods are described. Then, the electrode fabrication and imaging techniques used to obtain 3D

reconstructed electrode morphology are discussed. Then, the FEM basis for calculating tortuosity using heat and mass transport analogy is reviewed. Then, the modeling development including RVE selection, followed by the governing equations used to simulate electrochemical performance are presented. Finally, the simulation results are demonstrated and discussed with concluding remarks.

5.2 Experimental

5.2.1 Synthesis of $Li_4Ti_5O_{12}$

Direct synthesis of monodispersed LTO particles is difficult due to methods by which they are synthesized [146–148]. Hydrothermal and solid-state methods often lead to particle agglomeration or sintering, which increases the complexity and reduces the reliability of a model for such a system [20,149]. We have found that the simplest and most reliable route for LTO synthesis would be a two-step process: 1) synthesis of monodisperse TiO_2 particles; and 2) solid-state conversion of TiO_2 to LTO particles using carbon as a means of blocking Ti diffusion and suppressing TiO_2 sintering, thereby maintaining individual particle morphology [150] .

Almost monodispersed LTO nanoparticles were synthesized as outlined in the literature [151]. In a typical synthesis, 0.4 mL 0.1 M KCl solution was added to 100 mL ethanol. 2.5 mL titanium butoxide was added to the solution and stirred for 10 minutes. The solution was then aged at ambient temperature for 18 hours to form TiO_2 nanoparticles. After aging, the nanoparticles were centrifuged and washed several times with de-ionized water and ethanol before drying overnight at 60°C. In order to aid the conversion of TiO_2 to LTO, the TiO_2 nano-

particles were heat treated to 500°C at 1°C min^{-1}. This brief heat treatment was used to form crystalline anatase with a small domain size, which has been shown to reduce the onset conversion temperature to LTO and increase LTO purity [152].

Both carbon-coating and conversion to LTO were achieved in a one-step pyrolysis reaction. TiO_2 nanoparticles were first dispersed in an aqueous solution containing 10 wt% glucose and stirred at 70°C in a sealed container for several hours. After adequate mixing, the solution was dried in an oven at 80°C to form a light brown powder. The nanoparticles were then thoroughly mixed with lithium carbonate in a molar ratio of 1:1.03 and heated to 800°C for 6 h in Ar atmosphere to achieve carbon-coated LTO nanoparticles.

5.2.2 Characterization

The morphology and crystal structure of all materials were confirmed using field-emission scanning electron microscopy (FESEM, Zeiss ULTRA Plus; 10 kV acceleration voltage), X-ray diffraction (XRD, Bruker AXS D8 Advance), and Raman spectroscopy (Bruker SENTERRA; 532 nm 20 mW laser). The morphology of LTO nano-particles has been confirmed using SEM. The images show a narrow particle size distribution with a diameter of 250 nm (**Fig. 5-1 a, b**). The crystallinity and phase of the nano-particles have been confirmed using XRD and Raman characterizations. The XRD pattern confirms a pristine spinel phase $Li_4Ti_5O_{12}$ [144], (see **Fig. 5-1c**). Raman spectrum shows typical vibration modes of spinel phase LTO with the addition of characteristic D and G bands that correspond to graphitic carbon which have formed during the second stage of LTO synthesis [153], see (**Fig. 5-1d**).

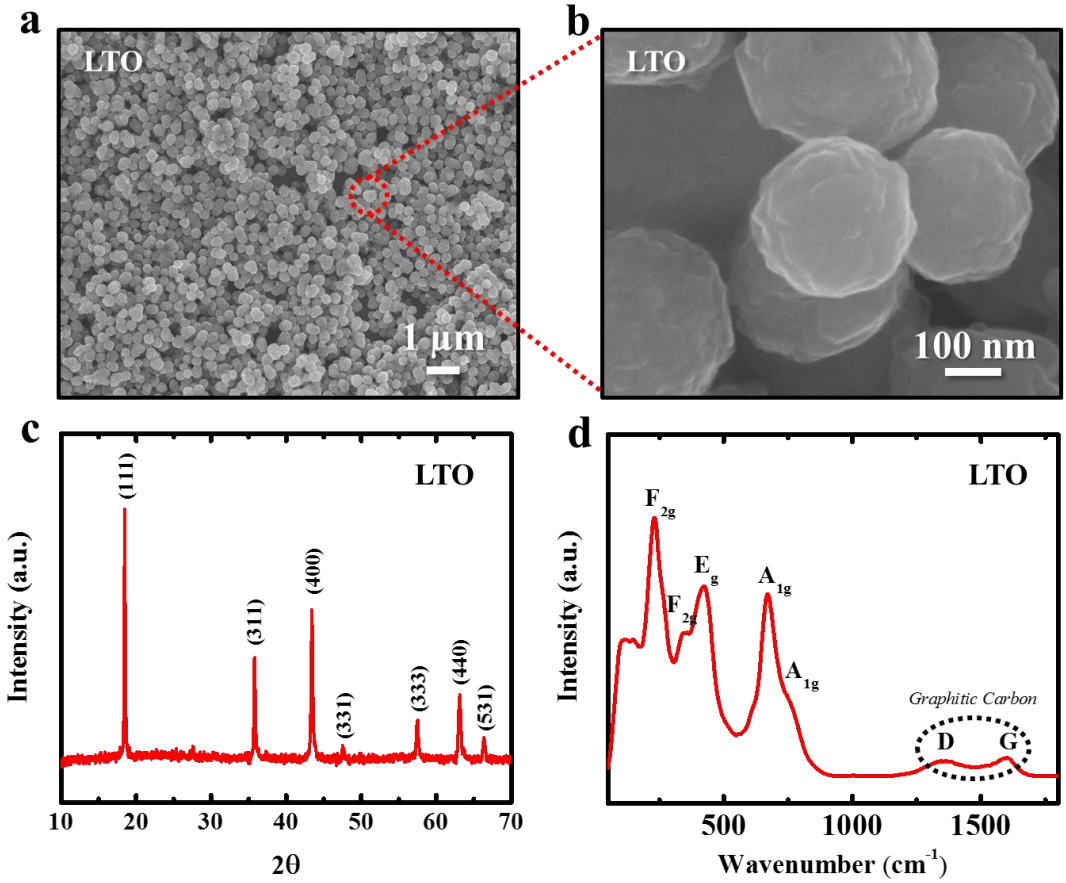

Figure 5-1. Characterization of as-synthesized LTO nanoparticles. (a), (b) SEM image of LTO nanoparticles, (c) XRD and (d) Raman spectra of LTO material.

5.2.3 Cell fabrication

The experimental performance of the LTO nanoparticles was determined by fabricating coin half-cells. An electrode slurry containing LTO was created using Super-P carbon black as the conductive additive, Polyvinylidene fluoride (PVDF) as the binding agent, and 1-methyl-2 pyrolidinone (NMP) as the solvent. The ratio between LTO, Super-P, and PVDF was 90:5:5. The slurry was then cast on a Cu foil current collector using a doctor blade and dried overnight

in a vacuum oven at 100°C. Four coin half-cells were fabricated to determine electrochemical performance of the electrodes. All the cells were fabricated in identical condition to assure the repeatability of the results. The coin cells utilized a lithium-foil as the reference/counter electrode, a Celgard 2500 as separator, and a 3:7 *(v/v)* ethylene carbonate and dimethyl carbonate organic solution containing 1 M hexafluorophosphate ($LiPF_6$) as electrolyte. Coin cells were assembled in an argon-filled glove box (H_2O < 0.5 ppm, O_2 < 0.5 ppm). Charge-discharge cycling was conducted using a NEWARE BTS-5V 10 mA battery testing station. All cells were cycled at C rates ranging from 0.2 C to 5 C (theoretical capacity of LTO, C = 175 mAh/g) within a voltage window of 1.0-2.5 V.

5.2.4 Nano-XCT

The samples for X-ray imaging were obtained by dissolving electrode's copper foil in nitric acid. Since copper influences the X-ray attenuation, the current collector needed to be delaminated. Synchrotron radiation nano-XCT was conducted using Transmission X-ray Microscope at Advanced Photon Source (APS), Argonne National Laboratory (sector 32-ID-C) [59]. Tomographic data was obtained using an 8 keV monochromatic beam. The tomographic images were obtained by rotating the sample 180° using a step scan increment of 0.5° and the exposure time of 1 second at each increment. The X-ray objective lens used to magnify radiographs was a 58 nm outermost zone width Fresnel zone plate, providing a spatial resolution of 58 nm. The 3D reconstruction was performed with Tomopy, an open source collaborative framework for the analysis of synchrotron tomographic data [125,126]. The reconstructed volume represents voxel of attenuation coefficient with a width of 58 nm after

binning. The total number of virtual slices were 1024 with 58 nm cubic voxels resolution and field of view of 1024 × 1224 × 1224 voxels. The LTO sample was imaged using two imaging modes: absorption contrast and Zernike phase contrast.

Image processing and segmentation of grayscale 3D image was achieved using the commercial software Simpleware. First, to reduce background image noise, a median filter with the cubic neighborhood radius of 3 pixels was applied. Median filters are effective to remove salt-and pepper noise and remove the outliers. It computes the value of each pixel as the statistical median of the neighborhood pixel around the corresponding pixel. Then, a mean filter with the cubic neighborhood radius of 1 pixel was applied for further noise reduction. The filter finds the value of each pixel by calculating the statistical mean of the neighboring pixels. Segmentation is achieved using binary thresholding. Unwanted noise and details was removed using a recursive Gaussian filter with cubic Gaussian sigma value of 1. Gaussian sigma is a parameter that determines how many neighboring pixels should contribute to the smoothing operation of corresponding pixel. The larger the sigma, the stronger the smoothing. To form a 3D pore network, a copy of the pore domain was created and then was inverted on all slices in the whole cubic domain. This is similar to the Boolean operation usually employed elsewhere, where the solid domain is subtracted from the cubic solid.

Fig. 5-2a and **5-2b** show two raw virtual slices obtained from absorption contrast and Zernike phase contrast modes, respectively. With relatively larger field of view of ~70 μm, and having small primary nano-particles, it is hard to differentiate various components such as active material and CBD in the virtual slices. Therefore, we zoomed on a smaller cubic region with the side of 10.4 μm^3, to distinguish between absorption and Zernike phase contrast

images. **Fig. 5-2c** and **5-2d** show cubic grayscale image of the electrode from reconstructed morphology based on absorption contrast and Zernike phase contrast, respectively (the cube side is 10.4 µm corresponding to 180 × 180 × 180 voxels). In absorption contrast, the white region represents the active material and black region shows the pores plus CBD (see **Fig. 5-2c**), whereas in Zernike phase contrast, white region represents active material plus CBD and black region shows the pores (see **Fig. 5-2d**). Fig. **5-2e** and **5-2f** show binary segmented regions obtained from the absorption contrast and Zernike phase contrast modes, respectively, which are applied to the image processing steps described. As previously shown by Babu *et al.* [98] the active material and CBD could be separately resolved by combining absorption contrast and Zernike phase contrast images. As mentioned, in absorption contrast, solid domain comprises active material, whereas in Zernike phase contrast, it includes active material as well as CBD. To capture the CBD, absorption contrast image needs to be subtracted from Zernike phase contrast to eliminate the active material. **Fig. 5-2g** shows the segmented 2D tomogram of the LTO electrode. In this figure, the domains of the active material, CBD, and pore separated from each other can be easily distinguished. A 3D image of the electrode's solid domain distinguishing active material and CBD is demonstrated in **Fig. 5-2h**. In addition, **Table 5-1** compares the volume fraction of different electrode phases obtained from XCT reconstruction and electrode fabrication. The electrode fabrication fraction were calculated based on the actual mass ratio (90:5:5) and material density ($\rho_{LTO} = 3.5\ g/cm^3, \rho_{CB} = 1.8\ g/cm^3, \rho_{PVDF} = 1.77\ g/cm^3$) . The small deviation in volume fractions is attributed to XCT low resolutions wherein the structure sizes below 58 nm^3 could not be captured.

Table 5-1. The volume fraction of different phases of the nanostructured LTO electrode based on the reconstruction data and the actual mass ratio.

	XCT	Electrode fabrication
LTO	0.33 (absorption contrast)	0.35
LTO+CBD	0.43 (Zernike phase contrast)	0.43
CBD	0.10	0.08
Pore	0.57	0.57

The lack of CBD in absorption contrast images may cause isolated LTO particles. This can increase computational cost due to having multiple regions in solid domains. In the literature, a filter or a dilation function on the solid domain is commonly employed to preserve the domain connectivity [10,135] or alternatively, very low content of carbon black (3%) and binder (3%) are added to the electrode during fabrication to reduce the reconstruction error [154]. However, the Zernike phase contrast reconstructed structure used in this study, provides a united percolated network of active materials and CBD, suitable for the FEM simulation, (see **Fig. 5-1e**). This eliminates the error associated with the neglecting low density carbon and binder phase in synchrotron based FEM simulations.

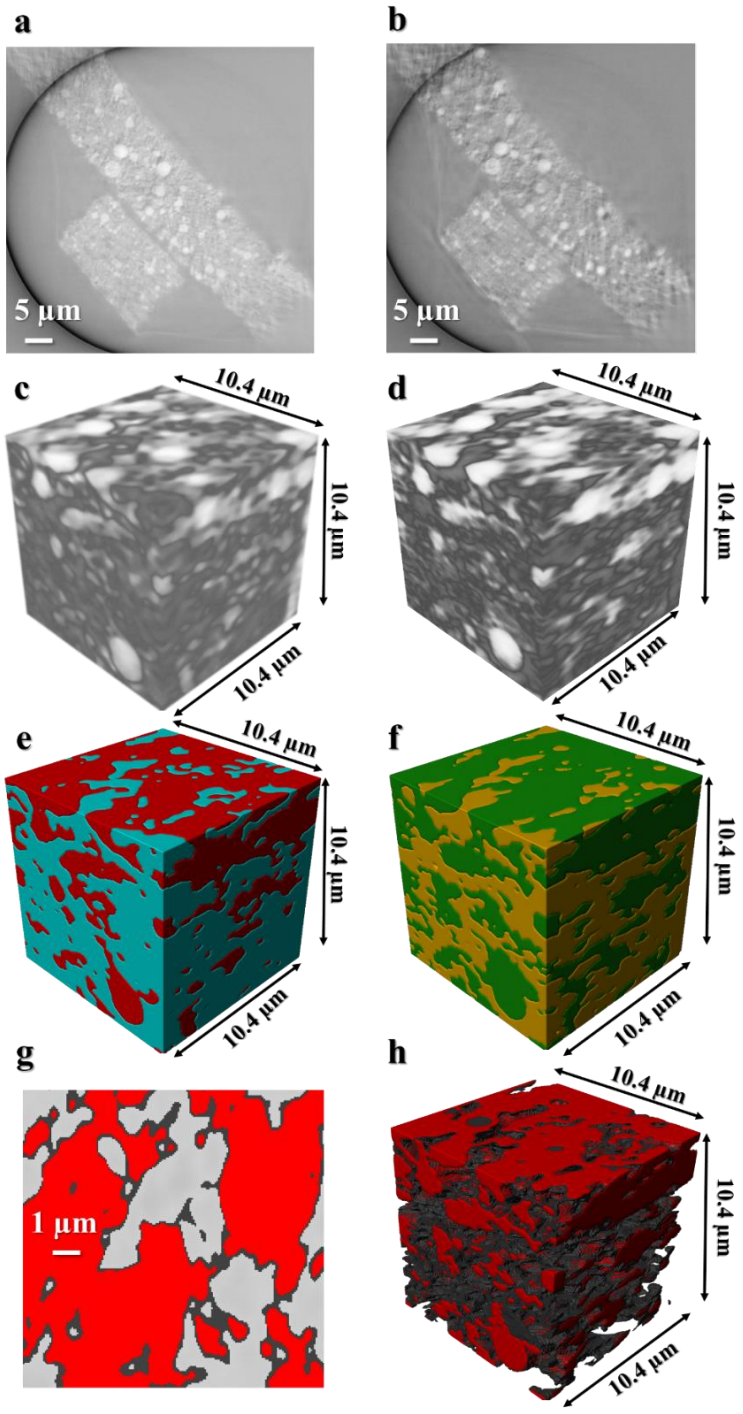

Figure 5-2. Raw grayscale 2D morphology of the electrode obtained using a) absorption contrast, and b) Zernike phase contrast imaging modes. Reconstructed 3D microstructure c) absorption

contrast and d) Zernike phase contrast. Segmentation of the regions using e) absorption contrast (red: active material, light blue: pores plus CBD) and f) Zernike phase contrast (green: active material plus CBD, dark yellow: pores). Active material (red), CBD (dark gray) and electrolyte (light gray) are distinguished by combining absorption and Zernike phase contrast imaging modes: g) 2D tomogram and h) 3D reconstruction.

5.3 Modeling

5.3.1 Morphological and transport properties

The original 3D reconstruction of the electrode sample was a non-cubic geometry that later was cropped to the largest possible cubic volume with the size of 260 × 800 × 800 cubic isotropic voxels corresponding to the overall volume of 29216 μm^3. Various morphological characteristics are purely geometrical and do not require numerical simulation. We quantified morphological parameters including electrode porosity, ε, volume specific surface area, a, and geometrical tortuosity, τ_{geom}, as morphological characteristics. The electrode porosity, ε, and volume specific surface area, a, are critical input for macro-homogeneous models. In case of volume specific surface area, macro-homogeneous models usually use simplified geometry such as: single-sized and multi-sized spherical particles, or complex computer generated geometries. The volume specific surface area, then is estimated based on the assumed structure. For example, for spherical particles, the volume specific surface area of the electrode, can be computed by [30,127]:

$$a = \frac{3\,(1-\varepsilon)}{R_s} \tag{5-2}$$

Where, R_s, is the average particle size.

For the transport properties estimation, to have a cubic geometry, a region with 180 × 180 × 590 corresponding to 3730 μm^3 was chosen (See **Fig. 5-3** for the pore domain demonstration of the region). Although the selected region includes just 11% of the original image volume, this region is quite large (6×10^6 times larger) compared to the nano-size of active material particles. There are two types of tortuosity: 1) geometrical tortuosity, which is the ratio of the actual path length between two points to their Euclidean distance (straight line distance); 2) transport tortuosity, which accounts for the decrease of transport phenomena due to the geometrical complexity of pores network. Geometrical tortuosity is calculated by dividing the actual path length between two points by the straight-line distance. The average geometrical tortuosity in each direction is estimated by [141]:

$$\tau_{geom} = \langle \frac{\min(L)}{D} \rangle \tag{5-3}$$

Where τ_{geom}, is the average of the shortest centroid path length, L, through the microstructure divided by D, which is the straight-line distance. To obtain transport tortuosity, a FEM simulation on the pore and solid domains are performed, where the diffusion and conduction are described by Laplace equation:

$$\nabla.\,(k\nabla T) = 0 \tag{5-4}$$

In this equation, k is the transport coefficient (i.e. diffusivity or thermal conductivity or electrical conductivity) and T is the Temperature. **Fig. 5-3** shows the reconstructed pore domain, based on absorption contrast, used for the transport tortuosity estimation. For each directional tortuosity, temperature is arbitrarily set as 0 and 1 at inlet and outlet faces of cubic domain and the heat flux is specified as zero at all other boundaries. From the simulation results, J, the area heat flux integral at the outlet or inlet boundary is calculated by:

$$J = \int_S k \frac{\partial T}{\partial x_i} dS \tag{5-5}$$

Where, S is the outlet or inlet surface boundary and i is the coordinate direction. Then, the effective conductivity, k_{eff}, can be calculated by:

$$k_{eff} = \frac{J}{A} \frac{L}{\Delta T} \tag{5-6}$$

Where, ΔT is temperature difference considered at two opposite walls, which here it was set to 1, A is the cross section perpendicular to the heat transfer direction, and L is the distance between inlet and outlet boundary. Tortuosity is:

$$\tau = \frac{\varepsilon\, k}{k_{eff}} \tag{5-7}$$

If we place **equations (5-5)** and **(5-6)** into **eq. (5-7)**, the transport tortuosity can be calculated by:

$$\tau_i = \frac{\varepsilon A}{L \int_S \frac{\partial T}{\partial x_i} dS} \tag{5-8}$$

Eq. (5-8) shows that the transport tortuosity, τ_i, is not a function of thermal conductivity, k, and the tortuosity factor is the same for all transport phenomena including heat and mass transport. The same approach can be applied on the reconstructed solid domain which is not shown here.

Macro-homogenous models commonly use the Bruggeman relation (see **Eq. (5-1**)) with $\alpha = 1.5$ as the basis for calculating tortuosity. The Bruggeman equation is based on the transport study with the assumption of isotropic and homogeneous pore domain. This assumption provides one unique tortuosity for the whole electrode. To be able to compare the directional tortuosities obtained from 3D simulation to Bruggeman tortuosity, Cooper *et al.* [63] introduced a characteristic tortuosity τ_c as:

$$\tau_c = 3\left[{\tau_x}^{-1} + {\tau_y}^{-1} + {\tau_z}^{-1}\right]^{-1} \tag{5-9}$$

Where, τ_x, τ_y, τ_z are directional tortousities. Cooper *et al.* [63] also suggested that τ_c can be used in the 1D micro-homogeneous model instead of Bruggeman tortuosity.

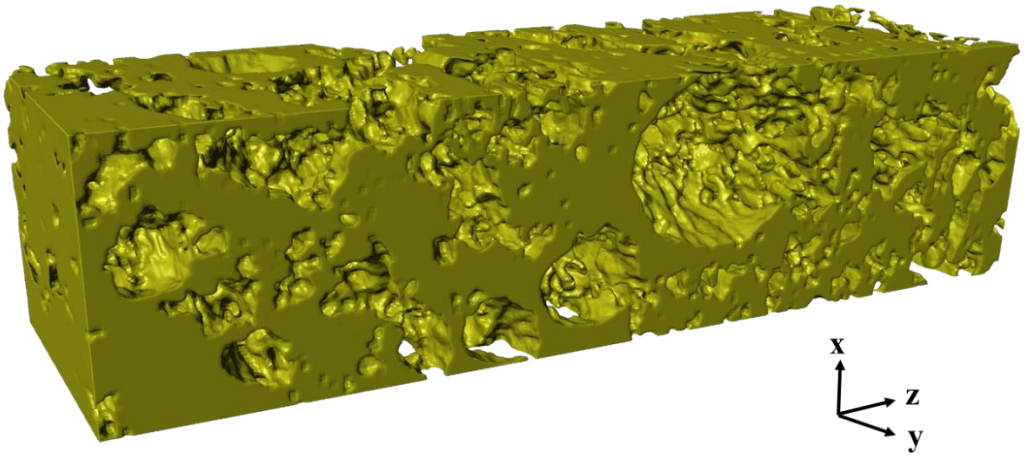

Figure 5-3. 3D visualization of the LTO electrode's pore domain obtained using nano-XCT in absorption contrast mode. The structure size is 10.4 × 10.4 × 34.2 µm^3, which corresponds to 180 × 180 × 590 voxels, (The direction of Z is through-plane).

5.3.2 Electrochemical performance

5.3.2.1 RVE selection

The electrode RVE is a sub-section volume wherein a measured property can be considered as a representative value for the whole electrode [11]. In this study, the properties of interest for the determination of a suitable RVE size are the electrode porosity and volume specific surface area which is the ratio of interfacial solid/pore domains surface area to the electrode volume. **Table 5-1** shows sample volume specific surface area and porosity of a cubic RVE sub-section of different sizes obtained from Zernike phase contrast reconstruction. The whole domain porosity is 0.57. For a RVE size of 3.48 µm and larger, the porosity of the sub-sections lies within 2 % of the whole electrode porosity. In addition, the electrode's volume specific surface area is 1.24 (1/µm), thus remaining within 3% of the domain volume specific surface

area for sizes of 3.48 μm and larger. Accordingly, the smallest appropriate RVE of the electrode is selected as 3.48 μm size. This calculation is based on the selection of sub-sections from one corner of electrode sample. To decrease the error associated with the selection of specific region in the electrode position, in the present study a volume with side length of 7 μm (see **Fig. 5-4**) have been selected as electrode RVE and model geometry for electrochemical performance simulation even though we may have selected the smallest possible size (i.e. 3.48 μm).

Table 5-2. The electrode's porosity and the solid domain volume specific surface area shown in sub-sections of the electrode sample with various sizes.

Cube size (μm)	Porosity, ε	Volume specific surface area, a ($1/\mu$m)
1.16	0.45	1.40
1.74	0.47	1.37
2.32	0.50	1.39
3.48	0.58	1.26
4.64	0.57	1.22
5.80	0.55	1.26
6.96	0.56	1.29
8.12	0.57	1.26
9.28	0.55	1.22
10.3	0.56	1.24

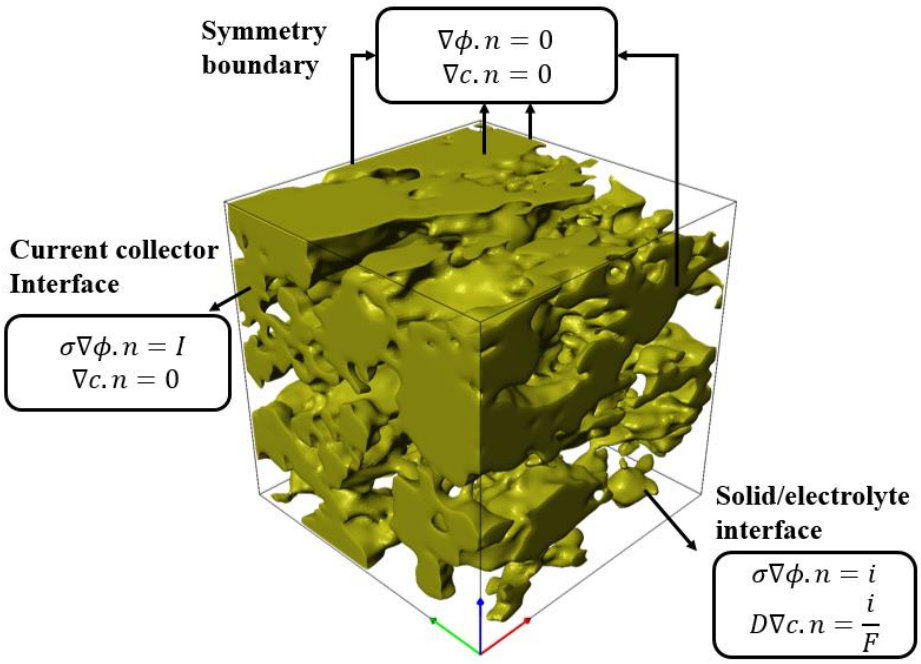

Figure 5-4. An RVE (cube side length = 7 µm) of the electrode's solid domain extracted from Zernike phase contrast 3D reconstruction for half-cell performance simulation with boundary conditions for specific RVE surfaces used to calculate the governing equations.

5.3.2.2 Governing equations

The governing equations employed in this study are the conservation of mass and charge within the electrode solid domain. The variations of lithium-ion concentration and electric potential within the electrolyte are neglected and electrolyte polarization has been modeled by a constant resistant parameter. The lithium diffusion within the solid domain is modeled by Fick's mass transport law as [10,66]:

$$\frac{\partial c_1}{\partial t} = \nabla.(D_1 \nabla c_1) \tag{5-10}$$

Where, c_1 is lithium concentration in the RVE, D_1 is the lithium diffusivity in the solid domain, and ∇ operates on the spatial coordinates. To distinguish different regions in the porous electrode, subscripts 1 and 2 are utilized to identify the solid and electrolyte domains, respectively. The electric potential within solid domain is calculated using conservation of charge and Ohm's law:

$$\nabla.(\sigma_1 \nabla \phi_1) = 0 \tag{5-11}$$

Where, ϕ_1 is the electric potential within REV, σ_1 is the solid phase electrical conductivity. As shown in **Fig. 5-4**, at the solid/electrolyte interface the boundary conditions for governing equation are [10,66]:

$$D_1 \nabla c_{1,s}.n = j_n \tag{5-12}$$

$$\sigma_1 \nabla c_{1,s}.n = i_{loc} \tag{5-13}$$

Where, j_n is the normal component of lithium mass transport flux at the solid/electrolyte interface, *s* refers to the solid/electrolyte boundary, and *n* is the normal unit vector to the interface, pointing toward the electrolyte. j_n is depended on applied current density as [11]:

$$j_n = \frac{i_{loc}}{F} = \frac{I}{F(1-\varepsilon)a\mathrm{L}} \tag{5-14}$$

where, i_{loc} is local current density at the interface, *I* is the applied current density on the electrode in half-cell, F is Faraday's constant, ε is the electrode porosity, *a* is the specific surface area of the interface per volume of the solid domain, and *L* is the electrode thickness. The rate of electrochemical reaction is obtained using Butler-Volmer kinetics as [127]:

$$i_{loc} = i_0\left(exp\left(\frac{\alpha F}{RT}(\phi_1 - U)\right) - exp\left(-\frac{(1-\alpha)F}{RT}(\phi_1 - U)\right)\right) \quad (5\text{-}15)$$

where, α is charge transfer coefficient, R is the universal gas constant, T is temperature, and U is the open circuit potential and i_0 is the exchange current density defined as [127]:

$$i_0 = Fk_0(c_2)^{\alpha}\left(c_{max} - c_{1,s}\right)^{\alpha}(c_{1,s})^{\alpha} \quad (5\text{-}16)$$

Where, k_0 is rate constant of the reaction, c_2 is concentration of lithium-ion in electrolyte which is considered constant in this study.

At the interface of the cathode and current collector, the charge transfer flux should be determined by applied current, I. A symmetric boundary condition is applied on all other surfaces. At the lithium counter electrode, $V = 0$ and separator resistance is neglected. Therefore, the overall half-cell voltage can be determined by:

$$E = \phi_1 - IR_2 - U \quad (5\text{-}17)$$

Where, R_2 is the electrolyte resistance which represents the potential drop inside the electrolyte between the electrode and lithium foil counter electrode. In this study, R_2 is considered an adjustable parameter that is determined by comparing simulation results with half-cell performance data [123,128].

5.4 Results and discussion

The SEM image of the LTO electrode consisting of primary nano-particles is shown in **Fig. 5-5a**. As a comparison, a raw 2D radiograph of the electrode has been obtained from nano-XCT as shown in **Fig. 5-5b**, which showed a similar 2D morphology. In addition, because the

absorption contrast mode does not capture carbon additives and polymer binder, only the distribution and morphology of the active material particles are observed. The 2D electrode images also demonstrate that some nano-particles tend to agglomerate and form micron-sized secondary particles (See **Fig. 5-5**) that vary in size ranging from 2 to 5 μm. It is noted that due to the relatively lower resolution of nano-XCT than SEM, the primary particles inside the secondary particles are not "visible" in nano-XCT images as can be observed in **Fig. 5-5b**.

In order to analyze the geometrical morphology of the secondary particles, four well-resolved secondary particles have been selected as shown **Fig. 5-6** with non-uniform surfaces and different morphologies. **Table 5-2** lists the 3D morphological information including size, volume specific surface area, and sphericity of the four particles. The particle sphericity is determined by dividing the surface area of the particle by the surface area of a sphere with the same volume, with the lower sphericity values indicating stronger non-sphericity. All particles are non-spherical with particle 4 showing the highest degree of non-sphericity, ca. 0.71. Moreover, particles 3 and 4 have sharp sandglass type structures at the corners, which would challenge the assumptions made for microstructure homogeneities in conventional macro-homogeneous models. The volume specific surface area of the secondary particles, ~3 (1/μm), is much higher than the one obtained using Zernike phase contrast mode, 1.24 (1/μm), see **Table 5-1**; This could be attributed to the inclusion of CBD in Zernike phase contrast mode which covers some part of the particle surface to provide electron conduction.

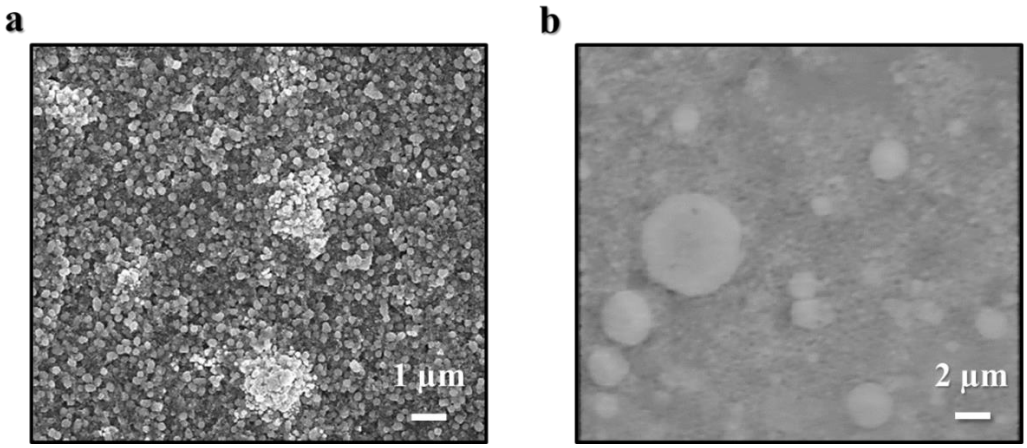

Figure 5-5. (a) Typical SEM image of the LTO electrode, and (b) its 2D radiograph obtained from nano-XCT using absorption contrast mode.

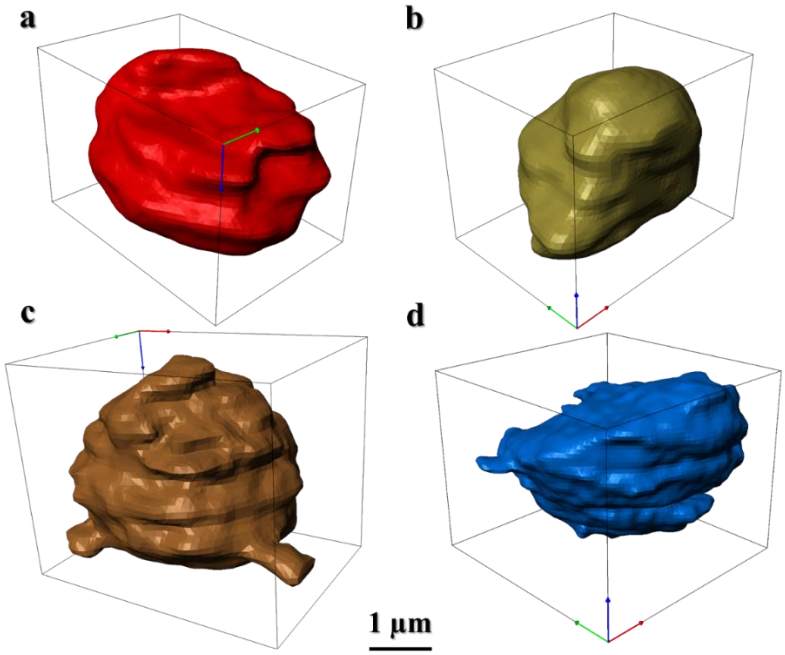

Figure 5-6. Four isolated LTO secondary particles obtained using absorption contrast imaging mode. (a) particle (1), (b) particle (2), (c) particle (3), (d) particle (4). The microstructure data for these particles are listed in Table 5-2.

Table 5-3. Microstructural information of the four secondary particles obtained using absorption contrast mode of nano-XCT.

Particle	Sphericity (perfect sphere=1)	Volume specific surface area, a (μm^{-1})	Cube outline dimensions (μm)
1	0.85	3.14	$2.96 \times 2.08 \times 1.96$
2	0.93	3.30	$2.52 \times 1.96 \times 1.96$
3	0.79	3.62	$2.84 \times 2.08 \times 2.24$
4	0.71	3.23	$3.36 \times 3.48 \times 2.68$

To investigate the validity of the homogeneity and isotropy of the electrode's microstructure hypothesized in most macro-homogeneous models, transport tortuosities of the pore and solid domains has been simulated and compared in different directions. In case of pore phase geometry, both absorption contrast and Zernike phase contrast modes can be used to reconstruct the model geometry. As mentioned before, the absorption contrast mode includes the volume of CBD in the pore phase. Therefore, the resulting tortuosity obtained using the absorption contrast mode underestimates the pore tortuosity. On the other hand, Zernike phase contrast is not capable of resolving nano-pores within CBD as their size is relatively smaller compared to the resolution of nano-XCT resolution (58 nm). Instead, the CBD is included in the solid domain, which results in enhanced pore phase tortuosity values [155]. In this study, absorption contrast is chosen as the model geometry to quantify pore

phase transport tortuosity in agreement with ref. [63]. Alternatively, for solid phase tortuosity, Zernike phase contrast 3D reconstructed structure is employed to provide an inter-connected network for the solid structure. This guarantees successful electron transport within the solid domain.

Table 5-3 presents the transport tortuosities obtained from heat-mass transport analogy for the solid and pore domains, respectively. In addition, **Table 5-3** shows characteristic tortuosity, τ_c, estimated from the directional tortuosities using **eq. (5-8)** and Bruggeman tortuosity, τ_B, calculated from **eq. (5-1)**. **Table 5-3** shows that through-plane tortuosity τ_z, for both pore and solid domains is higher than in-plane τ_x, τ_y, demonstrating higher ionic and electronic transport resistance in the through plane direction. In addition, different directional tortuosity values confirm the inherent heterogeneous structure of electrode, neglected in macro-homogeneous models. Characteristic tortuosity, τ_c for the pore and solid domains are 1.70 and 2.08, respectively, which is higher than the ones predicted by Bruggeman, 1.32 and 1.52. The results show that Bruggeman correlation is a poor estimator of electrode tortuosity. This is due to the fact that Bruggeman is based on homogeneous electrodes with spherical particles.

Table 5-4. Porosity and heat transport analogy derived directional tortuosities of the pore and solid phases obtained using absorption contrast and Zernike phase contrast modes, respectively.

	Pore phase	Solid phase
In-plane directional tortuosity, τ_x	1.46	1.37
In-plane directional tortuosity, τ_y	1.69	2.19
Through-plane directional tortuosity, τ_z	2.07	3.86
Characteristics tortuosity, τ_c	1.70	2.08
Bruggeman tortuosity, τ_B	1.32	1.52

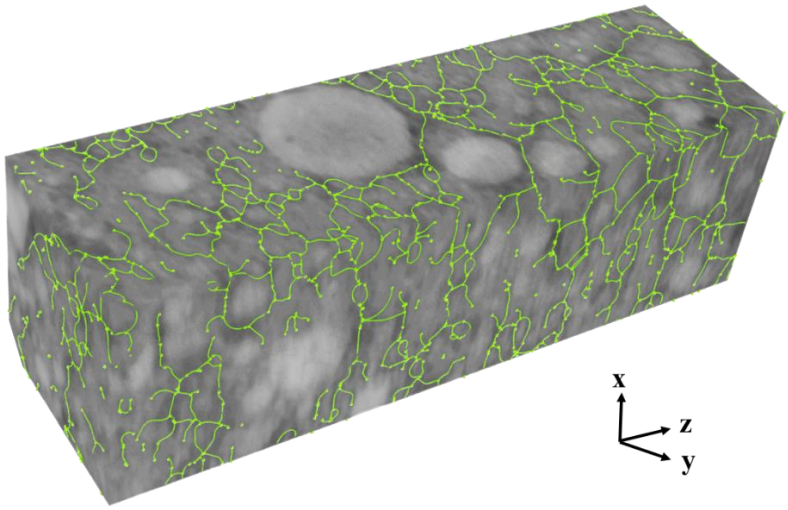

Figure 5-7. Pore network centroid at the boundaries of the 3D reconstructed electrode. The segmentation is obtained using absorption contrast mode, and the structure size is 10.4 × 10.4 × 34.2 μm^3 which corresponds to 180 × 180 × 590 voxels, (The direction of Z is through-plane).

ScanIP has a function to calculate a type of geometrical tortuosity based on the pore network tortuous paths. In order to calculate geometrical tortuosity, pore network centroid within 3D reconstructed geometry has been constructed as shown in **Fig. 5-7**. The tortuosity is then calculated by dividing the centroid motion path between two points length by the straight-line distance. We have estimated the average geometrical tortuosity in each direction according to **eq. (5-3).** Employing **eq. (5-3)** τ_{geom}, is averaged over 20 different paths for each starting point on the structure boundary where the end point is located on the opposite boundary. The same approach was used on the solid domain obtained from phase contrast mode. **Table 5-4** demonstrates geometrical tortuosity in each direction along with characteristics tortuosity, τ_c, for both pore and solid domains. The calculated geometrical tortuosities are lower compared to transport based tortuosities, except for τ_x. Moreover, similar to transport tortuosities, geometrical tortuosities also show clear dependence to the direction with higher through-plane (thickness direction) tortuosity τ_z, compared to the in-plane τ_x, τ_y. This again confirms the heterogeneous and anisotropic nature of LIB porous electrodes. For LFP cathode, Cooper *et al.* described a logarithmic relation between geometrical and transport tortuosities for a nano-structured LFP cathode using various electrode sub-volumes [63]. However, this correlation was not observed in the present study.

Table 5-5. Surface area and geometrical based directional tortuosities of the pore and solid phases obtained using absorption contrast and Zernike phase contrast modes, respectively.

	Pore phase	Solid phas
In-plane directional tortuosity, τ_x	1.53	1.51
In-plane directional tortuosity, τ_y	1.68	1.94
Through-plane directional tortuosity, τ_z	1.81	2.02
Characteristics tortuosity, τ_c	1.67	1.79

In addition to tortuosity, the electrode microstructures influence the physical and electrochemical properties distribution inside the electrode. Macro-homogeneous models are successful and computationally efficient to predict the LIB performance [12,156,157] while they fail to predict the electrode degradation and failure of the battery. They employ isotropic, homogeneous spherical particles in microstructure scale as the model geometry, resulting in a homogeneous distribution of physical and electrochemical properties inside the electrode particles [12]. At the electrode level, they consider the local average value of properties along the direction of electrode thickness, disregarding the microstructural effects [50]. Therefore, property distributions vary along the direction of electrode thickness, and they typically represent a certain trend [50]. On the other hand, heterogeneous models include heterogeneous microstructure of the electrodes as the geometry. This leads to the heterogeneous physical

and electrochemical processes which cause the resulting distribution of properties to show no specific trend [66].

Moreover, it is shown that heterogeneities inside the electrode microstructure contributes to microstructure failure and electrode degradation, which macro-homogeneous models fail to capture. For instance, Wu *et al.* [135] simulated the diffusion induced stress in a 3D reconstructed structure of $LiNi_{0.33}Mn_{0.33}Co_{0.33}O_2$ electrode. They showed that the stress is much higher around the concave regions within the electrode's microstructure than that of smooth homogenous regions due to high local lithium concentrations. Since the stress is higher close to these heterogeneous regions, the mechanical failure could initiate at these areas. Similar results were obtained for $LiCoO_2$ and graphite particles by Lim *et al.* [68] and $LiMn_2O_4$ electrode by Kashkooli *et al.*[14], showing higher stresses around concave heterogeneous regions. The modeling approach based on 3D reconstruction, considers the inherent heterogeneous structure of the electrode which makes it an invaluable tool for degradation studies to visualize the real spatial distribution of properties.

To capture the real spatial distribution of these properties, galvanostatic discharge performance of a LTO half-cell is simulated using the model presented in section 3.2. The model geometry used is the RVE as shown in **Fig. 5-4**, which is extracted from the 3D Zernike phase contrast reconstruction. The model parameters, operational conditions, and material properties are listed in **Table 5-5**. **Fig. 5-8** shows the galvanostatic discharge performance simulated at different C-rates (solid line). The experimental data obtained from coin half-cell galvanostatically discharged at various C-rates are also shown in **Fig. 5-8** (dotted line). Model-experimental comparison confirms the model's ability to predict discharge performance of the

cell at various rates. The model adjustable parameters including diffusion coefficient, D_{LTO}, reaction rate constant, k_0, electrical conductivity of solid matrix, σ, and electrolyte resistance, R_2, are determined by fitting the model results to experimental data at a low-rate [11,32]. The discharge performance at C-rate=0.2 was chosen as the basis to evaluate adjustable parameters. The values of 1×10^{-15} m^2/s, 1×10^{-10} $mol\ m^{-2}s^{-1}(mol\ m^{-3})^{-1.5}$, 0.2 S/m, $2.5 \times 10^{-3} \Omega m^2$ for $D_{LTO}, k_0, \sigma, R_2$ provided the best model-experiment fit and were utilized for the C-rates>0.1 up to 5 to predict the discharge performance. The open circuit potential, U, of the half-cell was obtained by discharging a fully charged half-cell at very low rate (C/50).

Table 5s-6. The list of model parameters.

Parameter	Description	Value
A	Area of the electrode	0.9698 cm^2
L	Electrode thickness	50 μm
ε	Electrode porosity	0.57
D_{LTO}	Solid state diffusion coefficient of LTO	1×10^{-15} m^2/s
σ	Electrical conductivity of solid matrix	0.2 S/m
k_0	Reaction rate constant	1×10^{-10} $mol\ m^{-2}s^{-1}(mol\ m^{-3})^{-1.5}$
α_a	Anodic transfer coefficient	0.5 [34]
α_c	Cathodic transfer coefficient	0.5 [34]
i_f	Exchange current density of lithium foil	19 A/m^2 [34]
c_{ini}	Initial $LiPF_6$ concentration inside electrolyte	1000 mol/m^3
c_{max}	Maximum Lithium concentration in the LTO particles	22741 mol/m^3 [157]
t_+^0	Lithium-ion transference number	0.363 [34]
R_2	Electrolyte resistance	$2.5 \times 10^{-3} \Omega m^2$
T	Cell Temperature	298 K

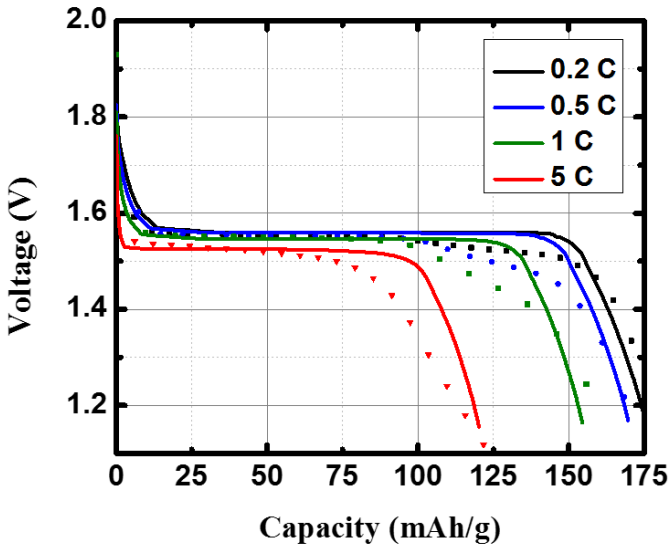

Figure 5-8. Comparison of the modeling (lines) and experimental coin half-cell (dots) results obtained with the LTO electrode at various C rates.

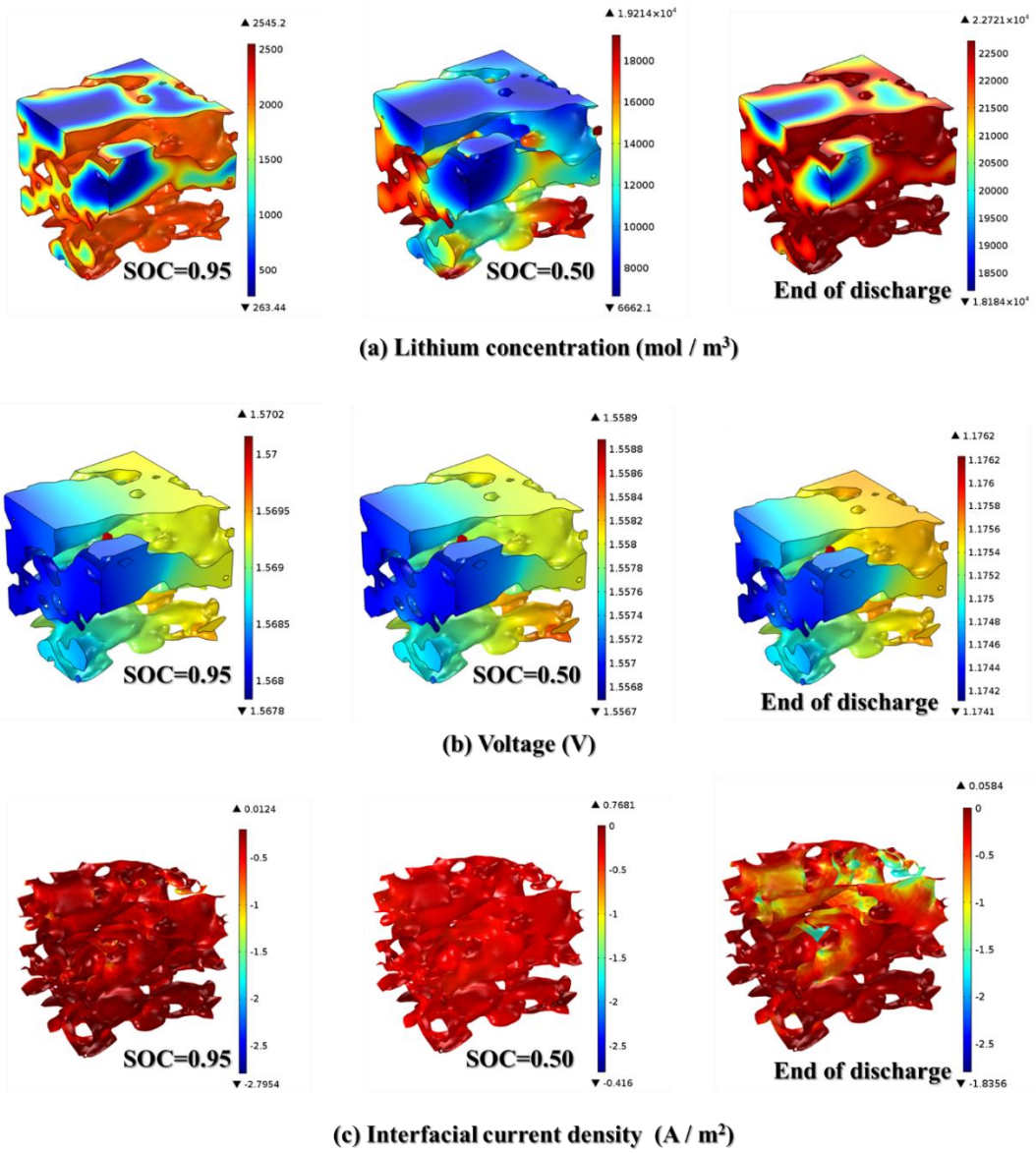

Figure 5-9. Distribution of physical and electrochemical properties in the RVE shown in Fig. 5-4 at various states of charge during galvanastatic discharge at 1 C.

The physical and electrochemical property distribution in the electrode's solid domain at different state of charges (SOCs) during the galvanostatic discharge at 1 C are shown in **Fig. 5-9**. The SOC is defined as the ratio of remaining discharge time to the time when the

end of discharge happens. The end of discharge is reached when the half-cell voltage drops to 1V. In the present model, lithium can diffuse inside the RVE at the solid/electrolyte interface and is free to diffuse between the neighboring particles. **Fig. 5-9a** shows that the lithium concentration of smaller particles/microstructures is higher due to higher surface area available for lithium transport specifically in the sandglass type structure with smaller cross section area perpendicular to lithium transport path. Similar behavior in the previous heterogeneous electrode studies were reported [10,11,66]. **Fig. 5-9b** shows the voltage variation in the LTO solid phase is very small confirming that nano-structuring and conductive Super P addition provided the high electronic conductivity. The voltage increases from current collector to the symmetry boundary no more than 3 mV. Based on the Butler-Volmer kinetics, **Eq. (5-15)**, the local interfacial current density is estimated and shown in **Fig. 5-9c**. The current density also shows small variation within the electrode's solid phase. **Fig. 5-9** shows an inhomogeneous distribution of lithium, and almost homogeneous distribution of voltage and interfacial current density during discharge at C-rate=1.

Structural heterogeneity is known to have greater influence physical and electrochemical processes when discharged at higher rates [66,158]. In order to further investigate the electrode heterogeneity, a discharge process at C-rate=5 was simulated. The lithium concentration, solid phase voltage, and interfacial current density results at C-rate=5 are shown in **Fig. 5-10**. It is clearly seen that higher discharge rate leads to higher lithium mass transport flux which results in larger lithium concentration inside the RVE (see **Fig. 5-10a**). As expected, the simulation results show higher inhomogeneity inside the electrode structure at C-rate=5 compared to C-rate=1. The electrode heterogeneity is more clearly

observed by comparing the range of lithium concentration resulting from high and low rates (5 and 1 C, respectively) as shown in **Table 5-6**. The range of lithium concentration is significantly larger at 5 C than at 1 C. In addition, local solid phase voltage and interfacial current density are shown in **Figs. 5-10b**, and **5-10c**, respectively, which are also shown to be greatly influenced at higher rates. At C-rate=5, the voltage range reaches up to 12 mV, which is 4 times higher than 3 mV obtained at C-rate=1. The interfacial current density also distributes over a wider range at C-rates=5 compared to C-rate=1. The maximum range becomes around 8 A / m^2 at C-rate=5 which is higher than 2.8 A / m^2 achieved at C-rate=1. The histograms showing the electrode's physical and electrochemical properties at various SOCs at C-rate=5 are presented in **Fig. 5-11**. The distribution of the properties does not follow any particular trend. The Macro-homogeneous models typically assume uniform distribution of the current density on the active material particles, however, in a realistic electrode, the current density distributes over a range due to heterogeneities.

Table 5-7. Lithium concentrations obtained at different SOC when galvanostatically discharged at 1 and 5 C (unit: mol / m^3)

C-rate	SOC=0.95	SOC=0.50	End of discharge
1	2282	12552	4536
5	19000	18400	16600

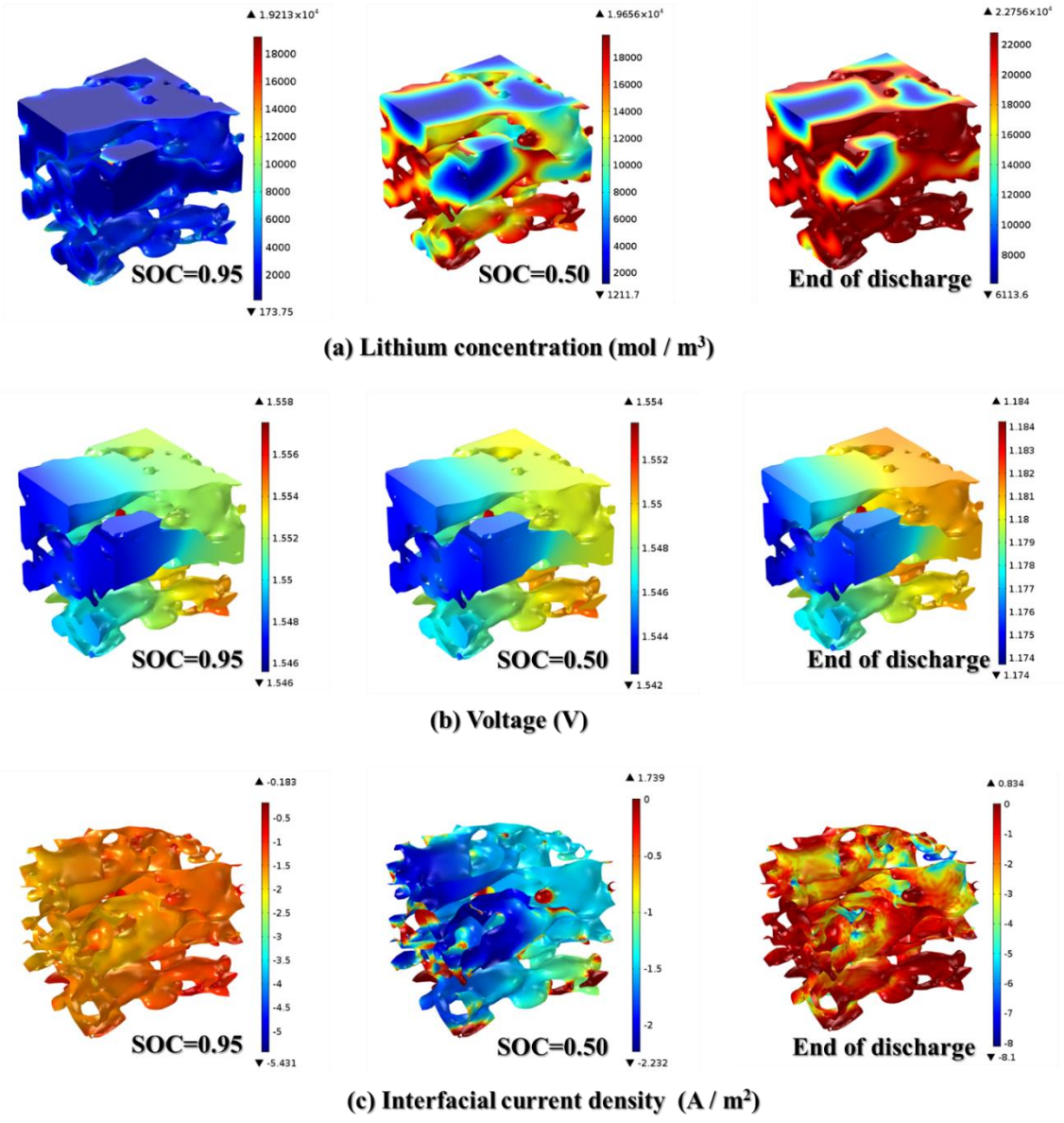

Figure 5-10. Distribution of physical and electrochemical properties in the RVE shown in Figure 5-4 at various states of charge during galvanastatic discharge at 5 C.

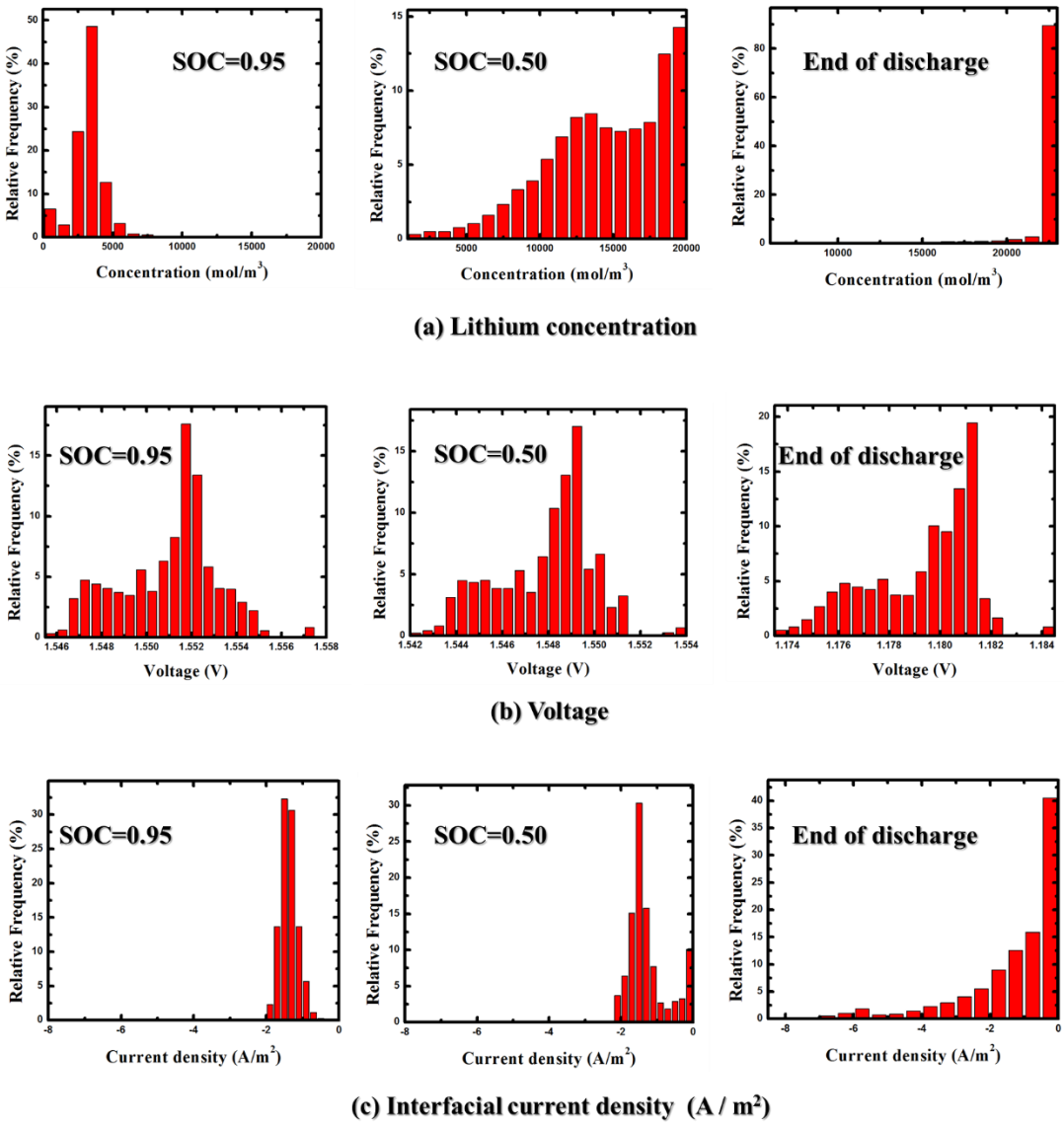

Figure 5-11. Histograms representing the distribution of physical and electrochemical properties in the RVE shown in Fig. 3 at various states of charge during galvanastatic discharge at 5 C.

5.5 Conclusions

The first 3D microstructural study of the LTO electrode based on multiple imaging mode synchrotron nano XCT was accomplished. The synchrotron with a 58 nm resolution was used to reconstruct 3D microstructure of the electrode, which was then characterized for its geometrical and electrochemical properties. The imaging was conducted using two different modes, absorption contrast and Zernike phase contrast, to resolve the electrode's active material, CBD, and pore phases in different ways. The 3D image has revealed that some primary LTO nano-particles tend to agglomerate and form secondary micro-sized particles. Four secondary particles have been selected and their size, volume specific surface area, and degree of non-sphericity have been quantified for simulation. The secondary particles have shown different volume specific surface area ranging from 3.14 to 3.62 (μm^{-1}) and various degree of sphericity from 0.71 to 0.91. The electrode's resistance to charge and mass transport have been quantified by estimating solid and pore domain tortuosities using two methods: 1) simulation based on mass transport analogy and 2) pure geometry. The resulting tortuosities have shown that the commonly used Bruggeman relation for macro-homogeneous models is a poor estimator of the electrode tortuosity, for instance pore domain in-plane and through plane tortuosities have been estimated as 1.46, 1.69, and 2.07 which are higher than the 1.32 of the Bruggeman one. In addition, tortuosities, obtained from both methods, vary significantly depending on the directions, confirming highly anisotropic and heterogeneous nature of pore and solid domains. To further investigate the microstructural heterogeneity, a computational framework has been developed to simulate electrochemical performance of the

LTO electrode. Unlike commonly used absorption contrast 3D structure, the current model took advantage of Zernike phase contrast reconstructed geometry. The lack of CBD in absorption contrast results in isolated active material particles, whereas Zernike phase contrast provides an integrated percolated network of active material and CBD together, making it suitable for FEM simulation. The model was an improvement over our previous RVE model as it now includes electron transport to the governing equations as well as lithium diffusion within solid. The model has been validated with the experimental data obtained from a coin half-cell performance. The simulation results have revealed irregular and non-uniform distribution of physical and electrochemical properties within the solid domain, which is attributed to the electrode's structural heterogeneity, which causes non-homogeneous mass and charge transport within the electrode structure. Structural heterogeneities have led to the wider distribution of properties at higher rates. Notably, the range of lithium concentration within solid domain at the end of discharge was reached 16,600 mol/m^3at C-rate=5, which is significantly higher than that of 4,536 mol/m^3 at C-rate=1.

6. Synchrotron X-ray nano computed tomography based simulation of stress evolution in $LiMn_2O_4$ electrodes

This chapter is reprinted in adopted form with permission from Electrochimica Acta:

A. G. Kashkooli, E. Foreman, S. Farhad, D. U. Lee, W. Ahn, K. Feng, V. D. Andrade, Z. Chen, Synchrotron X-ray nano computed tomography based simulation of stress evolution in $LiMn_2O_4$ electrodes, Electrochimcia Acta, 2017, 247, 1103–1116.

6.1 Introduction

As highlighted in previous chapters, the lithium-ion battery (LIB) technology is currently the primary energy storage choice for electric and hybrid electric vehicles due to several key advantages, including high energy density, power density, and long cycle life [159–161]. However, continued research efforts and systematic investigations are required to further improve the performance and life-time of LIBs to ultimately achieve larger scale automotive electrification [21,162,163]. As LIBs generally experience a large number of charge-discharge cycles, performance gradually decreases over the course of battery life-time via various degradation mechanisms. Notably, the capacity fade of LIBs are mainly ascribed to structural failure of electrodes [164,165], decomposition of the electrolyte [166,167], and parasitic reactions [168,169] that occur during battery cycling.

To investigate structural degradation mechanisms of LIB electrodes, many studies have been conducted in the past utilizing a single active material particle. For instance, the Newman group was the first to develop a mathematical model to calculate the diffusion-induced stress

inside a spherical particle of LIB electrodes. They showed that the failure of $LiMn_2O_4$ (LMO) electrodes occurs during common high power applications due to the phase change along the 3V plateau [170,171]. The Sastry group, on the other hand, showed investigation of different particles sizes and morphologies, ranging from one-dimensional spherical particles to three-dimensional ellipsoidal particles using their stress modeling framework, suggesting that ellipsoidal particles with a high aspect ratio reduces diffusion-induced stresses inside a particle [90,172,173]. At the electrode-level, Garcia *et al.* developed a framework to couple electrochemistry of porous electrodes with mechanical stresses inside them, and employed it to investigate cell performance of different arrangements consisting of two-dimensional spherical particles [174]. Likewise, the White group investigated stresses inside LIB electrodes using the Newman pseudo-2D model which consisted of a blend of LMO and $LiNi_{0.8}Co_{0.15}Al_{0.05}O_2$ (NCA) active materials [31,52], showing that stresses are generated due to the change in the lattice volume and phase transformations during battery cycling [175,176]. Lastly, Barai *et al.* conducted a stochastic analysis to investigate stress-induced damage inside LIB electrodes, generating phase-maps to show safe/unsafe operating conditions for various particle sizes such as C rates, and voltage window [177].

Despite the efforts mentioned above, most of the electrode structure investigations are still based on simple particle geometries such as spheres, ellipsoids, and combination of the two in various arrangements [31,52,90,170–177]. However, the real three-dimensional structure of active materials in LIB electrodes is very different from those simplified for the purpose of conducting simulations. Taking into the consideration of the real morphology of active particles is the pivotal step in truly understanding mechanisms behind the stresses in

LIB electrodes since they directly affect the distribution of stress and ultimately determine the active material failure. Recent advances in X-ray computed tomography (XCT) [10,154,178], and focused ion beam-scanning electron microscopy (FIB-SEM) [178–180] have allowed the reconstruction of three-dimensional active particles in the electrode. First, Lim *et al.* [68] has demonstrated the calculation of diffusion-induced stresses in three-dimensional electrode particles that were reconstructed by XCT. They have shown that the real particles exhibit convex and concave surfaces that lead to the generation of stresses in concave regions that are several times higher than those obtained from a spherical model of the same volume. Malve *et al.* [181], on the other hand, has demonstrated simulations of stresses in real electrode microstructures using FIB-SEM, also noting that much greater stresses are observed near small protuberances and notch-like concave features. Mendoza *et al.* [182] has also developed mechanical and electrochemical frameworks based on FIB-SEM reconstructed electrodes, simulating stress build-ups in the electrode microstructures during the charging. Similarly, Wu *et al.* [135] simulated stresses generated by phase transition and lithium intercalation in nickel-manganese-cobalt (NMC) electrode microstructures that were reconstructed by synchrotron XCT, also observing high stresses in the concave regions of electrode structures.

Despite taking into the consideration of stresses generated inside real electrode structures, the above investigations still neglect the effect of the presence of carbon doped-binder domain (CBD) [68,181], or considers it to be merged with the electrolyte phase [135,182]. However, recent experimental and modeling studies have revealed that stresses generated in the CBD and its mechanical failure could lead to detrimental capacity fade of LIBs [182–186]. As LIB is cycled, lithium-ions are intercalated into and de-intercalated from

the active material causing it to swell and contract, respectively, except in case of $LiCoO_2$. Therefore, any CBD attached to the active electrode particles experiences mechanical stresses due to the changes in the volume during lithiation and de-lithiation. This is because CBD provides not only electrical connectivity, but also mechanical support particularly for active particles with non-idealized shapes by re-distributing stresses to prevent them from detaching. Therefore, CBD must be given as much consideration as active material particles to accurately model mechanical stresses that lead to changes in the microstructures and eventual failure of LIB electrodes.

Based on the reports in the literature, the CBD is generally incorporated into the electrode models in three ways: 1) a continuous layer of CBD encloses individual particles [185,187]; 2) a continuous CBD bridges (interconnects) particles [188,189]; 3) a continuous layer of CBD covers the outer boundary of bi-continuous percolated network of particles [182,190]. Rahani *et al.* [187] investigated for the first time the role of CBD, comparing the results obtained using the first and second models above using a graphite electrode to show that both models sufficiently demonstrate the real stresses in the electrode. Takahashi *et al.* [185] also investigated degradation modes of graphite electrodes using the first model, highlighting that rather than the particles themselves, but the mechanical properties of CBD determines the electrode failure. In other studies, Rieger *et al.* [188] employed the second bridge model with different thicknesses and widths in the in-plane and diagonal directions to simulate the strain propagation during battery cycling, while Wu *et al.* [190] utilized the third model to show that CBDs with lower Young's modulus and larger elongation endure lower

stress compared to the one with higher modulus provided that they have the same ratio of the adhesion strength to the CBD strength.

In this study, the diffusion-induced stress and possible mechanical damages in a commercial LMO electrode has been investigated utilizing the real electrode morphology obtained by employing synchrotron transmission X-ray microscopy (TXM) at the Advanced Photon Source (APS) of the Argonne National Laboratory (ANL). The three-dimensional morphology of the active particles is reconstructed based on the stack of two-dimensionally projected images using a commercial software Simpleware 7. Additionally, to accurately study the stresses and the failure of the electrodes, neighboring CBD has been taken into the consideration using imaging processing techniques as a continuous layer covering the active particles (the first model mentioned above).

The diffusion-induced stress in the electrode structure is simulated under galvanostatic discharging conditions on four real particles and their enclosing CBD. Using this model, a more accurate distribution of stress in the electrode microstructures has been calculated, which allows the prediction of mechanical failures of the active materials and the CBD at various C rates. Although our results are based on LMO electrodes, the modeling approach and observations can be applied to other LIB electrode active materials. This chapter is organized as follows: first, the experimental method used to obtain the reconstructed particles is described. Then, the modeling development including CBD addition to the particles, followed by the governing equations used to model stress inside the active material and CBD are presented. Finally, the simulation results are presented and discussed with concluding remarks.

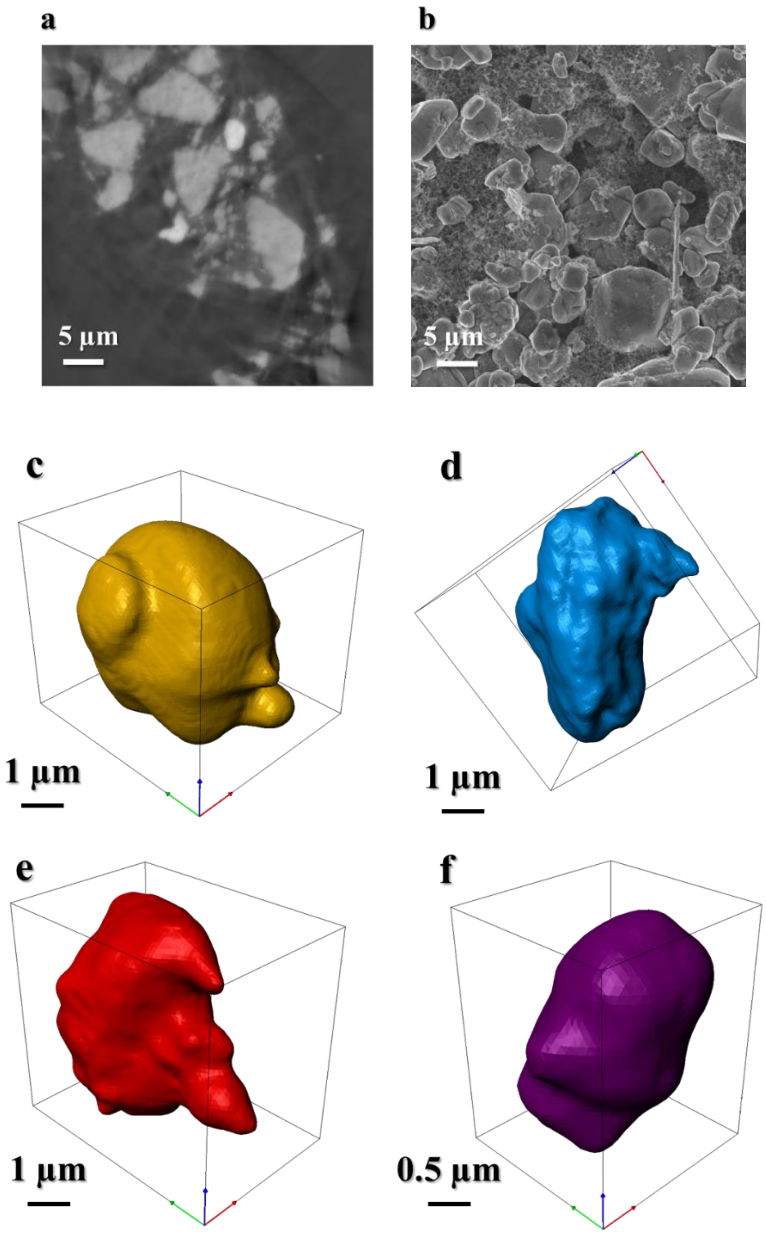

Figure 6-1. 2D Morphology of a commercial LMO electrode obtained from (a) synchrotron TXM imaging, and (b) SEM imaging, reconstructed three-dimensional particles of LMO electrode from synchrotron TXM imaging (c) particle (1), (d) particle (2), (e) particle (3), (f) particle (4).

6.2 Experimental methods

In order to obtain the electrode active material particles, a commercial LMO positive electrode was purchased and a small piece was cut for imaging purposes. Because the aluminum current collector affects the TXM, it was removed by soaking in 6 M KOH solution for 5 min [11]. A synchrotron TXM in sector 32-ID-C at APS in ANL was utilized to obtain the microstructures of the LMO electrode. The 2D tomograms were obtained in the absorption contrast mode employing a high energy 8 keV monochromatic beam. The tomographic images were obtained by rotating the sample 180° at an increment of 0.5° and the exposure time of 1 second at each step. The 3D reconstruction was performed with Tomopy, a python based platform for the synchrotron data analysis [125,126]. The reconstructed volume represents voxel of attenuation coefficient with a width of 54 nm after binning. A raw 2D projection of LMO particles obtained from the synchrotron TXM is shown in **Fig. 6-1a**. The carbon black and binder phases could not be captured by synchrotron TXM in absorption contrast mode. Therefore, the white region in **Fig. 6-1a** represents LMO active material particles and black region is the pore plus CBD. Fig. **6-1b** shows an SEM image of the electrode sample presenting similar morphology to TXM image with particles exhibiting irregular shapes and geometries, and sizes ranging from 1 to 5 μm.

For three-dimensional reconstruction, the stack of 2D images were imported to the ScanIP. The segmentation of grayscale 2D images were obtained using binary thresholding algorithm function in ScanIP. XCT usually captures a cluster of particles, nevertheless, we could isolate four well-resolved particles with different morphologies and sizes. As seen from **Fig. 6-1 (c-**

f), the reconstructed particles are non-spherical with complex convex and concave surface topology. To measure the degree of particle's non-sphericity, the particle sphericity factor was calculated. Similar to ref. [134], the particle sphericity is determined by comparing each particle's surface area to the surface area of a sphere with the same volume, where sphericity of unity corresponds to a perfect sphere and lower values indicate increased degree of non-sphericity. The particle surface area was calculated using "surface area" and "volume" function within ScanIP's quick general statistics pane. **Table 6-1** shows the microstructural information of the particles shown in **Fig. 6-1 (c-f**). We calculated the reaction rate current density corresponding to 1 C rate from each particle's surface area, volume, density of LMO, and practical capacity of 148 mAh g^{-1}.

Table 6-1. Microstructural information for the three isolated particles from LMO commercial electrode imaged using synchrotron TXM and the calculated current densities corresponding to 1 C rate.

Particle	Sphericity	Surface Area (μm^2)	Volume (μm^3)	1 C rate (A m^{-2})	Outline cube dimensions (μm)
a	0.93	79.22	59.75	0.46	$5.01 \times 5.62 \times 4.83$
b	0.82	60.89	33.10	0.33	$3.51 \times 5.07 \times 4.51$
c	0.80	50.94	24.67	0.29	$3.51 \times 5.07 \times 4.51$
d	0.90	14.18	4.326	0.18	$2.12 \times 2.26 \times 2.73$

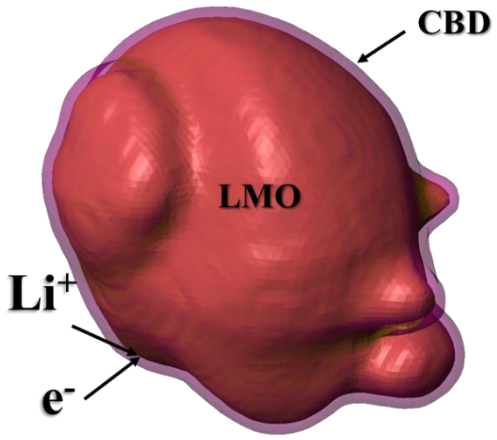

Figure 6-2. Schematic illustration of the model used in this study. The active material particle is covered with a uniform layer of CBD. Charge (electron) and Li-ion transport occur at active material particle/CBD interface.

6.3 Model Development

In order to study the development of stress in electrodes, we calculated the stress generated inside the four reconstructed electrode particles, see **Fig. 6-1 (c-f)**, enclosed in a uniformly thick layer of CBD. Although CBD can be identified with a combination of absorption contrast and phase contrast imaging modes [98], it is very challenging to use the resolved CBD for the simulation purposes. The reason being the resulting CBD is likely to be a non-continuum, segregated domains comprising multiple island-like structures which are not suitable for finite element simulations. Instead, we assumed that the active material particles are covered with a uniformly thick layer of CBD which completely wraps the outer surface of each particle as shown in **Fig. 6-2**. To form this layer of CBD, we performed a morphological dilation command on the active material domain with growing pixels equal to 2 (each pixel equals to

54 nm which is the resolution of the TXM utilized). Dilation is a morphological image processing feature available in ScanIP which enabled the growth of selected domains with a chosen pixel value. Then, we subtracted the active material domain from that of the grown one. This created a uniform CBD with the thickness of 108 nm around the particles. Similar CBD modeling approach have been previously used for spherical particles [185,187,191]. However, the spherical particles do not allow modeling of the tangential stress at the interface of active material and the CBD due to the delamination of the CBD layer [185]. Using FIB-SEM, Mendoza *et al.* [182] reconstructed the percolated network of electrode active materials without a CBD. To model a CBD, they shrank the size of their original structure by 100 nm and replaced the shrunk layer with a uniform CBD. Even though the CBD was incorporated in the electrode structure, their method reduced the total volume ratio of active material particles to the total electrode solid network.

In this study, lithium-ion transport inside active material particles is modeled by two coupled partial differential equations. These equations comprise the diffusion equation with the hydrostatic stress term, and the stress-strain relation with the embedded lithium-ion concentration. The diffusion of lithium-ions inside active material particles is governed by [68,170,172,176]:

$$\frac{\partial c}{\partial t} = \nabla . D\left(\nabla c - \frac{\Omega c}{RT}\nabla \sigma_h\right) \tag{6-1}$$

where c is the concentration of lithium-ions inside particle, D is diffusion coefficient, R is universal gas constant, T is temperature, Ω is partial molar volume of the active material, and σ_h is the hydrostatic stress which is calculated from stress domain as $\sigma_h = \sigma_{ii}/3$ (σ_{ii} are

diagonal elements of stress tensor). The boundary condition of the **Eq. (6-1)** on the particle's surface is expressed as:

$$-D\left(\nabla c - \frac{\Omega c}{RT}\nabla\sigma_h\right) = \frac{i_n}{F} \tag{6-2}$$

where i_n is the current density on the particle's surface and F is Faraday's constant. We have employed a linear elastic stress-strain relation to model the stress development in the electrode as this has been previously reported to be a suitable assumption [182,188]. For detailed studies on stress and failure predictions in CBD, its plastic deformation needs to be considered [187,190]. The stress-strain relation in the active material particle is calculated as analogous to thermal stress where the temperature gradient is replaced with the concentration gradient [68,172,176] as:

$$\varepsilon_{ij} = \frac{1}{E}\left[(1+\nu)\sigma_{ij} - \nu\sigma_{kk}\delta_{ij}\right] + \frac{\tilde{c}\Omega}{3}\,\delta_{ij} \tag{6-3}$$

where ε_{ij} are the strain components, σ_{ij} are the stress components, E is Young's modulus, ν is Poisson's ratio, δ_{ij} is the kronecker delta, and $\tilde{c} = (c - c_0)$ is the concentration change in lithium-ions from the original condition. Then, **Eq. (6-3)** is rearranged to obtain the relationship for the stress components as the following [172]:

$$\sigma_{ij} = 2\mu\varepsilon_{ij} + (\lambda\varepsilon_{kk} - \beta\tilde{c})\delta_{ij} \tag{6-4}$$

where $\mu = \frac{E}{2(1+\nu)}$, $\lambda = \frac{2\nu\mu}{1-2\nu}$, and $\beta = \frac{\Omega(3\lambda+2\mu)}{3}$. The strain tensor is related to the displacement vector as [172]:

$$\varepsilon_{ij} = \frac{1}{2}\left(\frac{\partial u_i}{\partial x_j} + \frac{\partial u_j}{\partial x_i}\right) \tag{6-5}$$

Under the quasi-static condition, mechanical deformation of the particle is governed by [172]:

$$\sigma_{ij,i} = 0 \tag{6-6}$$

Substituting **Eq. (6-4)** and **(6-5)** into **Eq. (6-6)** leads to the equation for the displacement *u* as [172]:

$$\mu\nabla^2 u_i + (\lambda + \mu)u_{k,ki} - \beta\tilde{c}_{,i} = 0 \tag{6-7}$$

For the interfacial boundary condition between the particle's core and the surrounding shell, Takahashi *et al.* [185] has previously assumed the radial stress to be continuous between the spherical particle core and CBD shell, whereas Hao *et al.* [191] considered the continuous radial displacement across the interface of a manganese oxide core and carbon shell suggesting that there is a mathematical discontinuity in the radial stress when crossing the interface. Here, similar to ref. [46], we assume that LMO particle and CBD domains are perfectly bonded together and the displacement vector is continuous across the interface. This condition can be expressed as:

$$u_{i,1}\big|_s = u_{i,2}\big|_s \tag{6-8}$$

where subscripts 1 and 2 denote active material domain and CBD, respectively and s represents the interface.

In the present work, the lithium-ion diffusion, **Eq. (6-2),** is only solved within the active material particles, whereas the mechanical stress is modeled for both active materials and CBD. The stress-strain governing equations for the CBD are similar to the active material particle, except the absence of the terms related to the diffusion-induced stress. The governing

equations within the CBD can be simply obtained by applying $\tilde{c} = 0$ into **Eq. (6-3) to (6-7)**, which are not shown here due to their similarity to those of the active material particle. In this study, due to the high porosity of the electrode, we assume that the mechanical interaction among neighboring LMO particles are negligible, see **Fig. 6-1 (a-b).** Therefore, at the outer surface of the CBD, the traction free boundary condition is assumed. The traction free boundary condition specifies that there is no external force on the CBD outer surface. This condition can be expressed as [172]:

$$\sigma_{xx}ll + \sigma_{yx}mm + \sigma_{zx}nn = 0 \tag{6-9a}$$

$$\sigma_{xy}ll + \sigma_{yy}mm + \sigma_{zy}nn = 0 \tag{6-9b}$$

$$\sigma_{xz}ll + \sigma_{yz}mm + \sigma_{zz}nn = 0 \tag{6-9c}$$

where *ll*, *mm*, *nn* are direction cosines between the external normal vector to the outer surface and each coordinate axis.

In this study, the active material is assumed to be isotropic which experiences volume expansion during discharge from $Li_{0.2}MnO_2$ to $Li_{0.995}MnO_2$. Typically, the calculation of the reaction current density, i_n on the particle's surface requires the use of Butler-Volmer equation employing local overpotential and exchange current density. However, we assume that the electrode is sufficiently thin to ensure that the electrolyte concentration does not change significantly on particle's surface, resulting in i_n becoming uniform on the particle's surface. As mentioned above, the 1C current density for each reconstructed particle is presented in **Table 6-1**. Additionally, the structural mechanics and partial differential modules in COMSOL Multiphysics® 5.0 have been employed to simulate the stresses in the active

material particles and the CBD domains. Lastly, the reconstructed particles have been imported from ScanIP as tetrahedral mesh elements in COMSOL for finite element simulation.

Table 6-2. List of parameters used in the simulation.

Parameter	Symbol and unit	LMO	CBD
Young's modulus	E (GPa)	10 [172]	0.2 [187]
Poisson ratio	ν	0.3 [172]	0.34 [185]
Partial molar volume	Ω (m^3 mol^{-3})	3.497×10^{-6}[172]	-
Maximum concentration	C_{max} (m^3 mol^{-3})	2.29×10^4 [192]	-
Diffusion coefficient	D (m^2 s^{-1})	7.08×10^{-15} [192]	-
Density	ρ (kg m^{-3})	4140 [193]	1780 [185]

6.4 Results and discussion

The mathematical model presented in the previous section is used to simulate the diffusion-induced stress within the reconstructed active material particles shown in **Fig. 6-1 (c-f)** surrounded by a uniform layer of CBD with the thickness 108 nm. The simulation has been performed in galvanostatic mode using the parameters listed in **Table 6-2**. The LMO particles were discharged at different C rates from SOC of 0.20 to 0.95, where we have defined SOC as the ratio of average concentration of lithium-ions in the particle to its maximum possible concentration as shown in **Table 6-2**. Although this simulation has been conducted using active material particles in a LMO electrode, our modeling approach and discussions are

applicable to other electrode materials. Von-Mises stress is commonly used to present stress inside 3D reconstructed particles [68,135,182]. However, the failure of brittle materials, including LMO, is typically related to the tensile stress rather than Von-Mises stress [173,194]. Therefore, tensile stress has been chosen to present stress within active material particles which could predict crack initiation and growth in active material particles [190]. In order to obtain the maximum tensile stress generated during discharge, we have calculated three principal stresses σ_1, σ_2, and σ_3 inside the LMO particles. The local maximum tensile strength is represented as σ_1, and the rest in the descending order (σ_3 being the smallest).

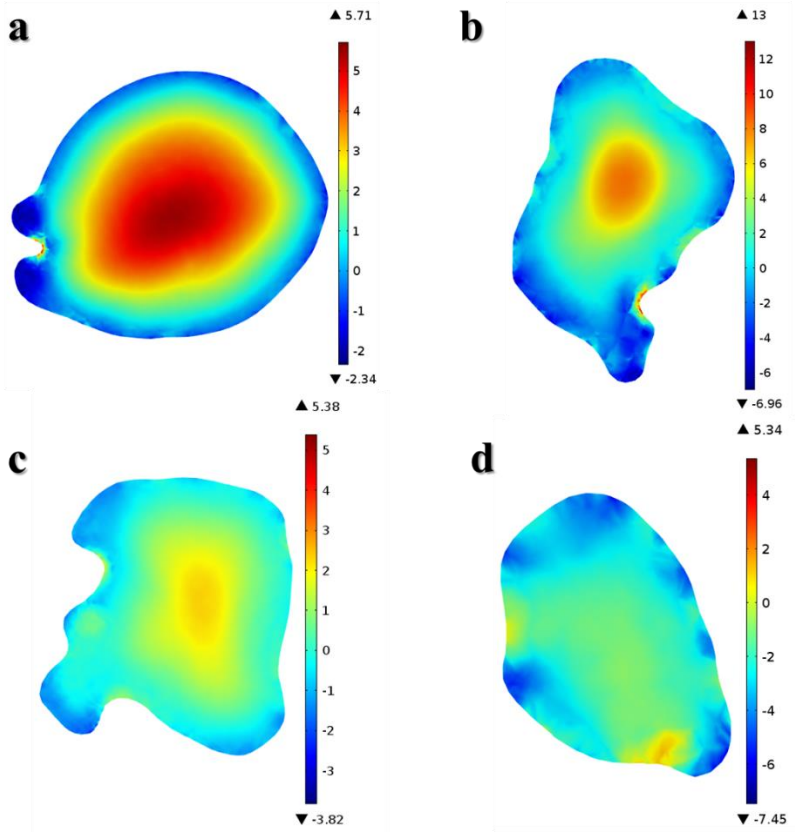

Figure 6-3. Maximum tensile stress (MPa) distribution within LMO particles enclosed with a uniform layer of CBD at the end of discharge at 1C, a) particle (1), b) particle (2), c) particle (3), and d) particle (4).

Fig. 6-3 shows 2D cross-sectional distribution of maximum tensile stress inside the LMO particles enclosed with a uniform layer of CBD at the end of discharge at 1C where the stress reaches its maximum value. The CBD's stress distribution is not shown in this figure due to its higher range of values and will be discussed later. However, CBD is considered in the model geometry for **Fig. 6-3** and all results presented in this chapter unless clearly stated otherwise. As shown in **Fig. 6-3**, a high level of maximum tensile stress occurs in two regions: 1) vicinity of the particle's center (bulk stress) or 2) concave area on the particle's surface

where there is a stress concentration (surface stress). The evolution of stress in these regions is investigated separately since the former is related to the particle's bulk behavior, while the latter is related to the particle's non-uniform surface morphology. In case of bulk behavior, the stress reaches its maximum near the particle's center and decreases towards the particle's surface. The lithium concentration changes from lower values at the particle's center to higher values at the surface of the particle. Therefore, the area close to the particle's surface expands more due to the lithium intercalation process, resulting in the center of the particles being under tension, while the outer being under compression. The positive and negative values correspond to tensile and compressive stresses, respectively. Hao *et al.* [191] showed similar behavior for a spherical LMO core enclosed with a carbon shell.

To further elaborate the CBD inclusion effects, the stress simulation without considering the CBD in the model geometry is also conducted and the calculated stress is used for comparison. When modeled without considering the surrounding CBD, the results show either much lower or higher bulk stress depending on the particle morphology and size. Specifically, the maximum tensile stress in vicinity of particle's center in particle (1) is 5.7 MPa with CBD compared to 6.1 MPa without CBD. Similarly, the stresses in particle (2), (3), and (4) with CBD are 13.3, 5.4, and 5.3 MPa with CBD, respectively, compared to 3.8, 3.4, and 1.1 MPa without CBD, respectively. These results are indicative of the presence of CBD limiting the displacement of the active material particle, which is modeled in this study by changing the traction free boundary condition to the continuous displacement on the particle's surface. This leads to either higher or lower values of tensile stress within particles depending on particle morphology and size.

The diffusion-induced stress depends on particle size, morphology, materials properties [68], and presence of surrounding CBD. For example, the lower values of stress are observed in smaller particles due to their relatively high surface to the volume ratio. This leads lower intercalation reaction rates on the particle's surface thereby resulting in relatively low diffusion-induced stress in the particle [68]. The higher diffusion-induced stress observed within particle (2) compared to that of particle (1), despite particle (2) having a larger surface to volume ratio, is attributed to diffusion-induced the presence of CBD in the model, and its effects on the irregular morphology of particle (2). When modeled without CBD, particle (1) demonstrates higher diffusion-induced stress than that of (2). These opposing results highlight the fact that the inclusion of CBD in the model properly takes into the consideration of the morphological effect of active material particles, such as those with multiple surface irregularities (particle (2)).

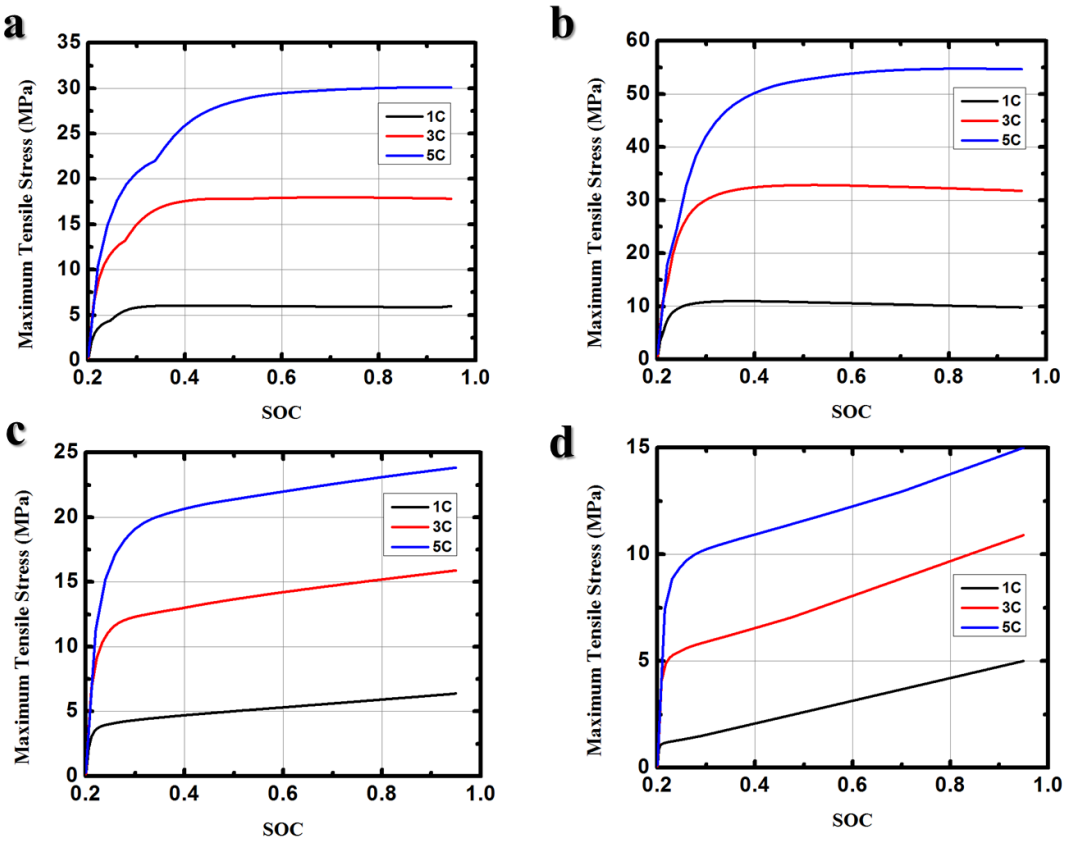

Figure 6-4. Maximum tensile stress (bulk stress) inside the reconstructed LMO particles enclosed with a uniform layer of CBD galvanostatically discharged at various C rates (1, 3, 5 C) from SOC=0.2 to SOC=0.95. a) particle (1), b) particle (2), c) particle (3), and d) particle (4).

Fig. 6-4 shows the evolution of the maximum tensile stress (bulk stress) in the reconstructed particles enclosed with a uniform layer of CBD galvanostatically discharged under various C rates. The maximum stress for each particle has been calculated in vicinity of particle's center where the highest bulk maximum tensile stress occurs when discharged at 1C rate. The electrode has been discharged up to the 5 C rate limit as noted by the manufacturer. The results in **Fig. 6-4** highlight increasing diffusion-induced stress with increasing discharge C rate, as expected, due to higher rates of intercalation occurring at the surface. Specifically,

in particle (1), the maximum tensile stress has been measured to be 17.8, and 30.1 MPa at C rate=3, and 5, respectively, which are 3.1 and 5.3 times higher than the maximum stress of 5.7 MPa measured at C rate=1. In particle (2), the maximum stresses measured are 31.8 and 54.7 MPa at C rate=3, and 5, respectively, which are 2.4 and 4.2 times higher than 13.0 MPa measured at C rate=1. In particle (3), the maximum stresses measured are 15.9 and 23.8 MPa at C rate=3, and 5, respectively, which are 2.5 and 3.7 times higher than 6.4 MPa measured at C rate=1. Lastly, in particle (4), the maximum stresses measured are 11.2 and 15.0 MPa at C rate=3, and 5, respectively, which are 2.1 and 2.8 times higher than 5.3 MPa measured at C rate=1. Interestingly, the rate of increase in the maximum stress observed with particle (1) is higher compared to those of other particles, which is attributed to its relatively much lower surface to volume ratio of 1.33 1/μm compared to 1.83, 2.06, and 3.28 1/μm of particles (2), (3), and (4) respectively. The lower surface to volume ratio increases the lithium-ion flux on the particle's surface which in turn increases the stress experienced by the particle.

Notably for particles (1) and (2) at all C rates presented in **Fig 6-4**, the stress is observed to increase rapidly between SOC=0.2 to 0.4 then plateaus to a constant value up to SOC=0.95. For particles (3) and (4), the stress is observed to increase rapidly between SOC=0.2 to 0.3 then linearly increases at a much slower rate up to SOC=0.95 where the maximum value is reached at the end of discharge. The stress plateau in particle (1), (2) and slow linear increase in stress observed with particles (3) and (4) after SOC=0.4 are related to the interaction between lithium diffusion in solid and the diffusion-induced hydrostatic stress [68,172,173]. The diffusion-induced hydrostatic stress increases the lithium diffusion in the active material particles, in accordance with **Eq. (6-1)**, which results in decreasing lithium concentration

gradient inside the particle. Therefore, the diffusion-induced hydrostatic stress results in lower rate of stress generated in the particles. Without including CBD in the model, Lim *et al.* [68] has shown that the stress increases very sharply until reaching the maximum value and then either plateaus at a constant value or decreases due to the diffusion-induced hydrostatic stress. The inclusion of CBD as in our model shows a similar behavior for stress evolution inside particles (1) and (2), while particles (3) and (4) shows reduced effects of hydrostatic-induced stress resulting in a slow linearly increasing stress after SOC=0.4.

Another notable observation is longer duration of rapidly increasing initial stress with increasing C rate. Specifically, particles (1), (2), and (3) exhibit a sharp increase from SOC=0.2 to 0.25 at C rate=1, from SOC=0.2 to 0.3 at C rate=3, and from SOC=0.2 to 0.4 at C rate=5. This is because as C rate increases, the diffusion-induced hydrostatic stress better facilitates the lithium diffusion in the particles even at higher SOCs. For particle (4), however, the rapid increase in stress initially occurs over a relatively shorter range of SOC most likely due to much smaller size of particle (4) compared to the size of other particles. These results are in good agreement with the reports of Chu *et al*. in which they showed under similar galvanostatic testing conditions, range of SOC where the sharp initial increase in stress occurs, increases with bigger particle sizes and with higher C rates [195].

The discussion so far involved high stress values close to the particle's center, which we called bulk stress. However, in **Fig. 6-3**, high values of stress near concave areas on the particle's surface surrounded by CBD were observed. These points of high stress due to surface irregularities can only be captured by including real 3D reconstructed active material particles with surrounding CBD. Reconstructed particles reveal non-uniform surface

morphology with multiple concave and convex areas which are locations of high local stress concentration. **Fig. 6-5** shows the simulation results of tensile stress on the surface of LMO particles at the end of discharge at 1C. On the surface of the particle, the maximum stress always occurs at the concave areas, and convex areas have relatively low stresses. The large curvature in the convex areas tend to result in relatively higher lithium concentration gradient due to the high surface to volume ratio, which leads to higher diffusional stresses in these areas, in accordance with **Eq. (6-3)**.

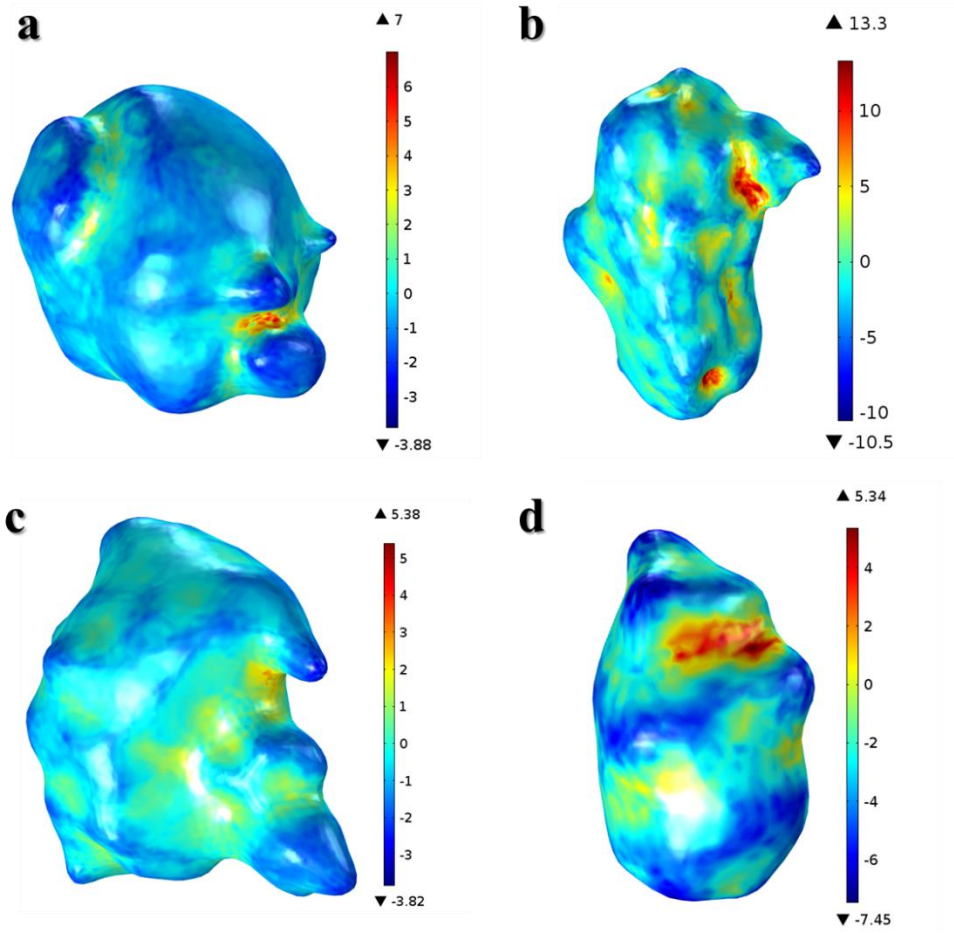

Figure 6-5. Maximum tensile stress (MPa) distribution on the surface of LMO particles enclosed with a uniform layer of CBD at the end of discharge at 1C. a) particle (1), b) particle (2), c) particle (3), and d) particle (4).

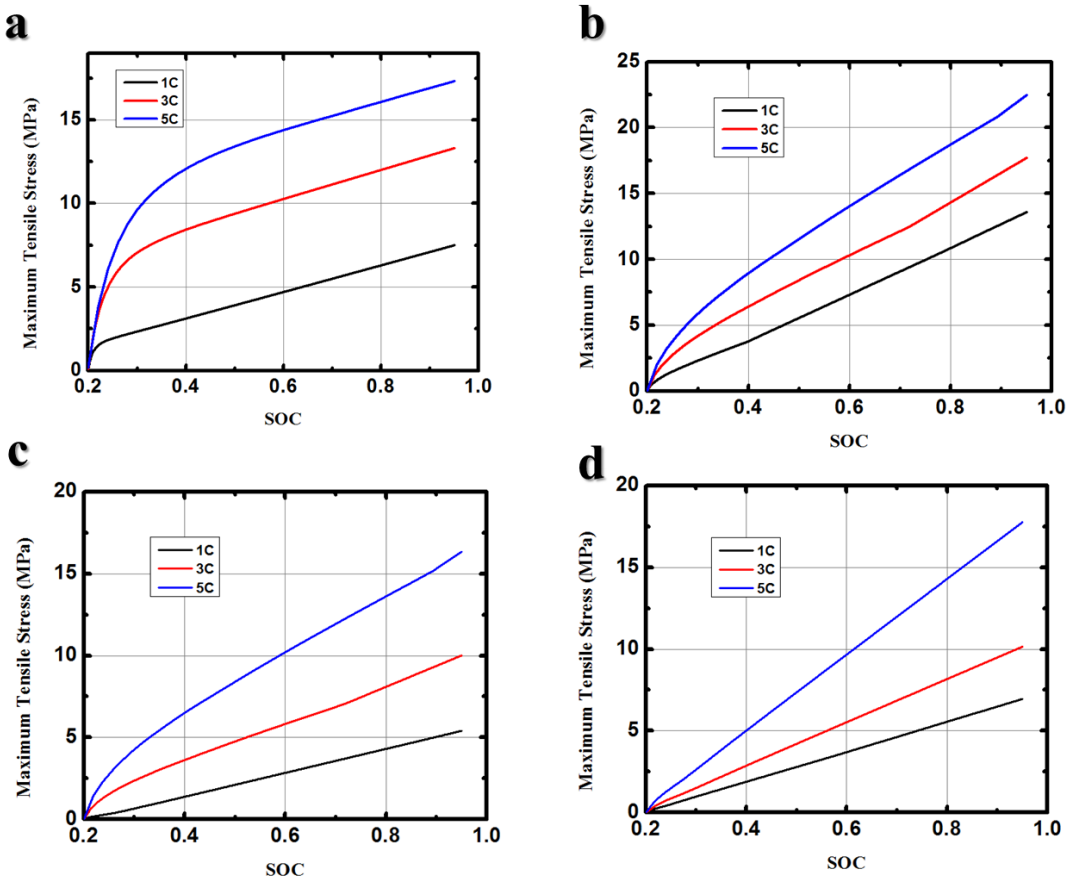

Figure 6-6. Maximum tensile stress on the surface of the reconstructed LMO particles (surface stress) enclosed with a uniform layer of CBD galvanostatically discharged at various C rates (1, 3, 5 C) from SOC=0.2 to SOC=0.95. a) particle (1), b) particle (2), c) particle (3), and d) particle (4).

Fig. 6-6 shows the maximum tensile stress variations on the particle's surface (surface stress) when discharged at different C rates. In all particles, the maximum tensile stress increases as the applied current density increases with the maximum stress occurring at C rate=5. The calculated maximum surface tensile stresses at C rate=1 are 7.5, 13.3, 5.4, and 6.9 MPa for particles (1), (2), (3), and (4), respectively, compared to 6.0, 9.0, 6.3, 5.0 MPa of

maximum bulk stress previously shown in vicinity of particle's center. At C rate=3, the maximum surface tensile stress is 13.3, 17.7, 10.0, and 10.1 MPa for particles (1), (2), (3), and (4), respectively, compared to the maximum bulk stress of 17.8, 31.8, 15.9, and 5.6 MPa. When discharged at C rate=5, the maximum surface tensile stress is 17.3, 22.5, 16.3, and 17.8 MPa for particles (1), (2), (3), and (4), respectively, compared to the maximum bulk stress of 30.1, 54.7, 23.8, and 11.9 MPa. These results show that at C rate=1 for particle (1) and (4) the surface stress is actually higher than the bulk stress which emphasizes the importance of utilizing the real particle surface morphology as the model's geometry. At C rate=3 and 5, for particles (1), (2), (3), the bulk stress is higher than the surface stress, while, the reverse is observed with particle (4), which reiterates the importance of modeling high surface stress in smaller particles.

There is no precise measurement of the tensile strength of lithium manganese oxide currently in the literature. Park *et al.* [196] has assumed the tensile strength of ~100 MPa close to the measured tensile strength of TiO_2. However, based on our simulation, the maximum tensile stress in the reconstructed particles, whether bulk or surface stress, discharged at various C rates are found to be much lower than 100 MPa, confirming that the material failure very unlikely to take place due to intercalation-induced stresses in the LMO particles investigated in the present study. Park *et al.* [173] have shown that the stress level caused by the phase transition from cubic to tetragonal is an order of magnitude higher than the intercalation-induced stress, and that this phase transition would eventually cause the material failure. Nevertheless, phase change is not considered in the current work since it is an irreversible process for LMO electrodes, which is normally avoided during battery operation.

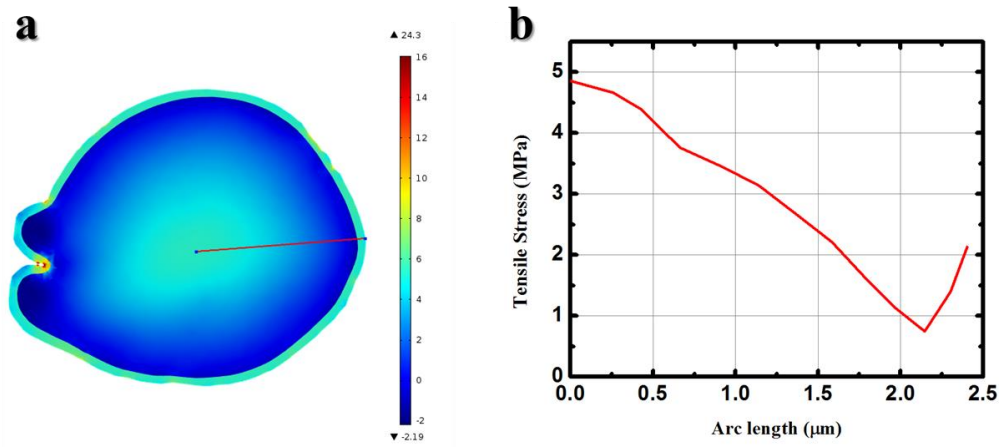

Figure 6-7. Maximum tensile stress distribution inside active material and CBD of particle (1) at the end of discharge at 1C. a) 2D cross section b) along the radial cutline

Hao *et al.* [191] showed that, in a core-shell structure, a jump in radial and tangential stress is observed at the core and shell interface. Their results were based on the modeling of a spherical LMO active particle with a surrounding carbon shell, and the assumption that the radial displacement is continuous at the interface. As shown in **Fig. 6-7**, our result based on the real morphology modeling also demonstrates a similar jump in tensile stress at the interface of the active material and CBD. Particle (1) along with its CBD was chosen as the sample geometry and 2D cross sectional tensile stress within the particle and CBD is shown in **Fig. 6-4a**. The variation of stress from center of the particle to the outer surface of CBD along a 1D cutline (red line in **Fig. 6-7a**) is presented in **Fig. 6-7b**, confirming a marked jump in tensile stress at the interface. To be able to compare our result to the spherical particle in ref. [191], the cutline path was carefully chosen to avoid the high surface stress at concave areas on the particle's surface.

In this study, CBD was assumed to be composed of the usual constituents, polyvinylidene fluoride (PVDF) polymer and Super P carbon black, as typical binder and conductive agent used in LIB electrodes. Different Young's modulus of binding materials investigated by Rahani and Shenoy [187] with a range from 170 MPa for softer binders to 2000 MPa for harder binders, employing 200 MPa to present their simulation results. Takahashi *et al.* [185], on the other hand, reported Young's modulus of 350 MPa for CBD which was submerged in the electrolyte, while Grillet *et al.* [186] deduced a value of 200 MPa for various amounts of carbon black ranging from 10 to 40 wt % added to form swollen PVDF-Carbon black composites. Finally, Wu *et al.* [190] estimated Young's modulus of 184 MPa from the piecewise linear elastic-plastic model of stress-strain curve. Based on these findings, we have chosen the value of 200 MPa to represent the Young's modulus of CBD in our simulation, consistent with the literature values [182,186,187,190]. In addition, Rahani *et al.* [187] also showed that CBD yield stress is one of the most important factors that affect the stress distribution inside the active particles. They chose the yield stress of σ_y=30 MPa for their CBD model, while Wu *et al.* [190] used $\sigma_y = 9.2$ MPa and ultimate tensile stress of 13.4 MPa for their simulation. Finally, Takahashi *et al.* [184] found the value of 16 MPa as the maximum tensile strength of CBD submerged in the electrolyte. In our study, we have chosen the value of 30 MPa for the yield stress which is in good agreement with values reported in the literature [182,187].

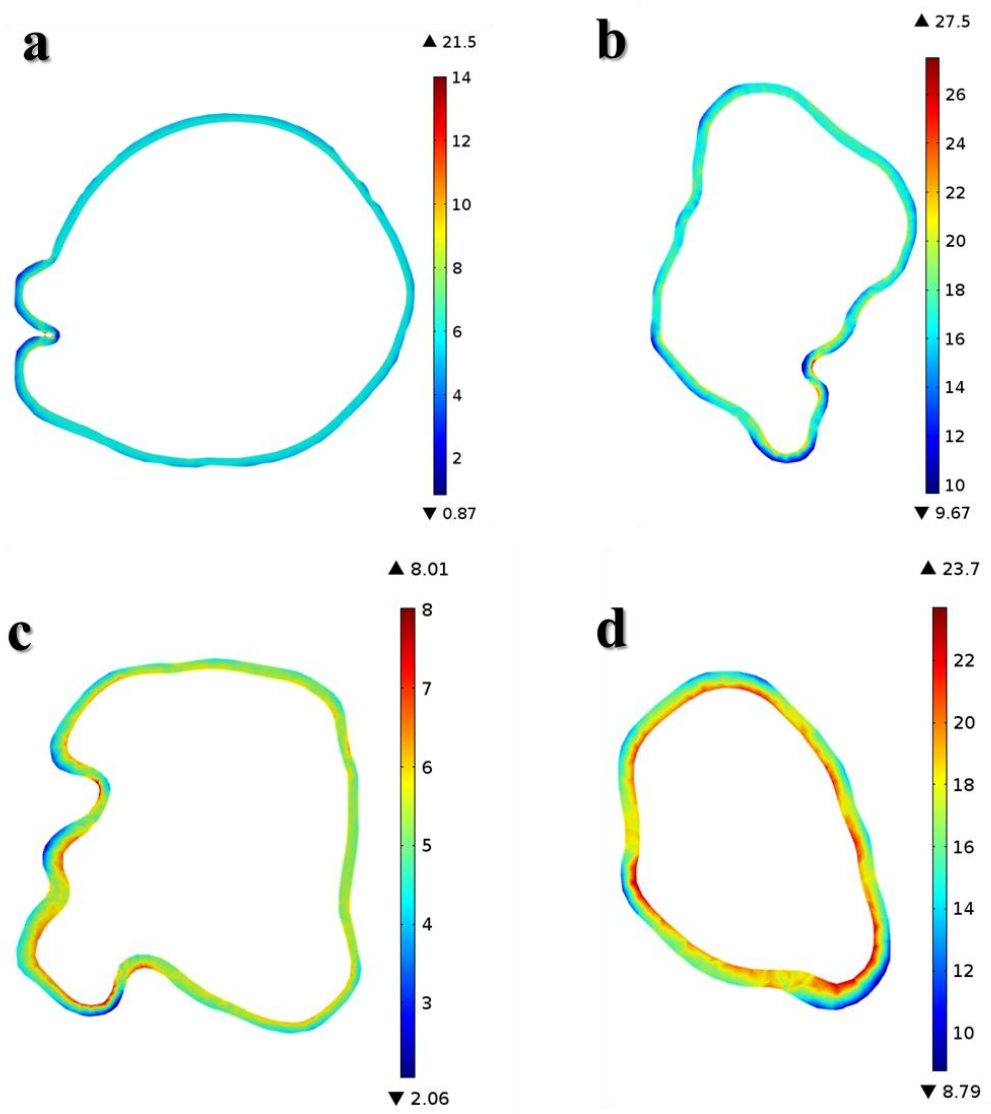

Figure 6-8. Von-Mises stress (MPa) distribution in the CBD layer at the end of galvanostatic discharge at 1 C in a) particle (1), b) particle (2), c) particle (3), and d) particle (4).

In the present study, CBD has been modeled as a ductile material; Since the failure of ductile material is related to the Von-Mises stress rather than tensile stress, it has been chosen to demonstrate stress within the CBD. The 2D cross section of Von-Mises stress in the CBD layer at the end of galvanostatic discharge at C rate=1 is shown in **Fig. 6-8**. The local CBD

stress in vicinity of areas with high concavity tends to increase from particle's surface to the outer surface of CBD, where it tends to decrease from the particle's surface to the outer surface of CBD in areas with high convexity. The maximum Von-Mises stress in the CBD layer at C rate=1 equals to 21.5, 27.5, 8.0, and 23.7 MPa in particles (1), (2), (3), and (4), respectively. These results are significantly lower than the yield stress of 30 MPa, which indicates that CBD is very unlikely to experience plastic deformation.

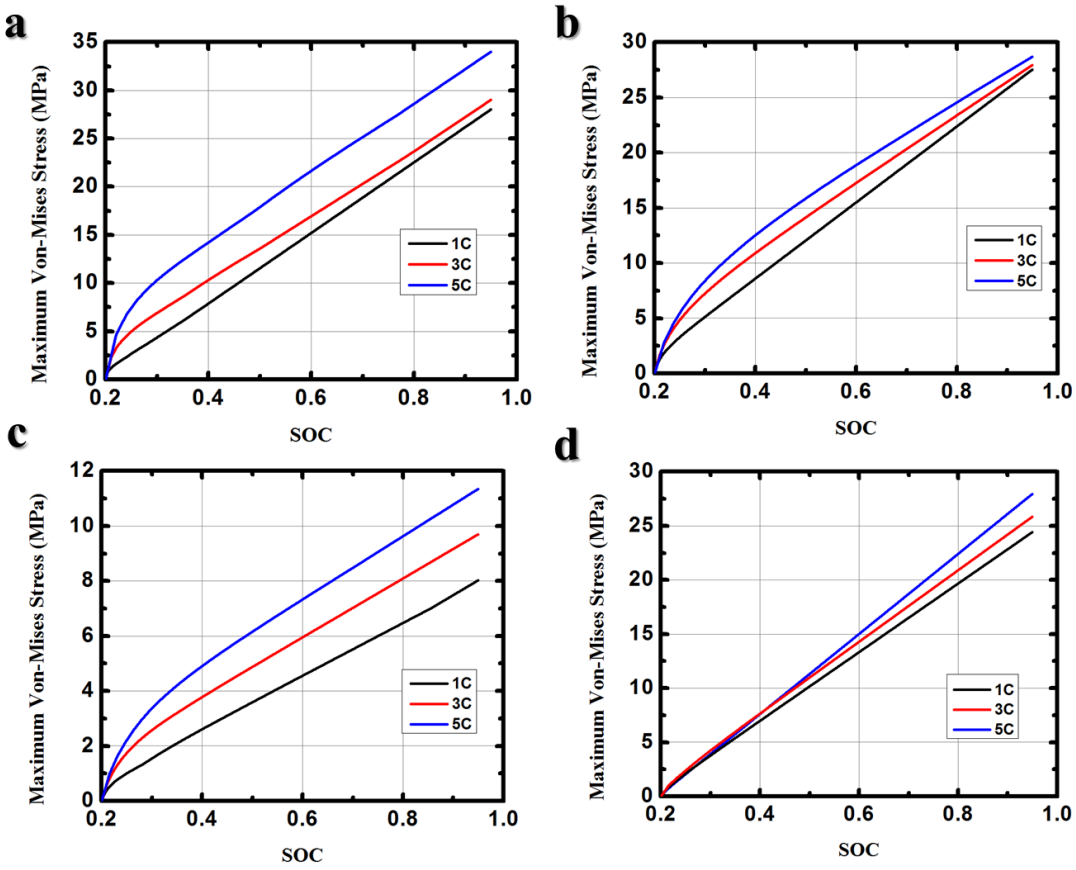

Figure 6-9. Maximum Von-Mises stress in the CBD layer after galvanostatically discharging at various C rates from SOC=0.2 to SOC=0.95 in a) particle (1), b) particle (2), c) particle (3), and d) particle (4).

In order to predict possible material failure due to plastic deformation of CBD that enclose the active LMO particles, we have simulated the maximum stress by galvanostatically discharge at higher C rates from SOC=0.2 to 0.95 as shown in **Fig. 6-9**. In all CBD layers of the particles, the maximum Von-Mises stress is observed to increase as the applied current density increases, the maximum occurring at C rate=5. Similar to the stress distribution in the active material particles discussed above, the maximum stress in the CBD layer is dependent

on the particle size, morphology, CBD thickness, materials properties, and the applied C rate. Having said this, the maximum Von-Mises stress in the CBD layer is found to equal 34.0, 28.7, 11.35, and 27.9 MPa in particles (1), (2), (3), and (4), respectively, when discharged at C rate=5. Since the maximum stress in the CBD layer of particle (1) exceeds 30 MPa, the failure of CBD via plastic deformation can potentially happen. Even though in this study plastic deformation is not included in the model, its occurrence only reduces the stress incurred on the active material particle itself, not affecting the previous prediction that the active material failure is very unlikely.

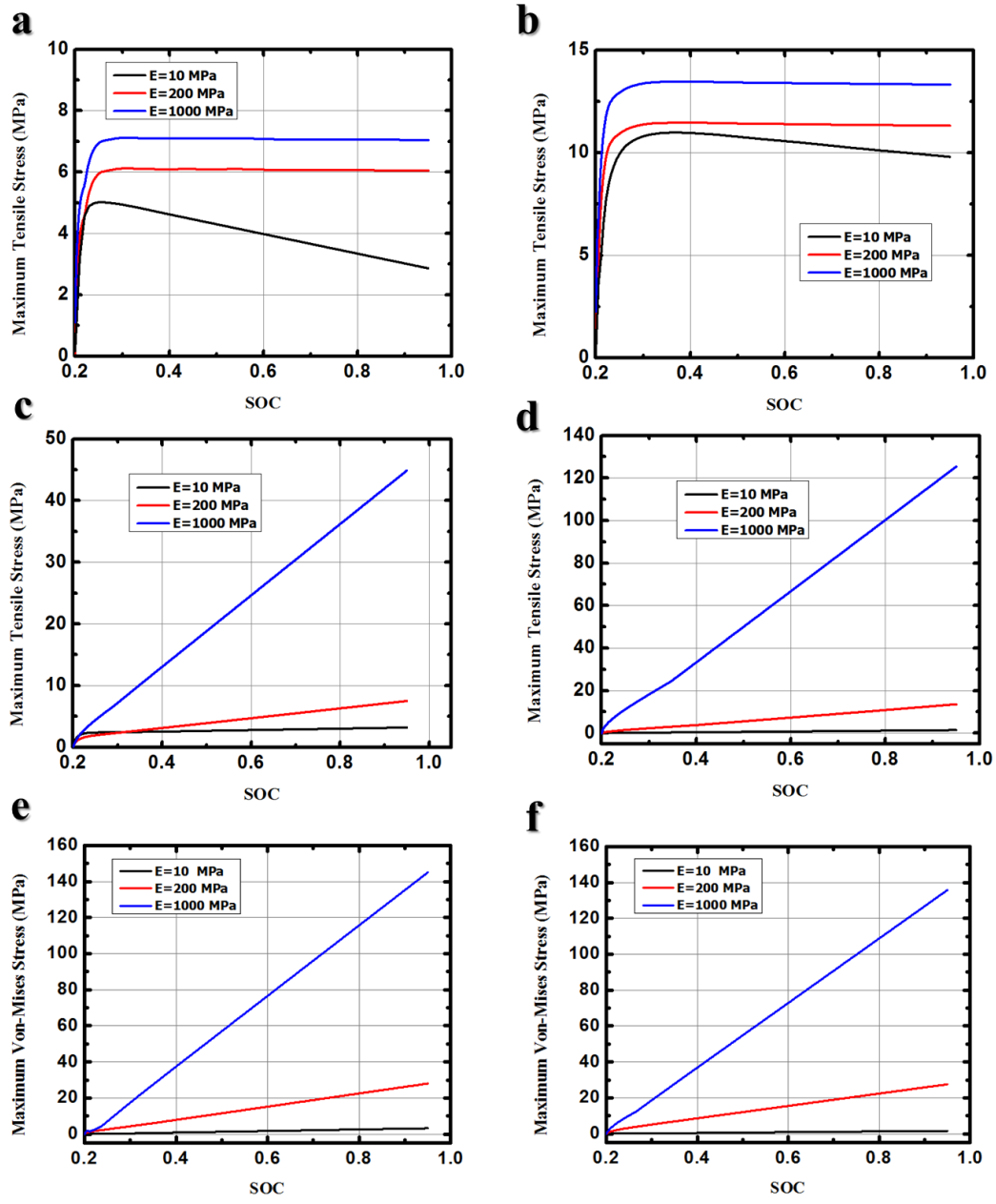

Figure 6-10. Stress (MPa) within LMO active material and CBD at the end of discharge at 1C with varying Young's modulus of CBD a), and b) Maximum tensile stress (bulk stress); c), and d) Maximum tensile stress (surface stress); e), and f) Maximum Von-Mises stress, in particles (1), and (2) respectively.

Additionally, it is noteworthy to mention the simulated stress in the electrodes are highly dependent on the overall mechanical properties of CBD, including Young's modulus, percentage of conductive additive [186] used to fabricate electrodes, as well as the environment in which they are tested such as, dry or wet (submerged in the electrolyte) [185]. In order to identify the effect of different CBD properties on the stress within electrodes, CBDs with low and high Young's moduli of E=10, and 1000 MPa, respectively, have been employed and compared with the reference modulus of E=200 MPa. All other model conditions and parameters were kept unchanged. The results obtained with only particles (1), and (2) are shown due to their higher stress levels compared to particles (3), and (4), but all particles' mechanical behaviors are quite similar. **Fig. 6-10** shows the bulk and surface stress within LMO active materials and Von-Mises stress in CBD during galvanostatic discharge at C rate=1. **Fig. 6-10a** and 10b demonstrate the maximum bulk tensile stress for various Young's moduli within particles (1) and (2), respectively, confirming that higher Young's modulus causes a slight increase in the bulk stress within active material particles. **Fig. 6-10c** and **10d** show the maximum surface tensile stress evolution, occurring at a concave area of particle (1) and (2), respectively. Unlike the bulk stress, increasing Young's modulus to 1000 MPa leads to an extremely large surface stress of 45 MPa in particle (1), and 125 MPa in particle (2) at the end of discharge. These are much higher than 100 MPa of LMO tensile strength and might lead to crack formation and material failure. This again highlights the importance of utilizing the real surface morphology of the active material particle as the model geometry, which cannot be predicted by conventional uniform spherical particle models. The maximum Von-Mises stress for CBD enclosing particles (1), and (2) are also presented in **Fig.**

6-10e and **10f**. Similar to the behavior of the active material, higher Young's modulus results in a dramatic increase in stress within CBD. For E=1000 MPa, plastic failure of CBD is most likely to happen because the maximum stress level of ~140 MPa exceeds the yield stress of CBD. Accordingly, the simulation results demonstrate that lower stiffness is favorable for lower diffusion induced stress in electrode's active material and CBD.

6.5 Conclusions

In this chapter, X-ray nano computed tomography technology has been utilized to successfully capture and model the real morphology of LMO active electrode particles and to investigate the diffusion-induced mechanical stress. Unlike other previously published reports, our investigation considers the effect of a uniform layer of CBD which encapsulates active particles on the mechanical stress during battery discharge. Our results have revealed that the stress generated in the electrode heavily depends on the particle size, local morphology, and mechanical properties of both active material and CBD. Specifically, surface tensile stress has been found to be relatively higher and lower on the surfaces of particles with high surface concavity, and convexity, respectively. In fact, the maximum stress experienced by the active particles during galvanostatic discharge at the rate as high as 5 C has been found to be significantly lower than the material's tensile strength. Inside CBD, however, the stress has been found to reach the levels of yield stress reported in the literature, which can lead to plastic deformation and detachment of CBD resulting in the loss of electrical connectivity of the active particles from the percolated solid network. This result highlights the importance of developing CBD with the optimal composition to achieve mechanical properties with higher

limits to prevent potential power loss and lifetime degradation of LIB electrodes. The unique mechanical stress analysis conducted in this study using real particle morphology is a significant advancement from simplified spherical model-based simulations commonly reported in the literature, which will positively contribute to further improving LIB active electrodes to address continuously rising energy demands.

7. Conclusions and Future Work

7.1 Summary and Conclusions

In the present thesis, image based models have been successfully developed to study multiphysics behaviour of LIB electrodes. The models investigate the interaction among chemistry, mass and charge transport, mechanics, and 3D microstructure of the electrode. In all studies, electrode's real 3D structure is reconstructed from either laboratory or synchrotron radiation nano-XCT images.

Earlier in the thesis work, an imaged-based multiscale model was developed to study the real microstructure of electrodes of lithium ion batteries. The model was based on the real 3D microstructure data, while take advantage of the traditional homogenous 1D model in macroscale to characterize discharge/charge performance. In macroscale, the model was modified through dropping Bruggeman relation and replacing it by reconstructed structure tortuosity. The coupling between micro and macro scales were performed at each time step, unlike using common surrogate based models for microscale. The simulation results could predict the experimental discharge voltage of LFP cathodes at different rates. The simulation showed that the lithium concentration in the electrode active material structure was much higher in the region with smaller cross-section area perpendicular to the lithium intercalation pathway. Such low area regions would intercalate ca. 10 times higher than the area with an average concentration. The approach used in this study provided valuable insight into the spatial distribution of lithium ions inside the microstructure of LIB electrodes. The

heterogeneous structure of LFP causes a wide range of physical and electrochemical properties compared to the homogenous model.

To form a computationally efficient image based model suitable for battery-packs simulations, and thermal, and stress analyses, a RVE model of the LFP electrode was developed in the next study. The model took advantage of computational efficiency of the single-particle model, while simultaneously utilized a RVE from the 3D reconstructed electrode as the model geometry. The simulation results showed good agreement with experimental discharge profile of LFP cathode at various discharge rates. Similar to the multiscale model, the RVE results showed that at any given SOC, the lithium concentration is elevated in the regions with smaller cross-sectional area perpendicular to the diffusion path in the active material and in the region with higher surface area exposed to the electrolyte. Moreover, the distribution of the lithium inside RVE was demonstrated to be wider than that of the single-spherical-particle model due to the inherent electrode heterogeneous structure.

To further analysis the microstructural behavior of nano-structured electrodes, the next study involved the 3D microstructural characterization of the LTO electrode based on multiple imaging mode synchrotron nano XCT. The synchrotron with a 58 nm resolution was used to reconstruct 3D microstructure of the electrode, which was then characterized for its geometrical and electrochemical properties. The imaging was conducted using two different modes, absorption contrast and Zernike phase contrast, to resolve the electrode's active material, CBD, and pore phases in different ways. The 3D image revealed that some primary LTO nano-particles tend to agglomerate and form secondary micro-sized particles. Four secondary particles were selected and their size, volume specific surface area, and degree of

non-sphericity were quantified. The secondary particles showed different volume specific surface area ranging from 3.14 to 3.62 (μm^{-1}) and various degree of sphericity from 0.71 to 0.91. The electrode's resistance to charge and mass transport was quantified by estimating solid and pore domain tortuosities using two methods: 1) simulation based on mass transport analogy and 2) pure geometry. The resulting tortuosities showed that the commonly used Bruggeman relation for homogeneous models is a poor estimator of the electrode tortuosity. In addition, tortuosities, obtained from both methods, vary significantly depending on the directions, confirming highly anisotropic and heterogeneous nature of pore and solid domains. To further investigate the microstructural heterogeneity, a computational framework was developed to simulate electrochemical performance of the LTO electrode. Unlike commonly used absorption contrast reconstructed structure, the model took advantage of Zernike phase contrast reconstructed geometry. The lack of CBD in absorption contrast results in isolated active material particles, whereas Zernike phase contrast provides an integrated percolated network of active material and CBD together, making it suitable for FEM simulation. The model was an improvement over our previous RVE model as it included electron transport to the governing equations as well as solid phase diffusion. The model was validated with the experimental data obtained from a coin cell performance. The simulation results revealed irregular and non-uniform distribution of physical and electrochemical properties within the solid domain, which could be attributed to the electrode's structural heterogeneity.

Ultimately, nano-XCT technology was utilized to investigate the mechanical response of a commercial LMO electrode. In this way, the 3D real morphology of LMO active electrode particles was reconstructed and the diffusion-induced mechanical stress within particles was

simulated. Unlike other previously published reports, our investigation considered the effect of a uniform layer of CBD which encapsulated active particles. Our results revealed that the stress generated in the electrode heavily depends on the particle size, local morphology, and mechanical properties of both active material and CBD. Specifically, surface tensile stress was found to be relatively higher and lower on the surfaces of particles with high surface concavity, and convexity, respectively. In fact, the maximum stress experienced by the active particles during galvanostatic discharge at the rate as high as 5 C was found to be significantly lower than the material's tensile strength. Inside CBD, however, the stress was found to reach the levels of yield stress reported in the literature, which could lead to plastic deformation and detachment of CBD resulting in the loss of electrical connectivity of the active particles from the percolated solid network. This result highlighted the importance of developing CBD with the optimal composition to achieve mechanical properties with higher limits to prevent potential power loss and lifetime degradation of LIB electrodes. The unique mechanical stress analysis conducted in this study using real particle morphology was a significant advancement over the simplified spherical model-based simulations commonly reported in the literature, which would positively contribute to further improving LIB cycle life.

7.2 Proposed future work

Based on the findings of these studies, some future directions for the image based modeling of LIBs can be suggested:

1. Multiscale modeling

The multiscale model just involved solid phase conservation of mass in microscale. The future work to follow multiscale model could improve the model by inclusion of the solid phase charge transfer. It is also suggested that in addition to solid phase, the electrolyte phase is also considered. The conservation of mass and charge within electrolyte phase provides electric potential and lithium-ion concentration in microscale. In this way, the pore-wall flux obtained from Butler-Volmer kinetics can be calculated from microscale data, in contrast to the current multiscale model in which it is mapped from macroscale data. This enables the heterogeneous distribution of current density on the microstructures.

2. CBD inclusion in multiphysics simulation

   Although we obtained the CBD phase by combination of absorption contrast and Zernike phase contrast imaging mode in the third study, there is still significant uncertainty about the exact location of the CBD inside electrode structure. In both multiscale and RVE models, we assumed that all neighboring particles are perfectly bound together and lithium may diffuse from one particle to its immediate neighbor. Having the exact location of CBD enables to disconnect individual particles which results in more accurate lithium diffusion path in the electrode structure.

3. The mechanical stress study in this thesis were performed in galvanostatic operating condition. However, when an EV runs in real operating conditions, it draws totally different current pattern from battery. To simulate the stress generated in vehicle batteries, it is suggested the present model is simulated according to specific vehicle driving cycle such as Urban Dynamometer Driving Schedule (UDDS), Highway Fuel

Economy Test Schedule (HWFET) and US06 for aggressive driving, to compare different stress level at various vehicle battery driving scenarios. This enables electrode failure prediction at real operating conditions.

References

[1] W. Li, B. Song, A. Manthiram, High-voltage positive electrode materials for lithium-ion batteries, Chem. Soc. Rev. 46 (2017) 3006–3059. doi:10.1039/C6CS00875E.

[2] M. Armand, Trascon Armand, 414 (2001) 359–367. doi:10.1038/35104644.

[3] M. Armand, J.-M. Tarascon, Building better batteries., Nature. 451 (2008) 652–657. doi:10.1038/451652a.

[4] G. Kim, K. Smith, Three-Dimensional Lithium-Ion Battery Model Multi-Scale Physics in Li-ion Battery, (2008).

[5] A.A. Franco, Multiscale modelling and numerical simulation of rechargeable lithium ion batteries: concepts, methods and challenges, RSC Adv. 3 (2013) 13027. doi:10.1039/c3ra23502e.

[6] S.A. Roberts, H. Mendoza, V.E. Brunini, B.L. Trembacki, D.R. Noble, A.M. Grillet, Insights Into Lithium-Ion Battery Degradation and Safety Mechanisms From Mesoscale Simulations Using Experimentally Reconstructed Mesostructures, J. Electrochem. Energy Convers. Storage. 13 (2016) 31005. doi:10.1115/1.4034410.

[7] P. Pietsch, V. Wood, X-Ray Tomography for Lithium Ion Battery Research: A Practical Guide, Annu. Rev. Mater. Res. 471229 (2017) 1–12. doi:10.1146/annurev-matsci-070616.

[8] D. Kehrwald, P.P.R. Shearing, N.P.N. Brandon, P.K.P. Sinha, S.S.J.S. Harris, Local Tortuosity Inhomogeneities in a Lithium Battery Composite Electrode, J. Electrochem. Soc. 158 (2011) A1393–A1399. doi:10.1149/2.079112jes.

[9] N. Besnard, A. Etiemble, T. Douillard, O. Dubrunfaut, P. Tran-Van, L. Gautier, S. Franger, J.C. Badot, E. Maire, B. Lestriez, Multiscale Morphological and Electrical Characterization of Charge Transport Limitations to the Power Performance of Positive Electrode Blends for Lithium-Ion Batteries, Adv. Energy Mater. 7 (2017) 1–16. doi:10.1002/aenm.201602239.

[10] A.G. Kashkooli, S. Farhad, D.U. Lee, K. Feng, S. Litster, S.K. Babu, L. Zhu, Z. Chen, Multiscale modeling of lithium-ion battery electrodes based on nano-scale X-ray computed tomography, J. Power Sources. 307 (2016) 496–509. doi:10.1016/j.jpowsour.2015.12.134.

[11] A.G. Kashkooli, A. Amirfazli, S. Farhad, D.U. Lee, S. Felicelli, H.W. Park, K. Feng, V. De Andrade, Z. Chen, Representative volume element model of lithium-ion battery electrodes based on X-ray nano-tomography, J. Appl. Electrochem. 47 (2017) 281–293. doi:10.1007/s10800-016-1037-y.

[12] A.G. Kashkooli, G. Lui, S. Farhad, D.U. Lee, K. Feng, A. Yu, Z. Chen, Nano-particle size effect on the performance of Li4Ti5O12 spinel, Electrochim. Acta. 196 (2016) 33–40. doi:10.1016/j.electacta.2016.02.153.

[13] A.G. Kashkooli, E. Foreman, S. Farhad, D.U. Lee, K. Feng, G. Lui, V. De Andrade, Z. Chen, Morphological and Electrochemical Characterization of Nanostructured $Li_4Ti_5O_{12}$ Electrodes Using Multiple Imaging Mode Synchrotron X-ray Computed Tomography, J. Electrochem. Soc. 164 (2017) A2861–A2871. doi:10.1149/2.0101713jes.

[14] A. Ghorbani Kashkooli, E. Foreman, S. Farhad, D.U. Lee, W. Ahn, K. Feng, V. De

Andrade, Z. Chen, Synchrotron X-ray nano computed tomography based simulation of stress evolution in LiMn 2 O 4 electrodes, Electrochim. Acta. 247 (2017) 1103–1116. doi:10.1016/j.electacta.2017.07.089.

[15] H. Wu, Y. Cui, Designing nanostructured Si anodes for high energy lithium ion batteries, Nano Today. 7 (2012) 414–429. doi:10.1016/j.nantod.2012.08.004.

[16] M. Zhang, T. Wang, G. Cao, Promises and challenges of tin-based compounds as anode materials for lithium-ion batteries, Int. Mater. Rev. 60 (2015) 330–352. doi:10.1179/1743280415Y.0000000004.

[17] C. Liu, Z.G. Neale, G. Cao, Understanding electrochemical potentials of cathode materials in rechargeable batteries, Mater. Today. 19 (2016) 109–123. doi:10.1016/j.mattod.2015.10.009.

[18] V. a Sethuraman, V. Srinivasan, J. Newman, Analysis of Electrochemical Lithiation and Delithiation Kinetics in Silicon, J. Electrochem. Soc. 160 (2013) A394–A403. doi:10.1149/2.008303jes.

[19] N. Nitta, G. Yushin, High-capacity anode materials for lithium-ion batteries: Choice of elements and structures for active particles, Part. Part. Syst. Charact. 31 (2014) 317–336. doi:10.1002/ppsc.201300231.

[20] J. Lim, E. Choi, V. Mathew, D. Kim, D. Ahn, J. Gim, S.-H. Kang, J. Kim, Enhanced High-Rate Performance of Li[sub 4]Ti[sub 5]O[sub 12] Nanoparticles for Rechargeable Li-Ion Batteries, J. Electrochem. Soc. 158 (2011) A275. doi:10.1149/1.3527983.

[21] K. Feng, W. Ahn, G. Lui, H.W. Park, A.G. Kashkooli, G. Jiang, X. Wang, X. Xiao, Z.

Chen, Implementing an in-situ carbon network in Si/reduced graphene oxide for high performance lithium-ion battery anodes, Nano Energy. 19 (2016) 187–197. doi:10.1016/j.nanoen.2015.10.025.

[22] B. Ammundsen, J. Paulsen, Novel lithium-ion cathode materials based on layered manganese oxides, Adv. Mater. 13 (2001) 943–956. doi:10.1002/1521-4095(200107)13:12/13<943::AID-ADMA943>3.0.CO;2-J.

[23] Y.K. Sun, S.T. Myung, B.C. Park, J. Prakash, I. Belharouak, K. Amine, High-energy cathode material for long-life and safe lithium batteries, Nat. Mater. 8 (2009) 320–324. doi:10.1038/nmat2418.

[24] J.W. Fergus, Recent developments in cathode materials for lithium ion batteries, J. Power Sources. 195 (2010) 939–954. doi:10.1016/j.jpowsour.2009.08.089.

[25] D. Jugović, D. Uskoković, A review of recent developments in the synthesis procedures of lithium iron phosphate powders, J. Power Sources. 190 (2009) 538–544. doi:10.1016/j.jpowsour.2009.01.074.

[26] C. Alaoui, Thermal management for energy storage system for smart grid, J. Energy Storage. 13 (2017) 313–324. doi:10.1016/j.est.2017.07.027.

[27] E. Samadani, S. Farhad, W. Scott, M. Mastali, L.E. Gimenez, M. Fowler, R. a. Fraser, Empirical Modeling of Lithium-ion Batteries Based on Electrochemical Impedance Spectroscopy Tests, Electrochim. Acta. 160 (2015) 169–177. doi:10.1016/j.electacta.2015.02.021.

[28] Z. Guo, B.Y. Liaw, X. Qiu, L. Gao, C. Zhang, Optimal charging method for lithium ion batteries using a universal voltage protocol accommodating aging, J. Power Sources.

274 (2015) 957–964. doi:10.1016/j.jpowsour.2014.10.185.

[29] M. Xiao, S.-Y. Choe, Impedance model of lithium ion polymer battery considering temperature effects based on electrochemical principle: Part I for high frequency, J. Power Sources. 277 (2015) 403–415. doi:10.1016/j.jpowsour.2014.10.157.

[30] M. Doyle, J. Newman, The use of mathematical modeling in the design of lithium/polymer battery systems, Electrochim. Acta. 40 (1995) 2191–2196. doi:10.1016/0013-4686(95)00162-8.

[31] M. Doyle, Modeling of Galvanostatic Charge and Discharge of the Lithium/Polymer/Insertion Cell, J. Electrochem. Soc. 140 (1993) 1526. doi:10.1149/1.2221597.

[32] V. Srinivasan, J. Newman, Discharge Model for the Lithium Iron-Phosphate Electrode, J. Electrochem. Soc. 151 (2004) A1517. doi:10.1149/1.1785012.

[33] M. Mastali Majdabadi, S. Farhad, M. Farkhondeh, R. a. Fraser, M. Fowler, Simplified electrochemical multi-particle model for LiFePO4 cathodes in lithium-ion batteries, J. Power Sources. 275 (2015) 633–643. doi:10.1016/j.jpowsour.2014.11.066.

[34] M. Farkhondeh, M. Safari, M. Pritzker, M. Fowler, T. Han, J. Wang, C. Delacourt, Full-Range Simulation of a Commercial LiFePO4 Electrode Accounting for Bulk and Surface Effects: A Comparative Analysis, J. Electrochem. Soc. 161 (2013) A201–A212. doi:10.1149/2.094401jes.

[35] G.K. Singh, G. Ceder, M.Z. Bazant, Intercalation dynamics in rechargeable battery materials: General theory and phase-transformation waves in LiFePO4, Electrochim. Acta. 53 (2008) 7599–7613. doi:10.1016/j.electacta.2008.03.083.

[36] A. a Franco, Multiscale modelling and numerical simulation of rechargeable lithium ion batteries: concepts, methods and challenges, Rsc Adv. 3 (2013) 13027–13058. doi:10.1039/c3ra23502e.

[37] M. Maccario, L. Croguennec, F. Weill, F. Le Cras, C. Delmas, C-containing LiFePO4 materials - Part II: Electrochemical characterization, Solid State Ionics. 179 (2008) 2383–2389. doi:10.1016/j.ssi.2008.09.005.

[38] P. Prosini, M. Lisi, D. Zane, M. Pasquali, Determination of the chemical diffusion coefficient of lithium in LiFePO4, Solid State Ionics. 148 (2002) 45–51. doi:10.1016/S0167-2738(02)00134-0.

[39] P.P. Prosini, M. Lisi, S. Scaccia, M. Carewska, F. Cardellini, M. Pasquali, Synthesis and Characterization of Amorphous Hydrated FePO[sub 4] and Its Electrode Performance in Lithium Batteries, J. Electrochem. Soc. 149 (2002) A297. doi:10.1149/1.1435359.

[40] S. Franger, F. Le Cras, C. Bourbon, H. Rouault, LiFePO[sub 4] Synthesis Routes for Enhanced Electrochemical Performance, Electrochem. Solid-State Lett. 5 (2002) A231. doi:10.1149/1.1506962.

[41] C. Weng, J. Sun, H. Peng, An Open-Circuit-Voltage Model of Lithium-Ion Batteries for Effective Incremental Capacity Analysis, Vol. 1 Aer. Veh. Aerosp. Control. Altern. Energy; Automot. Control Syst. Batter. Syst. Beams Flex. Struct. Biol. Control Its Appl. Bio-Medical Bio-Mechanical Syst. Biomed. Robot. (2013) V001T05A002. doi:10.1115/DSCC2013-3979.

[42] X. Hu, S. Li, H. Peng, A comparative study of equivalent circuit models for Li-ion

batteries, J. Power Sources. 198 (2012) 359–367. doi:10.1016/j.jpowsour.2011.10.013.

[43] V. Ramadesigan, P.W.C. Northrop, S. De, S. Santhanagopalan, R.D. Braatz, V.R. Subramanian, Modeling and Simulation of Lithium-Ion Batteries from a Systems Engineering Perspective, J. Electrochem. Soc. 159 (2012) R31–R45. doi:10.1149/2.018203jes.

[44] S. Santhanagopalan, Q. Guo, P. Ramadass, R.E. White, Review of models for predicting the cycling performance of lithium ion batteries, J. Power Sources. 156 (2006) 620–628. doi:10.1016/j.jpowsour.2005.05.070.

[45] D. Zhang, B.N. Popov, R.E. White, Modeling Lithium Intercalation of a Single Spinel Particle under Potentiodynamic Control, J. Electrochem. Soc. 147 (2000) 831. doi:10.1149/1.1393279.

[46] M. Safari, C. Delacourt, Mathematical Modeling of Lithium Iron Phosphate Electrode: Galvanostatic Charge/Discharge and Path Dependence, J. Electrochem. Soc. 158 (2011) A63. doi:10.1149/1.3515902.

[47] C. Delacourt, M. Safari, Analysis of lithium deinsertion/insertion in LiyFePO4 with a simple mathematical model, Electrochim. Acta. 56 (2011) 5222–5229. doi:10.1016/j.electacta.2011.03.030.

[48] M. Farkhondeh, C. Delacourt, Mathematical Modeling of Commercial LiFePO4 Electrodes Based on Variable Solid-State Diffusivity, J. Electrochem. Soc. 159 (2012) A177. doi:10.1149/2.073202jes.

[49] C. Delacourt, M. Safari, Life Simulation of a Graphite/LiFePO4 Cell under Cycling and Storage, J. Electrochem. Soc. 159 (2012) A1283–A1291. doi:10.1149/2.049208jes.

[50] J. Newman, W. Tiedemann, Porous-electrode theory with battery applications, AIChE J. 21 (1975) 25–41. doi:10.1002/aic.690210103.

[51] V. Ramadesigan, P.W.C. Northrop, S. De, S. Santhanagopalan, R.D. Braatz, V.R. Subramanian, Modeling and Simulation of Lithium-Ion Batteries from a Systems Engineering Perspective, J. Electrochem. Soc. 159 (2012) R31–R45. doi:10.1149/2.018203jes.

[52] T.F. Fuller, M. Doyle, J. Newman, TECHNICAL PAPERS ELECTROCHEMICAL SCIENCE AND TECHNOLOGY Simulation and Optimization of the Dual Lithium Ion Insertion Cell, 141 (1994).

[53] P.R.R. Shearing, L.E.E. Howard, P.S.S. Jørgensen, N.P.P. Brandon, S.J.J. Harris, Characterization of the 3-dimensional microstructure of a graphite negative electrode from a Li-ion battery, Electrochem. Commun. 12 (2010) 374–377. doi:10.1016/j.elecom.2009.12.038.

[54] T.B. Sercombe, X. Xu, V.J. Challis, R. Green, S. Yue, Z. Zhang, P.D. Lee, Failure modes in high strength and stiffness to weight scaffolds produced by Selective Laser Melting, Mater. Des. 67 (2015) 501–508. doi:10.1016/j.matdes.2014.10.063.

[55] L.L. Lavery, J. Gelb, A.P. Merkle, A. Steinbach, X-Ray Microscopy for Hierarchical Multi-Scale Materials, Micros. Today. 22 (2014) 16–21. doi:10.1017/S155192951400056X.

[56] E. Maire, P.J. Withers, Quantitative X-ray tomography, Int. Mater. Rev. 59 (2014) 1–43. doi:10.1179/1743280413Y.0000000023.

[57] D.P. Finegan, M. Scheel, J.B. Robinson, B. Tjaden, I. Hunt, T.J. Mason, J. Millichamp,

M. Di Michiel, G.J. Offer, G. Hinds, D.J.L. Brett, P.R. Shearing, In-operando high-speed tomography of lithium-ion batteries during thermal runaway, Nat. Commun. 6 (2015) 6924. doi:10.1038/ncomms7924.

[58] M. Holt, R. Harder, R. Winarski, V. Rose, Nanoscale Hard X-Ray Microscopy Methods for Materials Studies, Annu. Rev. Mater. Res. 43 (2013) 183–211. doi:10.1146/annurev-matsci-071312-121654.

[59] V. De Andrade, A. Deriy, M.J. Wojcik, D. Gürsoy, D. Shu, K. Fezzaa, F. De Carlo, Nanoscale 3D imaging at the Advanced Photon Source, SPIE Newsroom. (2016) 2–4. doi:10.1117/2.1201604.006461.

[60] W.K. Epting, J. Gelb, S. Litster, Resolving the Three-Dimensional Microstructure of Polymer Electrolyte Fuel Cell Electrodes using Nanometer-Scale X-ray Computed Tomography, Adv. Funct. Mater. 22 (2012) 555–560. doi:10.1002/adfm.201101525.

[61] J. Als-Nielsen, D. McMorrow, Elements of Modern X-ray Physics, John Wiley & Sons, Inc., Hoboken, NJ, USA, 2011. doi:10.1002/9781119998365.

[62] A.S. Kumar, Computational Methods for Nanoscale X-ray Computed Tomography Image Analysis of Fuel Cell and Battery Materials Computational Methods for Nanoscale X-ray, (2016).

[63] S.J.J. Cooper, D.S.S. Eastwood, J. Gelb, G. Damblanc, D.J.L.J.L. Brett, R.S.S. Bradley, P.J.J. Withers, P.D.D. Lee, a. J.J. Marquis, N.P.P. Brandon, P.R.R. Shearing, Image based modelling of microstructural heterogeneity in LiFePO 4 electrodes for Li-ion batteries, J. Power Sources. 247 (2014) 1033–1039. doi:10.1016/j.jpowsour.2013.04.156.

[64] F. Tariq, V. Yufit, M. Kishimoto, P.R. Shearing, S. Menkin, D. Golodnitsky, J. Gelb, E. Peled, N.P. Brandon, Three-dimensional high resolution X-ray imaging and quantification of lithium ion battery mesocarbon microbead anodes, J. Power Sources. 248 (2014) 1014–1020. doi:10.1016/j.jpowsour.2013.08.147.

[65] M. Ebner, F. Geldmacher, F. Marone, M. Stampanoni, V. Wood, X-Ray Tomography of Porous, Transition Metal Oxide Based Lithium Ion Battery Electrodes, Adv. Energy Mater. 3 (2013) 845–850. doi:10.1002/aenm.201200932.

[66] B. Yan, C. Lim, L. Yin, L. Zhu, Three Dimensional Simulation of Galvanostatic Discharge of LiCoO2 Cathode Based on X-ray Nano-CT Images, J. Electrochem. Soc. 159 (2012) A1604–A1614. doi:10.1149/2.024210jes.

[67] D.-W. Chung, P.R. Shearing, N.P. Brandon, S.J. Harris, R.E. Garcia, Particle Size Polydispersity in Li-Ion Batteries, J. Electrochem. Soc. 161 (2014) A422–A430. doi:10.1149/2.097403jes.

[68] C. Lim, B. Yan, L. Yin, L. Zhu, Simulation of diffusion-induced stress using reconstructed electrodes particle structures generated by micro/nano-CT, Electrochim. Acta. 75 (2012) 279–287. doi:10.1016/j.electacta.2012.04.120.

[69] J.B. Dunn, L. Gaines, J.C. Kelly, C. James, K.G. Gallagher, The significance of Li-ion batteries in electric vehicle life-cycle energy and emissions and recycling's role in its reduction, Energy Environ. Sci. 8 (2014) 158–168. doi:10.1039/C4EE03029J.

[70] R.A.F. and M.F. Ehsan Samadani1, Mehrdad Mastali1, Siamak Farhad, E. Samadani, M. Mastali, S. Farhad, R.A. Fraser, And, M. Fowler, Li-ion battery performance and degradation in electric vehicles under different usage scenarios, Int. J. Energy Res. 31

(2015) 135–147. doi:10.1002/er.3378.

[71] X. Li, D. Luo, X. Zhang, Z. Zhang, Enhancement of electrochemical performances for LiFePO4/C with 3D-grape-bunch structure and selection of suitable equivalent circuit for fitting EIS results, J. Power Sources. 291 (2015) 75–84. doi:10.1016/j.jpowsour.2015.05.018.

[72] Y. Honda, S. Muto, K. Tatsumi, H. Kondo, K. Horibuchi, T. Kobayashi, T. Sasaki, Microscopic mechanism of path-dependence on charge–discharge history in lithium iron phosphate cathode analysis using scanning transmission electron microscopy and electron energy-loss spectroscopy spectral imaging, J. Power Sources. 291 (2015) 85–94. doi:10.1016/j.jpowsour.2015.04.183.

[73] S.J. Dillon, K. Sun, Microstructural design considerations for Li-ion battery systems, Curr. Opin. Solid State Mater. Sci. 16 (2012) 153–162. doi:10.1016/j.cossms.2012.03.002.

[74] K.M.O. Jensen, X. Yang, J. V. Laveda, W.G. Zeier, K. a. See, M.D. Michiel, B.C. Melot, S. a. Corr, S.J.L. Billinge, X-Ray Diffraction Computed Tomography for Structural Analysis of Electrode Materials in Batteries, J. Electrochem. Soc. 162 (2015) A1310–A1314. doi:10.1149/2.0771507jes.

[75] W.B. Gu, B.Y. Wang, C.Y., Gu, W.B., Liaw, Micro-Macroscopic Coupled Modeling of Batteries and Fuel Cells, J. Electrochem. Soc. 145 (1998) 3418. doi:10.1149/1.1838821.

[76] V. Chabot, S. Farhad, Z. Chen, A.S. Fung, A. Yu, F. Hamdullahpur, Effect of electrode physical and chemical properties on lithium-ion battery performance, Int. J. Energy Res.

31 (2007) 135–147. doi:10.1002/er.

[77] W.B. Gu, C.Y. Wang, J.W. Weidner, R.G. Jungst, G. Nagasubramanian, Computational Fluid Dynamics Modeling of a Lithium/Thionyl Chloride Battery with Electrolyte Flow, J. Electrochem. Soc. 147 (2000) 427. doi:10.1149/1.1393213.

[78] H. Zarrin, S. Farhad, F. Hamdullahpur, V. Chabot, A. Yu, M. Fowler, Z. Chen, Effects of diffusive charge transfer and salt concentration gradient in electrolyte on Li-ion battery energy and power densities, Electrochim. Acta. 125 (2014) 117–123. doi:10.1016/j.electacta.2014.01.022.

[79] M.F. M.M. Majdabadi Kohneh, E. Samadani, S. Farhad, R. Fraser, Three-dimensional Electrochemical Analysis of a Graphite/LiFePO4 Li-ion Cell to Improve Its Durability, SAE Tech. Pap. (2015). doi:10.4271/2015-01-1182.

[80] R. Fu, S. Choe, V. Agubra, J. Fergus, Development of a physics-based degradation model for lithium ion polymer batteries considering side reactions, J. Power Sources. 278 (2015) 506–521. doi:10.1016/j.jpowsour.2014.12.059.

[81] C.H. Lee, S.J. Bae, M. Jang, A study on effect of lithium ion battery design variables upon features of thermal-runaway using mathematical model and simulation, J. Power Sources. 293 (2015) 498–510. doi:10.1016/j.jpowsour.2015.05.095.

[82] R. Zhao, J. Liu, J. Gu, The effects of electrode thickness on the electrochemical and thermal characteristics of lithium ion battery, Appl. Energy. 139 (2015) 220–229. doi:10.1016/j.apenergy.2014.11.051.

[83] C.-W. Wang, A.M. Sastry, Mesoscale Modeling of a Li-Ion Polymer Cell, J. Electrochem. Soc. 154 (2007) A1035. doi:10.1149/1.2778285.

[84] A. Gupta, J.H. Seo, X. Zhang, W. Du, A.M. Sastry, W. Shyy, Effective Transport Properties of LiMn2O4 Electrode via Particle-Scale Modeling, J. Electrochem. Soc. 158 (2011) A487. doi:10.1149/1.3560441.

[85] D.-W. Chung, M. Ebner, D.R. Ely, V. Wood, R. Edwin García, Validity of the Bruggeman relation for porous electrodes, Model. Simul. Mater. Sci. Eng. 21 (2013) 74009–74025. doi:10.1088/0965-0393/21/7/074009.

[86] G.B. Less, J.H. Seo, S. Han, a. M. Sastry, J. Zausch, a. Latz, S. Schmidt, C. Wieser, D. Kehrwald, S. Fell, Micro-Scale Modeling of Li-Ion Batteries: Parameterization and Validation, J. Electrochem. Soc. 159 (2012) A697. doi:10.1149/2.096205jes.

[87] M. Ebner, F. Marone, M. Stampanoni, V. Wood, Visualization and quantification of electrochemical and mechanical degradation in Li ion batteries., Science. 342 (2013) 716–20. doi:10.1126/science.1241882.

[88] B. Yan, C. Lim, L. Yin, L. Zhu, Simulation of heat generation in a reconstructed LiCoO2 cathode during galvanostatic discharge, Electrochim. Acta. 100 (2013) 171–179. doi:10.1016/j.electacta.2013.03.132.

[89] D.-W.D.-W.D.-W.D.-W.D.-W. Chung, P.R. Shearing, N.P. Brandon, S.J. Harris, R.E. García, R.E. Garcia, R.E. García, Particle Size Polydispersity in Li-Ion Batteries, J. Electrochem. Soc. 161 (2014) A422–A430. doi:10.1149/2.097403jes.

[90] X. Zhang, A.M. Sastry, W. Shyy, Intercalation-Induced Stress and Heat Generation within Single Lithium-Ion Battery Cathode Particles, J. Electrochem. Soc. 155 (2008) A542. doi:10.1149/1.2926617.

[91] L. Zielke, T. Hutzenlaub, D.R. Wheeler, C.-W. Chao, I. Manke, A. Hilger, N. Paust, R.

Zengerle, S. Thiele, Three-Phase Multiscale Modeling of a LiCoO 2 Cathode: Combining the Advantages of FIB-SEM Imaging and X-Ray Tomography, Adv. Energy Mater. (2014) n/a-n/a. doi:10.1002/aenm.201401612.

[92] G. Richardson, G. Denuault, C.P. Please, Multiscale modelling and analysis of lithium-ion battery charge and discharge, J. Eng. Math. 72 (2012) 41–72. doi:10.1007/s10665-011-9461-9.

[93] X. Zhang, Multiscale Modeling of Li-ion Cells: Mechanics, Heat Generation and Electrochemical Kinetics, (2009) 1–178.

[94] L. Tan, N. Zabaras, Multiscale modeling of alloy solidification using a database approach, J. Comput. Phys. 227 (2007) 728–754. doi:10.1016/j.jcp.2007.08.016.

[95] N. V. Queipo, R.T. Haftka, W. Shyy, T. Goel, R. Vaidyanathan, P. Kevin Tucker, Surrogate-based analysis and optimization, Prog. Aerosp. Sci. 41 (2005) 1–28. doi:10.1016/j.paerosci.2005.02.001.

[96] W. Du, N. Xue, W. Shyy, J.R.R. a. Martins, A Surrogate-Based Multi-Scale Model for Mass Transport and Electrochemical Kinetics in Lithium-Ion Battery Electrodes, J. Electrochem. Soc. 161 (2014) E3086–E3096. doi:10.1149/2.013408jes.

[97] X-ray Computed Tomography Facility, (n.d.). http://www.cmu.edu/me/xctf/.

[98] S. Komini Babu, A.I. Mohamed, J.F. Whitacre, S. Litster, Multiple imaging mode X-ray computed tomography for distinguishing active and inactive phases in lithium-ion battery cathodes, J. Power Sources. 283 (2015) 314–319. doi:10.1016/j.jpowsour.2015.02.086.

[99] G. Liu, H. Zheng, X. Song, V.S. Battaglia, Particles and Polymer Binder Interaction:

A Controlling Factor in Lithium-Ion Electrode Performance, J. Electrochem. Soc. 159 (2012) A214–A221. doi:10.1149/2.024203jes.

[100] M. Gnanavel, M.U.M. Patel, a. K. Sood, A.J. Bhattacharyya, High Rate Capability Lithium Iron Phosphate Wired by Carbon Nanotubes and Galvanostatic Transformed to Graphitic Carbon, J. Electrochem. Soc. 159 (2012) A336. doi:10.1149/2.015204jes.

[101] W. Shyy, S.S. Thakur, H. Ouyang, J. Liu, E. Blosch, Computational techniques for complex transport phenomena, 1997. doi:10.1017/CBO9780511665462.

[102] A. Ghorbani, S. Farhad, V. Chabot, A. Yu, Z. Chen, Effects of structural design on the performance of electrical double layer capacitors, Appl. Energy. 138 (2015) 631–639. doi:10.1016/j.apenergy.2014.09.033.

[103] A.G. Kashkooli, S. Farhad, A.S. Fung, Z. Chen, Effect of convective mass transfer on lead-acid battery performance, Electrochim. Acta. 97 (2013) 278–288. doi:10.1016/j.electacta.2013.02.116.

[104] A. Yamada, Y. Kudo, K.-Y. Liu, Phase Diagram of Li[sub x](Mn[sub y]Fe[sub 1−y])PO[sub 4] (0≤x, y≤1), J. Electrochem. Soc. 148 (2001) A1153. doi:10.1149/1.1401083.

[105] M. Farkhondeh, M. Pritzker, M. Fowler, M. Safari, C. Delacourt, Mesoscopic modeling of Li insertion in phase-separating electrode materials: application to lithium iron phosphate, Phys. Chem. Chem. Phys. 16 (2014) 22555–22565. doi:10.1039/C4CP03530E.

[106] M. Safari, M. Farkhondeh, M. Pritzker, M. Fowler, T. Han, S.K. Chen, Simulation of lithium iron phosphate lithiation/delithiation: Limitations of the core-shell model,

Electrochim. Acta. 115 (2014) 352–357. doi:10.1016/j.electacta.2013.10.159.

[107] C. Delmas, M. Maccario, L. Croguennec, F. Le Cras, F. Weill, Lithium deintercalation in LiFePO4 nanoparticles via a domino-cascade model., Nat. Mater. 7 (2008) 665–671. doi:10.1038/nmat2230.

[108] J.-H. Song, S.-J. You, D.H. Jeon, Numerical modeling and experimental validation of pouch-type lithium-ion battery, J. Appl. Electrochem. 44 (2014) 1013–1023. doi:10.1007/s10800-014-0723-x.

[109] S. Yu, Y. Chung, M.S. Song, J.H. Nam, W. Il Cho, Investigation of design parameter effects on high current performance of lithium-ion cells with LiFePO4/graphite electrodes, J. Appl. Electrochem. 42 (2012) 443–453. doi:10.1007/s10800-012-0418-0.

[110] S. Jung, Computational study about the effect of electrode morphology on the performance of lithium-ion batteries, Int. J. Energy Res. 40 (2016) 1073–1084. doi:10.1002/er.3501.

[111] M.A. Martin, C.-F. Chen, P.P. Mukherjee, S. Pannala, J.-F. Dietiker, J.A. Turner, D. Ranjan, Morphological Influence in Lithium-Ion Battery 3D Electrode Architectures, J. Electrochem. Soc. 162 (2015) A991–A1002. doi:10.1149/2.0631506jes.

[112] Z. Liu, P.P. Mukherjee, Microstructure Evolution in Lithium-Ion Battery Electrode Processing, J. Electrochem. Soc. 161 (2014) E3248–E3258. doi:10.1149/2.026408jes.

[113] C.T. Sun, R.S. Vaidya, Prediction of composite properties from a representative volume element, Compos. Sci. Technol. 56 (1996) 171–179. doi:10.1016/0266-3538(95)00141-7.

[114] T. Kanit, S. Forest, I. Galliet, V. Mounoury, D. Jeulin, Determination of the size of the representative volume element for random composites: statistical and numerical approach, Int. J. Solids Struct. 40 (2003) 3647–3679. doi:10.1016/S0020-7683(03)00143-4.

[115] W.M. Harris, W.K.S. Chiu, Determining the representative volume element size for three-dimensional microstructural material characterization. Part 1: Predictive models, J. Power Sources. 282 (2015) 552–561. doi:10.1016/j.jpowsour.2015.02.035.

[116] M. Stroeven, H. Askes, L.J. Sluys, Numerical determination of representative volumes for granular materials, Comput. Methods Appl. Mech. Eng. 193 (2004) 3221–3238. doi:10.1016/j.cma.2003.09.023.

[117] M. Ostoja-Starzewski, Material spatial randomness: From statistical to representative volume element, Probabilistic Eng. Mech. 21 (2006) 112–132. doi:10.1016/j.probengmech.2005.07.007.

[118] D. TRIAS, J. COSTA, A. TURON, J. HURTADO, Determination of the critical size of a statistical representative volume element (SRVE) for carbon reinforced polymers☆, Acta Mater. 54 (2006) 3471–3484. doi:10.1016/j.actamat.2006.03.042.

[119] J. Joos, M. Ender, T. Carraro, A. Weber, E. Ivers-Tiffée, Representative volume element size for accurate solid oxide fuel cell cathode reconstructions from focused ion beam tomography data, Electrochim. Acta. 82 (2012) 268–276. doi:10.1016/j.electacta.2012.04.133.

[120] A. Bertei, B. Nucci, C. Nicolella, Microstructural modeling for prediction of transport

properties and electrochemical performance in SOFC composite electrodes, Chem. Eng. Sci. 101 (2013) 175–190. doi:10.1016/j.ces.2013.06.032.

[121] Q. Cai, C.S. Adjiman, N.P. Brandon, Modelling the 3D microstructure and performance of solid oxide fuel cell electrodes: Computational parameters, Electrochim. Acta. 56 (2011) 5804–5814. doi:10.1016/j.electacta.2011.04.065.

[122] P.R. Shearing, R.S. Bradley, J. Gelb, F. Tariq, P.J. Withers, N.P. Brandon, Exploring microstructural changes associated with oxidation in Ni–YSZ SOFC electrodes using high resolution X-ray computed tomography, Solid State Ionics. 216 (2012) 69–72. doi:10.1016/j.ssi.2011.10.015.

[123] M. Guo, G. Sikha, R.E. White, Single-Particle Model for a Lithium-Ion Cell: Thermal Behavior, J. Electrochem. Soc. 158 (2011) A122. doi:10.1149/1.3521314.

[124] Y. Ma, J. Ru, M. Yin, H. Chen, W. Zheng, Electrochemical modeling and parameter identification based on bacterial foraging optimization algorithm for lithium-ion batteries, J. Appl. Electrochem. (2016). doi:10.1007/s10800-016-0998-1.

[125] D. Gürsoy, F. De Carlo, X. Xiao, C. Jacobsen, TomoPy: a framework for the analysis of synchrotron tomographic data, J. Synchrotron Radiat. 21 (2014) 1188–1193. doi:10.1107/S1600577514013939.

[126] D.M. Pelt, K.J. Batenburg, Accurately approximating algebraic tomographic reconstruction by filtered backprojection., in: Proc. 2015 Int. Meet. Fully Three-Dimensional Image Reconstr. Radiol. Nucl. Med., 2015.

[127] M. Doyle, Comparison of Modeling Predictions with Experimental Data from Plastic Lithium Ion Cells, J. Electrochem. Soc. 143 (1996) 1890. doi:10.1149/1.1836921.

[128] G. Ning, B.N. Popov, Cycle Life Modeling of Lithium-Ion Batteries, J. Electrochem. Soc. 151 (2004) A1584. doi:10.1149/1.1787631.

[129] H. Munakata, B. Takemura, T. Saito, K. Kanamura, Evaluation of real performance of LiFePO4 by using single particle technique, J. Power Sources. 217 (2012) 444–448. doi:10.1016/j.jpowsour.2012.06.037.

[130] C. Kuss, D. Lepage, G. Liang, S.B. Schougaard, Ultrafast charging of LiFePO4 with gaseous oxidants under ambient conditions, Chem. Sci. 4 (2013) 4223. doi:10.1039/c3sc51195b.

[131] Y. Xu, E. Hu, K. Zhang, X. Wang, V. Borzenets, Z. Sun, P. Pianetta, X. Yu, Y. Liu, X.-Q. Yang, H. Li, In situ Visualization of State-of-Charge Heterogeneity within a LiCoO $_2$ Particle that Evolves upon Cycling at Different Rates, ACS Energy Lett. 2 (2017) 1240–1245. doi:10.1021/acsenergylett.7b00263.

[132] M. Ebner, D.W. Chung, R.E. García, V. Wood, Tortuosity anisotropy in lithium-ion battery electrodes, Adv. Energy Mater. 4 (2014) 1–6. doi:10.1002/aenm.201301278.

[133] J.M. Paz-Garcia, O.O. Taiwo, E. Tudisco, D.P. Finegan, P.R. Shearing, D.J.L. Brett, S.A. Hall, 4D analysis of the microstructural evolution of Si-based electrodes during lithiation: Time-lapse X-ray imaging and digital volume correlation, J. Power Sources. 320 (2016) 196–203. doi:10.1016/j.jpowsour.2016.04.076.

[134] D.S. Eastwood, R.S. Bradley, F. Tariq, S.J. Cooper, O.O. Taiwo, J. Gelb, a. Merkle, D.J.L. Brett, N.P. Brandon, P.J. Withers, P.D. Lee, P.R. Shearing, The application of phase contrast X-ray techniques for imaging Li-ion battery electrodes, Nucl. Instruments Methods Phys. Res. Sect. B Beam Interact. with Mater. Atoms. 324 (2014)

118–123. doi:10.1016/j.nimb.2013.08.066.

[135] L. Wu, X. Xiao, Y. Wen, J. Zhang, Three-dimensional finite element study on stress generation in synchrotron X-ray tomography reconstructed nickel-manganese-cobalt based half cell, J. Power Sources. 336 (2016) 8–18. doi:http://dx.doi.org/10.1016/j.jpowsour.2016.10.052.

[136] D.E. Stephenson, B.C. Walker, C.B. Skelton, E.P. Gorzkowski, D.J. Rowenhorst, D.R. Wheeler, Modeling 3D Microstructure and Ion Transport in Porous Li-Ion Battery Electrodes, J. Electrochem. Soc. 158 (2011) A781. doi:10.1149/1.3579996.

[137] S. Frisco, A. Kumar, J.F. Whitacre, S. Litster, Understanding Li-Ion Battery Anode Degradation and Pore Morphological Changes through Nano-Resolution X-ray Computed Tomography, J. Electrochem. Soc. 163 (2016) A2636–A2640. doi:10.1149/2.0681613jes.

[138] D.A.G. Bruggeman, Berechnung verschiedener physikalischer Konstanten von heterogenen Substanzen. I. Dielektrizitätskonstanten und Leitfähigkeiten der Mischkörper aus isotropen Substanzen, Ann. Phys. 416 (1935) 636–664. doi:10.1002/andp.19354160705.

[139] D.A.G. Bruggeman, Berechnzcrrg verschCedcner physikalducher Eonstanten von heterogenew Yuhstan.xen 1., Ann. Phys. 24 (1935) 636–664. doi:10.1002/andp.19354160705.

[140] I. V. Thorat, D.E. Stephenson, N.A. Zacharias, K. Zaghib, J.N. Harb, D.R. Wheeler, Quantifying tortuosity in porous Li-ion battery materials, J. Power Sources. 188 (2009) 592–600. doi:10.1016/j.jpowsour.2008.12.032.

[141] M. Ender, J. Joos, T. Carraro, E. Ivers-Tiffée, Three-dimensional reconstruction of a composite cathode for lithium-ion cells, Electrochem. Commun. 13 (2011) 166–168. doi:10.1016/j.elecom.2010.12.004.

[142] B. Tjaden, S.J. Cooper, D.J. Brett, D. Kramer, P.R. Shearing, On the origin and application of the Bruggeman correlation for analysing transport phenomena in electrochemical systems, Curr. Opin. Chem. Eng. 12 (2016) 44–51. doi:10.1016/j.coche.2016.02.006.

[143] B. Yan, C. Lim, Z. Song, L. Zhu, Analysis of Polarization in Realistic Li Ion Battery Electrode Microstructure Using Numerical Simulation, Electrochim. Acta. 185 (2015) 125–141. doi:10.1016/j.electacta.2015.10.086.

[144] J. Li, Z. Tang, Z. Zhang, Controllable formation and electrochemical properties of one-dimensional nanostructured spinel Li4Ti5O12, Electrochem. Commun. 7 (2005) 894–899. doi:10.1016/j.elecom.2005.06.012.

[145] D. Ahn, X. Xiao, Extended lithium titanate cycling potential window with near zero capacity loss, Electrochem. Commun. 13 (2011) 796–799. doi:10.1016/j.elecom.2011.05.005.

[146] A. Nugroho, S.J. Kim, K.Y. Chung, B.-W. Cho, Y.-W. Lee, J. Kim, Facile synthesis of nanosized Li4Ti5O12 in supercritical water, Electrochem. Commun. 13 (2011) 650–653. doi:10.1016/j.elecom.2011.03.037.

[147] K. Kanamura, T. Chiba, K. Dokko, Preparation of Li4Ti5O12 spherical particles for rechargeable lithium batteries, J. Eur. Ceram. Soc. 26 (2006) 577–581. doi:10.1016/j.jeurceramsoc.2005.06.014.

[148] S.S. Lee, K.-T. Byun, J.P. Park, S.K. Kim, H.-Y. Kwak, I.-W. Shim, Preparation of Li4Ti5O12 nanoparticles by a simple sonochemical method, Dalt. Trans. (2007) 4182. doi:10.1039/b707164g.

[149] D. Wang, X. Wu, Y. Zhang, J. Wang, P. Yan, C. Zhang, D. He, The influence of the TiO2 particle size on the properties of Li4Ti5O12 anode material for lithium-ion battery, Ceram. Int. 40 (2014) 3799–3804. doi:10.1016/j.ceramint.2013.09.038.

[150] L. Cheng, J. Yan, G.-N. Zhu, J.-Y. Luo, C.-X. Wang, Y.-Y. Xia, General synthesis of carbon-coated nanostructure Li $_4$ Ti $_5$ O $_{12}$ as a high rate electrode material for Li-ion intercalation, J. Mater. Chem. 20 (2010) 595–602. doi:10.1039/B914604K.

[151] S. Eiden-Assmann, J. Widoniak, G. Maret, Synthesis and Characterization of Hollow and Non-Hollow Monodisperse Colloidal TiO 2 Particles, J. Dispers. Sci. Technol. 25 (2005) 535–545. doi:10.1081/DIS-200025719.

[152] Y. Shen, M. Søndergaard, M. Christensen, S. Birgisson, B.B. Iversen, Solid State Formation Mechanism of Li 4 Ti 5 O 12 from an Anatase TiO 2 Source, Chem. Mater. 26 (2014) 3679–3686.

[153] H.-K. Kim, J. Jegal, J.-Y. Kim, S. Yoon, K.C. Roh, K. Kim, In situ fabrication of lithium titanium oxide by microwave-assisted alkalization for high-rate lithium-ion batteries, J. Mater. Chem. A. 1 (2013) 14849–14852. doi:10.1039/c3ta13206d.

[154] C. Lim, B. Yan, H. Kang, Z. Song, W.C. Lee, V. De Andrade, F. De Carlo, L. Yin, Y. Kim, L. Zhu, Analysis of geometric and electrochemical characteristics of lithium cobalt oxide electrode with different packing densities, J. Power Sources. 328 (2016) 46–55. doi:10.1016/j.jpowsour.2016.07.119.

[155] T. Hutzenlaub, A. Asthana, J. Becker, D.R. Wheeler, R. Zengerle, S. Thiele, FIB/SEM-based calculation of tortuosity in a porous LiCoO2 cathode for a Li-ion battery, Electrochem. Commun. 27 (2013) 77–80. doi:10.1016/j.elecom.2012.11.006.

[156] S. Stewart, P. Albertus, V. Srinivasan, I. Plitz, N. Pereira, G. Amatucci, J. Newman, Optimizing the Performance of Lithium Titanate Spinel Paired with Activated Carbon or Iron Phosphate, J. Electrochem. Soc. 155 (2008) A253. doi:10.1149/1.2830552.

[157] J. Christensen, V. Srinivasan, J. Newman, Optimization of Lithium Titanate Electrodes for High-Power Cells, J. Electrochem. Soc. 153 (2006) A560. doi:10.1149/1.2172535.

[158] M. Smith, R.E. García, Q.C. Horn, The Effect of Microstructure on the Galvanostatic Discharge of Graphite Anode Electrodes in LiCoO[sub 2]-Based Rocking-Chair Rechargeable Batteries, J. Electrochem. Soc. 156 (2009) A896. doi:10.1149/1.3216000.

[159] G.E. Blomgren, The Development and Future of Lithium Ion Batteries, J. Electrochem. Soc. 164 (2017) A5019–A5025. doi:10.1149/2.0251701jes.

[160] M. Hu, X. Pang, Z. Zhou, Recent progress in high-voltage lithium ion batteries, J. Power Sources. 237 (2013) 229–242. doi:10.1016/j.jpowsour.2013.03.024.

[161] V.A. Agubra, L. Zuniga, D. Flores, J. Villareal, M. Alcoutlabi, Composite Nanofibers as Advanced Materials for Li-ion, Li-O2 and Li-S Batteries, Electrochim. Acta. 192 (2016) 529–550. doi:10.1016/j.electacta.2016.02.012.

[162] T. Waldmann, M. Wohlfahrt-Mehrens, Effects of rest time after Li plating on safety behavior—ARC tests with commercial high-energy 18650 Li-ion cells, Electrochim. Acta. 230 (2017) 454–460. doi:10.1016/j.electacta.2017.02.036.

[163] M. Rashid, A. Gupta, Experimental assessment and model development of cycling

behavior in Li-ion coin cells, Electrochim. Acta. 231 (2017) 171–184. doi:10.1016/j.electacta.2017.02.040.

[164] H. Wang, Y. Jang, B. Huang, D.R. Sadoway, Y. Chiang, TEM Study of Electrochemical Cycling-Induced Damage and Disorder in LiCoO2 Cathodes for Rechargeable Lithium Batteries, J. Electrochem. Soc. 146 (1999) 473–480. doi:10.1149/1.1391631.

[165] D. Wang, X. Wu, Z. Wang, L. Chen, Cracking causing cyclic instability of LiFePO4 cathode material, J. Power Sources. 140 (2005) 125–128. doi:10.1016/j.jpowsour.2004.06.059.

[166] K. Abe, H. Yoshitake, T. Kitakura, T. Hattori, H. Wang, M. Yoshio, Additives-containing functional electrolytes for suppressing electrolyte decomposition in lithium-ion batteries, Electrochim. Acta. 49 (2004) 4613–4622. doi:10.1016/j.electacta.2004.05.016.

[167] X. Liao, X. Zheng, J. Chen, Z. Huang, M. Xu, L. Xing, Y. Liao, Q. Lu, X. Li, W. Li, Tris(trimethylsilyl)phosphate as electrolyte additive for self-discharge suppression of layered nickel cobalt manganese oxide, Electrochim. Acta. 212 (2016) 352–359. doi:10.1016/j.electacta.2016.07.026.

[168] J. Xu, R.D. Deshpande, J. Pan, Y.-T. Cheng, V.S. Battaglia, Electrode Side Reactions, Capacity Loss and Mechanical Degradation in Lithium-Ion Batteries, J. Electrochem. Soc. 162 (2015) A2026–A2035. doi:10.1149/2.0291510jes.

[169] X. Zeng, G.L. Xu, Y. Li, X. Luo, F. Maglia, C. Bauer, S.F. Lux, O. Paschos, S.J. Kim, P. Lamp, J. Lu, K. Amine, Z. Chen, Kinetic study of parasitic reactions in lithium-ion

batteries: A case study on LiNi0.6Mn0.2Co0.2O2, ACS Appl. Mater. Interfaces. 8 (2016) 3446–3451. doi:10.1021/acsami.5b11800.

[170] J. Christensen, J. Newman, Stress generation and fracture in lithium insertion materials, J. Solid State Electrochem. 10 (2006) 293–319. doi:10.1007/s10008-006-0095-1.

[171] J. Christensen, J. Newman, A Mathematical Model of Stress Generation and Fracture in Lithium Manganese Oxide, J. Electrochem. Soc. 153 (2006) A1019. doi:10.1149/1.2185287.

[172] X. Zhang, W. Shyy, A. Marie Sastry, Numerical Simulation of Intercalation-Induced Stress in Li-Ion Battery Electrode Particles, J. Electrochem. Soc. 154 (2007) S21. doi:10.1149/1.2793718.

[173] J. Park, W. Lu, A.M. Sastry, Numerical Simulation of Stress Evolution in Lithium Manganese Dioxide Particles due to Coupled Phase Transition and Intercalation, J. Electrochem. Soc. 158 (2011) A201. doi:10.1149/1.3526597.

[174] R.E. Garcia, Y.-M. Chiang, W. Craig Carter, P. Limthongkul, C.M. Bishop, R.E. García, Y.-M. Chiang, W. Craig Carter, P. Limthongkul, C.M. Bishop, Microstructural Modeling and Design of Rechargeable Lithium-Ion Batteries, J. Electrochem. Soc. 152 (2005) A255. doi:10.1149/1.1836132.

[175] S. Renganathan, G. Sikha, S. Santhanagopalan, R.E. White, Theoretical Analysis of Stresses in a Lithium Ion Cell, J. Electrochem. Soc. 157 (2010) A155. doi:10.1149/1.3261809.

[176] Y. Dai, L. Cai, R.E. White, Simulation and analysis of stress in a Li-ion battery with a blended LiMn2O4 and LiNi0.8Co0.15Al 0.05O2 cathode, J. Power Sources. 247 (2014)

365–376. doi:10.1016/j.jpowsour.2013.08.113.

[177] P. Barai, P.P. Mukherjee, Stochastic Analysis of Diffusion Induced Damage in Lithium-Ion Battery Electrodes, J. Electrochem. Soc. 160 (2013) A955–A967. doi:10.1149/2.132306jes.

[178] Z. Liu, J. Scott Cronin, Y.C.K. Chen-Wiegart, J.R. Wilson, K.J. Yakal-Kremski, J. Wang, K.T. Faber, S.A. Barnett, Three-dimensional morphological measurements of LiCoO2 and LiCoO2/Li(Ni1/3Mn1/3Co1/3)O 2 lithium-ion battery cathodes, J. Power Sources. 227 (2013) 267–274. doi:10.1016/j.jpowsour.2012.11.043.

[179] R. Scipioni, P.S. J??rgensen, D.T. Ngo, S.B. Simonsen, Z. Liu, K.J. Yakal-Kremski, H. Wang, J. Hjelm, P. Norby, S.A. Barnett, S.H. Jensen, Electron microscopy investigations of changes in morphology and conductivity of LiFePO4/C electrodes, J. Power Sources. 307 (2016) 259–269. doi:10.1016/j.jpowsour.2015.12.119.

[180] G. Inoue, M. Kawase, Numerical and experimental evaluation of the relationship between porous electrode structure and effective conductivity of ions and electrons in lithium-ion batteries, J. Power Sources. 342 (2017) 476–488. doi:10.1016/j.jpowsour.2016.12.098.

[181] V. Malavé, J.R. Berger, H. Zhu, R.J. Kee, A computational model of the mechanical behavior within reconstructed LixCoO2 Li-ion battery cathode particles, Electrochim. Acta. 130 (2014) 707–717. doi:10.1016/j.electacta.2014.03.113.

[182] H. Mendoza, S.A. Roberts, V.E. Brunini, A.M. Grillet, Mechanical and Electrochemical Response of a LiCoO2 Cathode using Reconstructed Microstructures, Electrochim. Acta. 190 (2016) 1–15. doi:10.1016/j.electacta.2015.12.224.

[183] H. Liu, J.M. Foster, A. Gully, S. Krachkovskiy, M. Jiang, Y. Wu, X. Yang, B. Protas, G.R. Goward, G.A. Botton, Three-dimensional investigation of cycling-induced microstructural changes in lithium-ion battery cathodes using focused ion beam/scanning electron microscopy, J. Power Sources. 306 (2016) 300–308. doi:10.1016/j.jpowsour.2015.11.108.

[184] K. Takahashi, V. Srinivasan, Examination of Graphite Particle Cracking as a Failure Mode in Lithium-Ion Batteries: A Model-Experimental Study, J. Electrochem. Soc. 162 (2015) A635–A645. doi:10.1149/2.0281504jes.

[185] K. Takahashi, K. Higa, S. Mair, M. Chintapalli, N. Balsara, V. Srinivasan, Mechanical Degradation of Graphite/PVDF Composite Electrodes: A Model-Experimental Study, J. Electrochem. Soc. 163 (2016) A385–A395. doi:10.1149/2.0271603jes.

[186] A.M. Grillet, T. Humplik, E.K. Stirrup, S.A. Roberts, D.A. Barringer, C.M. Snyder, M.R. Janvrin, C.A. Apblett, Conductivity Degradation of Polyvinylidene Fluoride Composite Binder during Cycling: Measurements and Simulations for Lithium-Ion Batteries, J. Electrochem. Soc. 163 (2016) A1859–A1871. doi:10.1149/2.0341609jes.

[187] E.K. Rahani, V.B. Shenoy, Role of Plastic Deformation of Binder on Stress Evolution during Charging and Discharging in Lithium-Ion Battery Negative Electrodes, J. Electrochem. Soc. 160 (2013) A1153–A1162. doi:10.1149/2.046308jes.

[188] B. Rieger, S. Schlueter, S. V Erhard, A. Jossen, Strain Propagation in Lithium-Ion Batteries from the Crystal Structure to the Electrode Level, 163 (2016). doi:10.1149/2.0431608jes.

[189] M. Indrikova, S. Grunwald, F. Golks, A. Netz, B. Westphal, A. Kwade, The

Morphology of Battery Electrodes with the Focus of the Conductive Additives Paths, J. Electrochem. Soc. 162 (2015) A2021–A2025. doi:10.1149/2.0441510jes.

[190] W. Wu, X. Xiao, M. Wang, X. Huang, A Microstructural Resolved Model for the Stress Analysis of Lithium-Ion Batteries, J. Electrochem. Soc. 161 (2014) A803–A813. doi:10.1149/2.082405jes.

[191] F. Hao, D. Fang, Diffusion-Induced Stresses of Spherical Core-Shell Electrodes in Lithium-Ion Batteries: The Effects of the Shell and Surface/Interface Stress, J. Electrochem. Soc. 160 (2013) A595–A600. doi:10.1149/2.054304jes.

[192] X. Zhang, W. Shyy, A. Marie Sastry, Erratum: Numerical Simulation of Intercalation-Induced Stress in Li-Ion Battery Electrode Particles [J. Electrochem. Soc., 154, A910 (2007)], J. Electrochem. Soc. 154 (2007) S21. doi:10.1149/1.2793718.

[193] R.E. García, Y.-M. Chiang, Spatially Resolved Modeling of Microstructurally Complex Battery Architectures, J. Electrochem. Soc. 154 (2007) A856. doi:10.1149/1.2754072.

[194] M.A. Meyers, K.K. Chawla, Mechanical Behavior of Materials, (2009) 880. www.cambridge.org/9780521866750.

[195] J.L. Chu, S. Lee, The effect of chemical stresses on diffusion, J. Appl. Phys. 75 (1994) 2823–2829. doi:10.1063/1.356174.

[196] G.A. Gogotsi, G.G. Gnesin, Y.L. Grushevskii, V.P. Zavada, Strength and crack resistance of ceramics. Report 3. A silicon carbide ceramic, Strength Mater. 19 (1987) 674–677. doi:10.1007/BF01524304.